Generation, Storage, and Retrieval of Nonclassical States of Light using Atomic Ensembles

A thesis presented
by

Matthew D. Eisaman

to
The Department of Physics
in partial fulfillment of the requirements
for the degree of
Doctor of Philosophy
in the subject of

Physics

Harvard University
Cambridge, Massachusetts
May 2006

Thesis advisor

Mikhail D. Lukin

Author

Matthew D. Eisaman

Generation, Storage, and Retrieval of Nonclassical States of Light using Atomic Ensembles

Abstract

This thesis presents the experimental demonstration of several novel methods for generating, storing, and retrieving nonclassical states of light using atomic ensembles, and describes applications of these methods to frequency-tunable single-photon generation, single-photon memory, quantum networks, and long-distance quantum communication.

We first demonstrate emission of quantum-mechanically correlated pulses of light with a time delay between the pulses that is coherently controlled by utilizing ^{87}Rb atoms. The experiment is based on Raman scattering, which produces correlated pairs of excited atoms and photons, followed by coherent conversion of the atomic states into a different photon field after a controllable delay.

We then describe experiments demonstrating a novel approach for conditionally generating nonclassical pulses of light with controllable photon numbers, propagation direction, timing, and pulse shapes. We observe nonclassical correlations in relative photon number between correlated pairs of photons, and create few-photon light pulses with sub-Poissonian photon-number statistics via conditional detection on one field of the pair. Spatio-temporal control over the pulses is obtained by exploiting

long-lived coherent memory for photon states and electromagnetically induced transparency (EIT) in an optically dense atomic medium.

Finally, we demonstrate the use of EIT for the controllable generation, transmission, and storage of single photons with tunable frequency, timing, and bandwidth. To this end, we study the interaction of single photons produced in a "source" ensemble of ^{87}Rb atoms at room temperature with another "target" ensemble. This allows us to simultaneously probe the spectral and quantum statistical properties of narrow-bandwidth single-photon pulses, revealing that their quantum nature is preserved under EIT propagation and storage. We measure the time delay associated with the reduced group velocity of the single-photon pulses and report observations of their storage and retrieval.

Together these experiments utilize atomic ensembles to realize a narrow-bandwidth single-photon source, single-photon memory that preserves the quantum nature of the single photons, and a primitive quantum network comprised of two atomic-ensemble quantum memories connected by a single photon in an optical fiber. Each of these experimental demonstrations represents an essential element for the realization of long-distance quantum communication.

Contents

Title Page i
Abstract iii
Table of Contents v
List of Figures vii
List of Tables ix
Citations to Previously Published Work x
Acknowledgments xii
Dedication xv

1 Introduction **1**
1.1 Motivation: Quantum Control of Single Photons 1
1.2 The Control Tool: Electromagnetically Induced Transparency (EIT) . 4
1.2.1 EIT Basics 5
1.2.2 Dark-State Polaritons 7
1.2.3 EIT-based Quantum Memory 10
1.3 Quantum Control of Single Photons using Atomic Ensembles 11
1.3.1 EIT-Based Single-Photon Generation and Storage 12
1.3.2 Quantum Networks and Long-Distance Quantum Communication using Atomic Ensembles 15
1.4 Progress towards Long-Distance Quantum Communication using Atomic Ensembles 18
1.5 Overview 21

2 Generation of Correlated Photon States using Atomic Ensembles **23**
2.1 Introduction 23
2.2 Generating Correlated Photon States 23
2.2.1 Experimental Setup 26
2.2.2 Continuous-Wave Regime 31
2.2.3 Pulsed Regime 34
2.3 Observation of Correlations 35
2.3.1 Quantifying Correlations 36

2.3.2 Nonclassical Correlations in the Continuous-Wave Regime . . 43
2.4 Conclusions 48

3 Shaping Quantum Pulses of Light using Atomic Ensembles 49
3.1 Introduction 49
3.2 Few-Photon Pulse Shaping 50
3.3 Quantum-Correlated Photon States 59
3.4 Conclusions 63

4 Conditional Generation of Single Photons using Atomic Ensembles 64
4.1 Introduction 64
4.2 Conditionally Generated Nonclassical States of Light 67
4.2.1 Conditions for High-Fidelity Single-Photon Generation 67
4.2.2 Experimental Observations 70
4.3 Experimental Conditions allowing Conditional Single-Photon Generation 73
4.4 Single-Photon Generation 80
4.4.1 Experimental Demonstration 80
4.4.2 Theoretical Model 84
4.5 Conclusions 89

5 EIT-Based Slowing, Storage, and Retrieval of Single-Photon Pulses using Atomic Ensembles 92
5.1 Introduction 92
5.2 Single-Photon EIT 93
5.3 EIT-based Slowing, Storage, and Retrieval of Single Photons 97
5.4 Conclusions 100

6 Conclusion 102

A Appendices to Chapter 2 105
A.1 Properties of Rubidium 87 105
A.2 Low-Noise Photodetector Details 112
A.3 Photon-Number Statistics 118
A.4 Hardware Requirements for Detection of Twin-Mode Squeezing . . . 123

B Appendices to Chapter 4 127
B.1 Evaluating the Uncertainty in the Second-Order Correlation Function 127

Bibliography 132

List of Figures

1.1 Electromagnetically induced transparency. 5
1.2 Basic idea behind EIT-based single-photon generation. 13
1.3 Atomic-ensemble based quantum repeater. 16
1.4 Quantum network. 17

2.1 Atomic-level configuration and experimental setup. 25
2.2 Fluorescence as a function of frequency for the D_1 line ($5^2S_{1/2} \rightarrow 5^2P_{1/2}$) of rubidium. 28
2.3 Transverse spatial position of the retrieve laser and anti-Stokes field in the far-field, as imaged with a CCD camera. 30
2.4 Correlations in the continuous-wave regime. 32
2.5 Correlations in the pulsed regime. 36
2.6 Fluctuations and correlations in the pulsed regime. 37
2.7 Modeling twin-mode intensity squeezing in the presence of unbalanced losses and delays. 40
2.8 Twin-mode intensity squeezing in the continuous-wave regime. 46

3.1 Experimental procedure. 51
3.2 Schematic of the experimental setup. 52
3.3 Photograph of the experimental setup. 53
3.4 Write and retrieve laser frequencies, relative to the fluorescence spectrum of the D_1 line ($5^2S_{1/2} \rightarrow 5^2P_{1/2}$) of rubidium. 54
3.5 Stokes pulse shapes. 55
3.6 Anti-Stokes pulse shapes. 57
3.7 Measured anti-Stokes pulse width (full-width at half-max) and total photon number as a function the retrieve laser power. 58
3.8 Observation of nonclassical correlations. 61
3.9 Signal and noise processes in EIT-based retrieval of atomic coherences. 62

4.1 Conditional nonclassical state generation. 72
4.2 Experimental setup. 74

4.3 Photograph of the experimental setup. 75
4.4 Noise ×10 (green squares) and signal-to-noise ratio/100 (blue diamonds) on the anti-Stokes channel as a function of temperature. . . . 77
4.5 Signal (magenta diamonds), noise (green triangles), and signal-to-noise ratio/10 (blue diamonds) on the anti-Stokes channel as a function of time. 79
4.6 Experimental procedure. 81
4.7 Observation of conditional single-photon generation. 83
4.8 Model system used to calculate $g^{(2)}(AS)$ in the presence of loss and background photons on the anti-Stokes channel. 86

5.1 Observation of single-photon EIT. 94
5.2 Measurement of single-photon pulse delay. 98
5.3 Measurement of single-photon storage. 99

A.1 Atomic-level structure for the D_1 line ($5^2S_{1/2} \rightarrow 5^2P_{1/2}$) of ^{87}Rb . . . 106
A.2 Calculated number density of ^{87}Rb (assuming as isotopically pure ensemble) as a function of temperature. 107
A.3 Diffusion constant D_0 as a function of temperature for four buffer-gas atoms: He, Ne, N_2, and Ar. 108
A.4 Predicted diffusion times for various experimental conditions. 110
A.5 Schematic of the low-noise photodetector circuit. 112
A.6 Measurement of the standard quantum limit and noise floor. 115
A.7 Comparison of Poisson and thermal photon-number statistics. 120
A.8 Limitations on the observation of twin-mode intensity squeezing. . . . 125

List of Tables

4.1 Scaling for the anti-Stokes pulse Q-parameter and Fock state fidelity F. 69

A.1 ^{87}Rb physical properties. 105
A.2 Optical properties for the D_1 line ($5^2S_{1/2} \rightarrow 5^2P_{1/2}$) of ^{87}Rb 106
A.3 Photodetector parts list. 114

Citations to Previously Published Work

Some of the introductory material appears in

> "Quantum Control of Light Using Electromagnetically Induced Transparency", A. André, M. D. Eisaman, R. L. Walsworth, A. S. Zibrov, and M. D. Lukin, J. Phys. B: At. Mol. Opt. Phys. **38**, S589 *Special Issue: Einstein Year*, 2005;

and in

> "Electromagnetically Induced Transparency: Toward Quantum Control of Single Photons", M. D. Eisaman, M. Fleischhauer, M. D. Lukin, and A. S. Zibrov, Optics and Photonics News, January 2005.

Parts of Chapter 2 have been published as

> "Atomic Memory for Correlated Photon States", C. H. van der Wal, M. D. Eisaman, A. André, R. L. Walsworth, D. F. Phillips, A. S. Zibrov, and M. D. Lukin, Science **301**, 196 (2003);

and as

> "Towards non-classical light storage via atomic-vapor Raman scattering", C. H. van der Wal, M. D. Eisaman, A. S. Zibrov, A. André, D. F. Phillips, R. L. Walsworth, and M. D. Lukin, Proc. of SPIE **5115**, 236 (2003).

Parts of Chapter 3 have been published as

> "Shaping Quantum Pulses of Light via Coherent Atomic Memory", M. D. Eisaman, L. Childress, A. André, F. Massou, A. S. Zibrov, and M. D. Lukin, Phys. Rev. Lett. **93**, 233602 (2004), `quant-ph/0406093`.

Parts of Chapter 4 have been published as

> "Towards Quantum Control of Light: Shaping Quantum Pulses of Light via Coherent Atomic Memory", L. Childress, M. D. Eisaman, A. André, F. Massou, A. S. Zibrov, and M. D. Lukin, in Decoherence, Entanglement, and Information Protection in Complex Quantum Systems, V. M. Akulin, A. Sarfati, G. Kurizki and S. Pellegrin, eds. (Kluwer Academic Publisher, Boston 2005);

and as

> "Shaping Quantum Pulses of Light via Coherent Atomic Memory", M. D. Eisaman, L. Childress, A. André, F. Massou, A. S. Zibrov, and M. D. Lukin, Phys. Rev. Lett. **93**, 233602 (2004), `quant-ph/0406093`;

and as

> "Electromagnetically induced transparency with tunable single-photon pulses", M. D. Eisaman, A. André, F. Massou, M. Fleischhauer, A. S. Zibrov, and M. D. Lukin, Nature **438**, 837 (2005);

and as

> "Progress toward generating, storing, and communicating single-photon states using coherent atomic memory", M. D. Eisaman, A. André, F. Massou, G.-W. Li, L. Childress, A. S. Zibrov, and M. D. Lukin, Proc. of SPIE **5842**, 105 (2005).

Parts of Chapter 5 have been published as

> "Electromagnetically induced transparency with tunable single-photon pulses", M. D. Eisaman, A. André, F. Massou, M. Fleischhauer, A. S. Zibrov, and M. D. Lukin, Nature **438**, 837 (2005).

Electronic preprints (shown in `typewriter font`) are available on the Internet at the following URL:

> `http://www.arxiv.org`

Acknowledgments

First, I would like to thank my advisor Mikhail (Misha) Lukin for his enthusiasm and support during my four years in his group. His deep knowledge of many fields has been an invaluable resource, and his intense curiosity and high standards always inspired and challenged me. Misha, I consider it a privilege to have been your student, and will fondly remember the time spent in your lab.

I would also like to thank Alexander (Sasha) Zibrov, who served as my primary experimental mentor during the completion of this work. I learned most of the experimental physics I know from Sasha, and without him, this thesis would certainly not have been possible.

In addition, I would like to thank the other members of my thesis committee, John Doyle and Charles Marcus. Their feedback on my preliminary exam raised important questions that steered this work in the right direction. Also, I would like to thank Ron Walsworth, David Phillips, and Irina Novikova for many fruitful discussions and useful experimental suggestions.

This thesis was only possible because of the extremely talented colleagues with whom I had the opportunity to work and interact. When I first came to the lab, I worked very closely with Caspar van der Wal, a very talented experimentalist. I learned a lot about experimental physics from Caspar, and had a lot of fun in the process. After Caspar's departure, I had the privilege to work with Lilian Childress, who always has many original and creative ideas, and Florent Massou, who had a very significant impact on the experiment despite his short time with us.

Throughout this entire time, I benefitted greatly from a close interaction with theorists, most notably Axel André. The close collaboration between theory and ex-

periment was an important factor in this project's success, and Axel's patience and insight made this collaboration both productive and enjoyable. In addition, discussions with Michael Hohensee greatly helped us with our understanding of the system. Collaboration with Michael Fleischhauer was very helpful, especially in understanding some of the most recent results. Finally, I'd like to thank Anders Sorensen for many useful discussions.

I would like to thank many other colleagues for useful and stimulating discussions over the years: Michal Bajcsy, Jake Taylor, Darrick Chang, Mohammad Hafezi, Aryesh Mukherjee, Gurudev Dutt, Vlatko Balić, Philip Walther, Alexey Gorshkov, Liang Jiang, Chris Slowe, Naomi Ginsberg, Trygve Ristroph, Zac Dutton, Laurent Vernac, and Yanhong Xiao.

The success of the experiments depended greatly on the design of many custom pieces of electronics. For this I would like to Bill Walker, and especially Jim MacArthur, who designed our counting electronics and helped greatly with the design and construction of our low-noise photodiodes. I have learned a lot of electronics from Jim during my time at Harvard.

The experiments also benefitted from many custom-machined parts. For this, and for teaching me everything I know about the machine shop, I would like to thank Stan Cotreau.

The Physics Department staff has been an invaluable resource. I would like to thank Sheila Ferguson, Vickie Green, Stuart McNeil, Billy Moura, Jean O'Connor, and Marilyn O'Connor for all their help.

I'd like to thank my friends and family for their support and encouragement

during my time at Harvard. To my parents who taught me the value of hard work, and sacrificed so much for my education, I can't thank you enough. This thesis is dedicated to you. Finally, to Heather, thank you for your support, encouragement, and understanding - I couldn't have done it without you.

To my parents

Chapter 1

Introduction

1.1 Motivation: Quantum Control of Single Photons

One of the most exciting challenges in quantum optics is the development of techniques to facilitate controlled, coherent interactions between single photons and matter. Beyond their fundamental importance in optical science, such techniques provide the key elements for the practical realization of a photonic quantum network - an interconnected web of stationary sites capable of storing and processing quantum information. Such networks are expected to play a major role in extending the range of quantum communication and quantum cryptography to long distances, and possibly for implementing scalable quantum-information processors [19, 20, 34, 27, 28].

Photons are robust and efficient carriers of quantum information, while atoms are well-suited to precise quantum-state manipulation and long-lived storage of quantum

information in metastable atomic states. Therefore, a commonly envisioned realization of a quantum network involves single-photon transmission through optical fibers connecting a number of memory nodes that utilize atoms for the generation, storage and processing of quantum states. The realization of this vision requires: techniques for generating nonclassical states of light and atoms, techniques for coherent transfer of quantum states from photons to atoms and vice versa, and a quantum memory that is capable of storing, manipulating, and releasing quantum states at the level of individual quanta [31].

Several promising avenues for achieving such interactions are currently being explored, and remarkable progress has been achieved in just the past few years. In particular, cavity QED experiments [70, 74, 96, 97] have realized strong coupling between single optical photons and single atoms using high-finesse micro-cavities. This approach involves controlled, coherent absorption and emission of single photons by single atoms, allowing the generation and storage of single photons, as well as the creation of nonlinear interactions between them. While these experiments are quite elegant, they are technically very challenging because they require the strong coupling of a single atom to a single cavity mode. Despite these challenges, the spectacular experimental progress in this field makes it a viable avenue for studying the fundamental physics of atom-photon interactions, as well as for quantum networking, with possibilities ranging from deterministic single-photon sources to quantum logic operations.

Another promising avenue involves the manipulation of quantum pulses of light in optically dense atomic ensembles. In this case, a large photon-atom coupling is

easy to achieve by using an atomic ensemble with a large optical depth. The primary challenge of this approach is to control the light-matter interaction and to eliminate the dissipative processes that normally accompany such interactions. Recently a number of protocols have been developed [73, 18, 52, 40] that utilize a dispersive light-matter interaction and the ideas of quantum teleportation to achieve continuous-variable quantum state mapping into atomic samples. These ideas have recently been utilized to combine off-resonant, dispersive interactions together with quantum measurements to map quantum states of weak laser pulses into atoms [65].

At the same time, the desired control over the light-matter interactions in dense atomic ensembles can also be achieved by using a technique called Electromagnetically Induced Transparency (EIT) [54, 84, 41]. EIT is a quantum-interference effect that allows the propagation of a light pulse inside a resonant medium to be controlled using a second electromagnetic field. This thesis presents experiments that utilize EIT for the quantum control of multi-photon and single-photon pulses of light and their interactions with atomic ensembles.

This chapter gives an introduction and background to EIT [54, 83, 41], propagation in an EIT medium [56, 42], and EIT-based "light storage" [103, 79]. In addition, we describe the basic idea behind using EIT as a quantum control tool to generate and store single photons using atomic ensembles. Finally, we describe a proposal for utilizing these tools to realize both quantum networks and long-distance quantum communication using atomic ensembles [34].

1.2 The Control Tool: Electromagnetically Induced Transparency (EIT)

When the frequency of a laser pulse approaches that of a particular atomic transition, the optical response of the medium is greatly enhanced. Typically under such conditions, light propagation is accompanied by strong absorption and dispersion, as the atoms are driven into fluorescing excited states.

EIT is a technique for the coherent control of light propagation in such a resonant medium. Consider the situation in which the atoms have a pair of long-lived lower energy states ($|g\rangle$ and $|s\rangle$ in Fig. 1.1(a)). This is the case, for example, for sublevels of different total angular momentum within the electronic ground state of alkali atoms. In order to modify the propagation of light that couples the ground state $|g\rangle$ to an electronically excited state $|e\rangle$ in such a medium (signal field, red arrow), one can apply a second optical field that is near resonance with the transition $|s\rangle - |e\rangle$ (control field, black arrow). The combined effect of these two fields is to place the atoms into a coherent superposition of the states $|g\rangle$ and $|s\rangle$. The atoms can simultaneously occupy both states ($|g\rangle$ and $|s\rangle$) with a definite phase relationship, such that the two possible absorption pathways ($|g\rangle \rightarrow |e\rangle$ and $|s\rangle \rightarrow |e\rangle$) interfere destructively. Mathematically, this can be seen by considering the portion at the Hamiltonian that describes the absorption pathways $|g\rangle \rightarrow |e\rangle$ and $|s\rangle \rightarrow |e\rangle$:

$$H \sim \Omega_s |e\rangle \langle g| + \Omega_c |e\rangle \langle s| , \tag{1.1}$$

where Ω_c (Ω_s) represents the control (signal) field Rabi frequency (proportional to the electric field amplitude [113]). In this case, we can define a so-called "dark state"

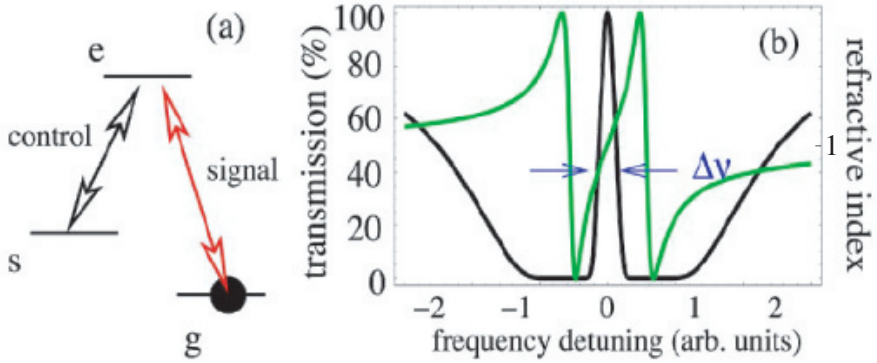

Figure 1.1: Electromagnetically induced transparency. **(a)** Prototype atomic system for EIT. **(b)** Transmission (black curve) and refractive index (green curve) of the signal field under EIT conditions as a function of the signal frequency . Rapid variation of the refractive index with changing signal frequency causes a reduction of the signal-field group velocity.

$|D\rangle$, for which there is no absorption to the excited state $|e\rangle$ [41]:

$$|D\rangle = \frac{(\Omega_c |g\rangle - \Omega_s |s\rangle)}{\sqrt{|\Omega_c|^2 + |\Omega_s|^2}}. \tag{1.2}$$

Under such conditions, none of the atoms are promoted to the excited state, leading to vanishing light absorption [54]. In this way, the EIT control field is utilized to modify the propagation of the signal field.

1.2.1 EIT Basics

Fig. 1.1(b) shows the transmission of the signal field through an atomic medium under EIT conditions (black line), as a function of the detuning of the signal field from the $|g\rangle - |e\rangle$ resonance (the control field is assumed to be resonant with the $|s\rangle - |e\rangle$ transition). In the case when the resonant control field is strong and its intensity is constant in time but the signal field is weak, the response of the atomic ensemble

as experienced by the signal field can be described in terms of the signal-field linear susceptibility $\chi(\omega)$ [41]:

$$\chi(\omega) = \frac{n|\mu_{ge}|^2}{\epsilon_0 \hbar} \frac{i(\gamma_{gs} - i\omega)}{(\gamma_{ge} - i\omega)(\gamma_{gs} - i\omega) + |\Omega|^2} \tag{1.3}$$

$$= \frac{2g^2 N}{\omega_{ge}} \frac{i(\gamma_{gs} - i\omega)}{(\gamma_{ge} - i\omega)(\gamma_{gs} - i\omega) + |\Omega|^2} \tag{1.4}$$

where n is the atomic density, μ_{ge} is the $|g\rangle - |e\rangle$ dipole matrix element, ϵ_0 is the permittivity, $\hbar$ is Planck's constant, γ_{ij} corresponds to the relaxation rate of the $|i\rangle\langle j|$ coherence, Ω is the Rabi frequency of the control field, N is the total number of atoms in the laser mode volume, g is the atom-signal field coupling constant $g = \mu_{ge}\sqrt{\frac{\omega_{ge}}{2\hbar\epsilon_0 V}}$ (ω_{ge} the $|g\rangle - |e\rangle$ transition frequency, and V the quantization volume), and ω is the difference between the signal field frequency and the frequency of the atomic transition $|g\rangle \rightarrow |e\rangle$ (with $\omega \rightarrow 0$ corresponding to the exact atom-field resonance). The imaginary part of the susceptibility describes absorptive properties of the medium (thereby modifying the signal-field intensity transmission coefficient T), whereas the real part determines the signal-field refractive index n:

$$T(\omega) = \exp\left[-\mathrm{Im}\chi(\omega)kL\right], \quad n(\omega) = 1 + \mathrm{Re}\chi(\omega)/2 \tag{1.5}$$

where k is the signal-field wave vector and L is the length of the medium. From these expressions, we see that EIT can be used to make a resonant, opaque medium transparent by means of quantum interference. Ideal transparency is obtained in the limit when the relaxation of the low-frequency (spin) coherence ($\gamma_{gs} = 0$) vanishes, in which case there is no absorption at atomic resonance (see Fig. 1.1(b)).

Many of the important properties of EIT result from the fragile nature of quantum interference in a medium that is initially opaque. Indeed, ideal transparency is

attained only at exact resonance, i.e., when the frequency detuning $\omega = 0$. Away from this resonance condition, the interference is not ideal and the medium becomes absorbing. The transparency spike that appears in the absorption spectrum is typically very narrow (kHz - MHz) in alkali vapors. At the same time the tolerance to frequency detuning (transparency window $\Delta\nu$) can be increased by using a stronger coupling field, as can be seen using Eq. (1.4).

For a signal field on resonance ($\omega = 0$) in an ideal EIT medium, the susceptibility vanishes and the refractive index is equal to unity. This means that the propagation velocity of a phase front (i.e., the phase velocity) is equal to that in vacuum. However, the narrow transparency resonance is accompanied by a very steep variation of the refractive index with frequency (see Fig. 1.1(b)). As a result, the envelope of a wave packet propagating in the medium moves with a group velocity v_g [42], where

$$v_g = \frac{c}{1 + g^2 N/|\Omega|^2}, \tag{1.6}$$

which can be much smaller than the speed of light in vacuum c. Note that v_g depends on the control field intensity and the atomic density: decreasing the control power or increasing the atomic density makes v_g slower, as demonstrated by Hau et al. [56] and then by others [23, 66]. The slowing achieved using these methods can be quite dramatic: for example, light propagation speeds of 17 m/s were observed in Ref. [56].

1.2.2 Dark-State Polaritons

In the previous section, we saw that the essential features of EIT can be understood using the linear susceptibility. In this section, we consider the experimentally relevant situation of a pulse of light traveling through an EIT medium. In this case, a very nice

physical picture emerges, in which the incident light pulse and the $|g\rangle - |s\rangle$ atomic coherence form a coupled excitation referred to as a dark-state polariton [42].

Consider the situation where a signal pulse is initially outside the medium. The front edge of the pulse then enters the medium and is rapidly decelerated. Being outside of the medium the back edge still propagates with vacuum speed c. As a result, upon entrance into the cell, the spatial extent of the pulse is compressed by the ratio c/v_g, while its peak amplitude remains unchanged. Clearly the energy of the light pulse is much smaller when it is inside the medium. Photons are used to establish the coherence between the states $|g\rangle$ and $|s\rangle$, or, in other words, to change the atomic state, with the excess energy carried away by the control field. As the signal pulse exits the medium, its spatial extent increases again and the atoms return to their original ground state; the pulse, however, is delayed as a whole by the group delay $\tau = \frac{L}{v_g} - \frac{L}{c}$, where L is the length of the EIT medium.

As previously mentioned, the propagation of the signal pulse without absorption occurs because the atoms occupy a specific superposition of the states $|g\rangle$ and $|s\rangle$ (a so-called "dark state") that prevents absorption to the state $|e\rangle$ via quantum interference between the absorption pathways $|g\rangle \rightarrow |e\rangle$ and $|s\rangle \rightarrow |e\rangle$. Inside the medium, the wave of atomic coherence (sometimes referred to as a "spin wave", where $|g\rangle$ = "spin down" and $|s\rangle$ = "spin up") propagates together with the signal pulse. The photons in the pulse are therefore strongly coupled to the atoms, with an associated quasiparticle called a dark-state polariton [42] that is a combined excitation of photons and atomic coherence. For the case when the decay rate of coherence between states $|g\rangle$ and $|s\rangle$ is negligible, we can describe the propagating signal by

the electric field operator $\hat{\mathcal{E}}(z,t) = \sum_k \hat{a}_k(t)e^{ikz}$, where the sum is over the free-space photonic modes with wave vectors k and corresponding bosonic operators $\hat{a}_k$. To describe the properties of the medium, we use collective atomic operators $\hat{\sigma}_{\mu\nu}(z,t) = \frac{1}{N_z}\sum_{j=1}^{N_z} |\mu_j\rangle\langle\nu_j|e^{-i\omega_{\mu\nu}t}$ averaged over small but macroscopic volumes containing $N_z \gg 1$ particles at position z [3].

In particular, the operator $\hat{\mathcal{P}}(z,t) = \sqrt{N}\hat{\sigma}_{ge}(z,t)$ describes the atomic polarization oscillating at an optical frequency, whereas the operator $\hat{\mathcal{S}}(z,t) = \sqrt{N}\hat{\sigma}_{gs}(z,t)$ corresponds to a low-frequency atomic coherence, or "spin wave". The control field is assumed to be strong and is treated classically. The atomic evolution is governed by a set of Heisenberg equations: $i\hbar\partial_t\hat{A} = \left[\hat{A}, \hat{H}\right]$, where $\hat{H}$ is the atom-field interaction Hamiltonian and $\hat{A} = \{\hat{\mathcal{P}}, \hat{\mathcal{S}}\}$. These equations can be simplified assuming that the signal field is weak and that Ω and $\hat{\mathcal{E}}$ change in time sufficiently slowly, i.e., adiabatically. To leading order in the signal field $\hat{\mathcal{E}}$ we find [3]

$$\hat{\mathcal{P}}(z,t) = -\frac{i}{\Omega}\partial_t\hat{\mathcal{S}}, \qquad \hat{\mathcal{S}}(z,t) = -\frac{g\sqrt{N}\hat{\mathcal{E}}}{\Omega}. \tag{1.7}$$

The evolution of the signal field is described by the Heisenberg equation

$$\left(\frac{\partial}{\partial t} + c\frac{\partial}{\partial z}\right)\hat{\mathcal{E}}(z,t) = ig\sqrt{N}\hat{\mathcal{P}}(z,t). \tag{1.8}$$

The solution of Eqs. (1.7) and (1.8) can be obtained by introducing a new quantum field $\hat{\Psi}(z,t)$ that is a superposition of photonic and atomic components:

$$\hat{\Psi}(z,t) = \cos\theta\hat{\mathcal{E}}(z,t) - \sin\theta\hat{\mathcal{S}}(z,t) \tag{1.9}$$

$$\cos\theta = \frac{\Omega}{\sqrt{\Omega^2 + g^2N}}, \quad \sin\theta = \frac{g\sqrt{N}}{\sqrt{\Omega^2 + g^2N}}. \tag{1.10}$$

The field $\hat{\Psi}(z,t)$, referred to as a dark-state polariton [42], obeys the equation of

motion:

$$\left[\frac{\partial}{\partial t} + c\cos^2\theta\frac{\partial}{\partial z}\right]\hat{\Psi}(z,t) \;=\; 0, \tag{1.11}$$

with solution

$$\hat{\Psi}(z,t) \;=\; \hat{\Psi}\left[z - c\int_0^t d\tau\cos^2\theta(\tau), t=0\right], \tag{1.12}$$

which describes shape-preserving propagation with velocity $v_g = c\cos^2\theta$ that is proportional to the magnitude of its photonic component.

1.2.3 EIT-based Quantum Memory

In this section, we show how the dark-state polariton picture described in the previous section allows control of polariton properties via the control laser intensity. Specifically, by dynamically reducing the control laser intensity to zero, the polariton velocity can be reduced to zero, with the excitation becoming completely atomic in nature. In this way, the incident photon pulse can be mapped onto the stationary atomic coherence (so-called "light storage"), allowing the atomic medium to serve as a memory for the quantum state of the incident photon.

From Eqs. (1.9) - (1.12), we see that the dark-state polariton is a coupled excitation of light and matter propagating at velocity $v_g = c\cos^2\theta$. This dependence of the polariton velocity on the control-field Rabi frequency Ω means that the polariton velocity can be controlled via the intensity of the control field. Moreover, from Eqs. (1.9) and (1.10), we see that as the velocity is reduced, the atomic contribution to the polariton grows, while the photonic component shrinks. As the control field intensity is reduced to zero [$\Omega(t) \to 0$], the group velocity is reduced to zero as

$\cos^2\theta \to 0$, and the polariton becomes entirely atomic in nature: $\hat{\Psi}(z,t) \to -\hat{\mathcal{S}}(z,t)$. This is the idea behind EIT-based "light storage" [103, 79].

At this point, the photonic quantum state is mapped onto long-lived ground states of the atoms. For large optical depth and zero ground-state decoherence ($\gamma_{gs} = 0$), the entire procedure has no loss and is completely coherent, as long as the storage process is sufficiently smooth [43]. The stored photonic state can be easily retrieved by simply reaccelerating the stopped polariton by turning the control field back on. In recent years, experiments have shown that weak classical light pulses can be stored and retrieved in optically thick atomic media using dynamic EIT [79, 103] and that the storage process preserves phase coherence [89], although significant work remains to optimize the fidelity [50, 101, 71] and storage time.

Theoretical studies [33] have shown that EIT propagation and quantum-state transfer using dynamic EIT preserves the nonclassical features of quantum states. This has been recently demonstrated experimentally for EIT propagation of squeezed vacuum field incident on an EIT medium [2]. This thesis presents experiments [35] (simultaneously demonstrated in Ref [26]) in which the quantum nature of single photons is shown to be preserved during EIT-based propagation, storage, and retrieval.

1.3 Quantum Control of Single Photons using Atomic Ensembles

In this section, we describe how EIT can be used to obtain quantum control of single photons using atomic ensembles. Specifically, in Section 1.3.1 we describe how

Raman scattering, single-photon detection, and EIT-based atomic-coherence retrieval can be used to conditionally generate single photons using atomic ensembles. We also describe how EIT with a dynamic control field intensity can be used to store and retrieve a single photon in an atomic ensemble, thus utilizing the atomic ensemble as a quantum memory. Finally, in Section 1.3.2, we describe how these techniques can be combined to realize quantum networks and long-distance quantum communication using atomic ensembles. The purpose of this section is to introduce the basic idea behind these methods; later chapters will describe their experimental implementation.

1.3.1 EIT-Based Single-Photon Generation and Storage

The idea behind EIT-based single photon generation is shown in Fig. 1.2. We consider an atomic ensemble of three-level "Λ-type" atoms, with two metastable ground states $|g\rangle$ and $|s\rangle$, and excited state $|e\rangle$. The first step is to create the desired atomic state by utilizing spontaneous Raman scattering combined with single-photon detection. An off-resonant laser, referred to as the "write" laser, is applied to an ensemble that has been optically pumped into the state $|g\rangle$, resulting in the spontaneous Raman scattering of so-called Stokes photons with a frequency less than that of the write laser by an amount equal to the $|g\rangle$ - $|s\rangle$ transition frequency. Ideally, conditioning on detection of a single Stokes photon at the single-photon detector ensures that only one atom in the ensemble has made the transition from the state $|g\rangle$ to the state $|s\rangle$. Moreover, since we do not know which of the N atoms addressed by the write laser is in the $|s\rangle$ state, by detecting a single Stokes photon, we project the atomic ensemble

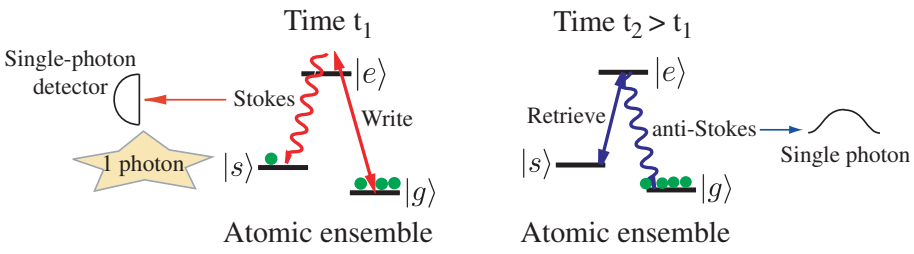

Figure 1.2: Basic idea behind EIT-based single-photon generation. In the first step at some time t_1, the write laser, which couples the states $|g\rangle$ and $|e\rangle$, is applied to an atomic ensemble that has been optically pumped into the state $|g\rangle$. This results in the spontaneous Raman scattering of a Stokes photon with a frequency less than that of the write laser by an amount equal to the $|s\rangle - |g\rangle$ transition frequency. By conditioning on detection of a single Stokes photon, the atomic ensemble is prepared in a state with a single excitation in the state $|s\rangle$. At some time $t_2 > t_1$, this atomic excitation is mapped onto a single photon (a so-called anti-Stokes photon resonant with the $|g\rangle - |e\rangle$ transition) by application of a retrieve laser resonant with the $|s\rangle - |e\rangle$ transition. The retrieve laser prevents the population in state $|g\rangle$ from absorbing the single anti-Stokes photon by acting as an EIT control laser.

onto the state

$$\frac{1}{\sqrt{N}} \sum_{i=1}^{N} |g_1\, g_2 \ldots g_{i-1}\, s_i\, g_{i+1} \ldots g_N\rangle\,. \tag{1.13}$$

That is, we create a collective atomic coherence, or spin wave, with a single excitation, where each atom has an equal probability of being in state $|s\rangle$. The momentum conservation equation

$$\mathbf{k}_{write} = \mathbf{k}_{Stokes} + \mathbf{k}_{spin}, \tag{1.14}$$

where $\mathbf{k}_{write}$, $\mathbf{k}_{Stokes}$, and $\mathbf{k}_{spin}$ are the wave vectors of the write laser, Stokes photon, and spin wave respectively, ensures that detecting Stokes photons in a small solid angle in the forward direction projects the atomic state onto a well-defined spin-wave mode.

After creating this atomic state, the atomic coherence is retrieved onto a single

photon pulse[1] using EIT, as shown in Fig. 1.2. A laser referred to as the "retrieve" laser is applied on resonance with the $|s\rangle$ - $|e\rangle$ transition, converting the atomic coherence into a dark-state polariton that propagates out of the medium and emerges as an anti-Stokes photon resonant with the $|g\rangle$ - $|e\rangle$ transition. The retrieve laser acts as an EIT control laser for the single anti-Stokes photon, preventing it from being absorbed by the large atomic population in state $|g\rangle$. The physics behind this is identical to that utilized in classical EIT "light storage" experiments [79, 103].

One advantage of generating single photons using EIT is that EIT allows a measure of control over the single-photon properties. For example, the retrieve laser intensity determines the width of the EIT transparency window (see Eq. (1.4) and Fig. 1.1(b)) and thus also determines the bandwidth of the single photons. In addition, the timing of the single-photon emission can be controlled via the turn-on time of the retrieve laser. Finally, the direction of the retrieve laser determines the direction of the single-photon emission via momentum conservation.

One can also imagine utilizing the coherent control enabled by EIT to create an atomic-ensemble based single-photon quantum memory. By sending a single photon produced in one ensemble to another ensemble, one can store the photon in the second ensemble by applying a dynamic EIT control field as discussed in Section 1.2.3. The single photon is then stored as an atomic coherence, and can be reconverted into a photon by reapplication of the EIT control field. Such a scheme could serve as the basis of a quantum network. Chapters 4 and 5 present experiments, based on these

[1]Strictly speaking, there is no such thing as a photon "pulse", or a "wavepacket for a photon" [113]. Nevertheless, the spatial localization produced by the photodetector does allow a "wave function" for the photon to be defined [100]. In this thesis, we adopt the operational definition in which the "photon pulse" amplitude is simply the probability amplitude for detection of the photon, but one should still treat the concept of a photon pulse with care [113, 90, 32, 78, 100].

ideas, that demonstrate a single-photon source, quantum memory, and a primitive quantum network using atomic ensembles.

1.3.2 Quantum Networks and Long-Distance Quantum Communication using Atomic Ensembles

Two potential applications of these techniques are now being actively explored: quantum networks and long-distance quantum communication. Much of the work on single-photon generation and storage using atomic ensembles has been motivated by the proposal by Duan, Lukin, Cirac and Zoller for long-distance quantum communication [34], hereafter referred to as the DLCZ proposal. This proposal is based on earlier theoretical suggestions [77, 88] for storing photonic states in atomic ensembles [83]. Figure 1.3 illustrates how the Raman scattering scheme described in the previous section can be used to implement the backbone of this protocol - the probabilistic generation of quantum entanglement of two atomic ensembles using an absorbing photonic channel. The two ensembles are illuminated by synchronized classical pump pulses. The forward-scattered Stokes photons interfere at a 50%-50% beam splitter, with the outputs detected respectively, by two single-photon detectors. The basic idea is that in such a configuration a single detector click implies that one quantum of spin excitation has been created in one of the two ensembles, but it is fundamentally impossible to determine from which of the two ensembles the photon was emitted. In this case, the measurement projects the state onto an entangled state

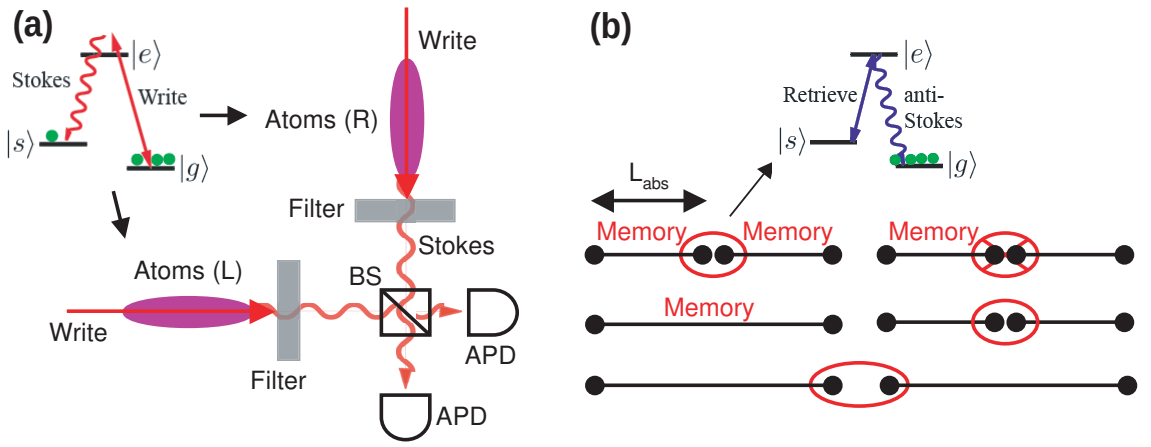

Figure 1.3: Atomic-ensemble based quantum repeater. **(a)** First step: entanglement generation. Interference of spontaneous Stokes photons from two ensembles (R and L) on a beam-splitter (BS) leads to generation of entanglement between the corresponding modes in the ensembles, provided a single Stokes photon was detected in one of the avalanche photo detectors (APD). If zero or more than one photons are detected, the process must be repeated. **(b)** Second step: entanglement swapping. The entanglement between atomic ensembles created over a characteristic absorption length L_{abs} in the first step, indicated here by filled circles connected by a line, is extended to two absorption lengths via entanglement swapping. Entanglement swapping is accomplished by interference of retrieved anti-Stokes photons on a beam splitter and detection as in (a), provided a single anti-Stokes photon has been measured.

of the two ensembles of the form

$$\frac{1}{\sqrt{2}}\left(|0\rangle_L|1\rangle_R + e^{i\phi}|1\rangle_L|0\rangle_R\right), \tag{1.15}$$

where $L(R)$ labels the left (right) ensemble, $|n\rangle_i$ denotes n atomic excitations in ensemble i, and ϕ denotes an unknown phase-shift difference between the left and right channels [34].

The most remarkable feature of the above process is that it can be made robust with respect to imperfections and losses during the optical propagation. In particular, when the total losses in both left and right optical paths are equal, the loss will affect only the overall probability of success but not the purity of the resulting state condi-

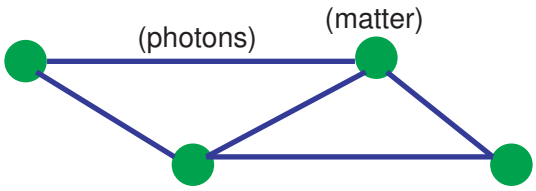

Figure 1.4: Quantum network. Green circles represent matter-based storage and processing nodes. Blue lines represent photonic quantum-transmission lines.

tioned on the detection of a single Stokes photon. These techniques for probabilistic manipulation of atomic ensembles may have interesting applications for long-distance quantum communication over realistic photonic channels, where absorption leads to an exponential decrease of the signal.

Fig. 1.3(b) demonstrates how this generated entanglement, combined with the nonzero decoherence time of the $|g\rangle - |s\rangle$ coherence and the EIT-based retrieval of this coherence, can be used to efficiently extend this entanglement to large distances. The entanglement between atomic ensembles created over a characteristic absorption length L_{abs} in the first step, indicated by filled circles connected by a line, is extended to two absorption lengths via entanglement swapping. By repeating this process, long-distance entanglement is created. Entanglement swapping is accomplished by interference of retrieved anti-Stokes photons on a beam splitter and detection as in Fig. 1.3(a), provided a single anti-Stokes photon has been measured. In such a probabilistic scheme, the "memory", i.e., the nonzero decay time of the $|g\rangle - |s\rangle$ coherence, is essential for polynomial scaling of the required time with distance, compared to exponential scaling for the case of direct entanglement generation [34].

The ability to transmit quantum information between remote locations using photons, combined with EIT-based atomic memory for photons, allows for the realization

of quantum networks, as shown in Fig. 1.4. Photons, which travel quickly and interact weakly with the environment, are ideal candidates to transmit quantum information; matter, which is stationary and allows EIT-based storage of photonic information, is an ideal candidate for long-term storage and processing. Quantum networks will likely play an integral role in any future realization of quantum computation or communication. Chapter 5 describes experiments [35] demonstrating a primitive two-node quantum network using two room-temperature atomic ensembles of ^{87}Rb.

1.4 Progress towards Long-Distance Quantum Communication using Atomic Ensembles

The first proposal for long-distance quantum communication using atomic ensembles was published in 2001 [34]. Since then, experimental demonstrations of the basic ingredients of this technique have been rapid, leading to a dynamic, fast-paced field of investigation.

The first experimental demonstration of these ideas was achieved simultaneously by two groups in 2003. Jeff Kimble's group at Caltech demonstrated nonclassical photon-number correlations between the two photon fields associated with the generation and retrieval of atomic coherences in a Cs magneto-optical trap (MOT), in the pulsed regime at the single-photon level [76]. Simultaneously, our group at Harvard demonstrated (see Chapter 2) nonclassical relative intensity correlations between the two photon fields associated with the generation and retrieval of atomic coherences in a warm ^{87}Rb atomic vapor in the continuous-wave regime at the level of a few

microwatts [118].

In 2004 G.-C. Guo's group in China reported nonclassical correlations between the two photon fields associated with the generation and retrieval of atomic coherences in the pulsed regime at the single-photon level in a room-temperature atomic vapor of ^{87}Rb atoms with 30 Torr of Ne buffer gas [64]. Conditional single-photon generation produced by retrieving a stored excitation in a MOT of Cs atoms was then demonstrated by the Caltech group [30]. In addition, Alex Kuzmich's group at Georgia Tech demonstrated the quantum state transfer between matter and light in a MOT of cold ^{85}Rb atoms by measuring polarization correlations between the photons associated with the generation and retrieval of atomic coherences [94]. Experiments in our group (see Chapter 3) demonstrated nonclassical photon-number correlations at the single-photon level, conditional generation of nonclassical photon states, and the ability to use EIT-based retrieval to control the timing and bandwidth of these pulses, all in a warm vapor of ^{87}Rb atoms [37].

In 2005, Steve Harris's group at Stanford demonstrated the creation of counter-propagating nonclassically correlated pairs of photons with controllable waveforms at a rate of 12,000 pairs per second using a MOT of cold ^{87}Rb [9]. This experiment was also the first to work in the regime where the intensity of the retrieve laser causes a Rabi-flopping which manifests itself in oscillations of the correlations in time. The Georgia Tech group then demonstrated entanglement between a photon and a collective atomic excitation in a MOT of cold ^{85}Rb atoms by measuring polarization correlations between the photons emitted during creation and retrieval of the atomic excitation [95]. In addition, Vladan Vuletić's group at MIT created quantized spin

gratings by single-photon detection, and converted these gratings on-demand into photons with retrieval efficiencies exceeding 40% (80%) for single (a few) quanta. In December of 2005, three papers were published, each of which took an important step toward the realization of the DLCZ scheme. The first paper [29], published by the Caltech group, was the first observation of measurement-induced entanglement between two atomic ensembles (MOTs of Cs atoms, in this case), as suggested by the DLCZ proposal [34], and as illustrated in Fig. 1.3(a). The other two papers each demonstrated the preservation of the quantum nature of single photons created in one atomic ensemble after being stored in and retrieved from a second atomic ensemble using EIT. The Georgia Tech group accomplished this in MOTs of cold ^{85}Rb atoms [26]. Our group performed these experiments (as described in Chapters 4 and 5) using room-temperature ensembles of ^{87}Rb atoms [35].

Finally, in 2006, the Georgia Tech group entangled two MOTs of ^{85}Rb atoms [93], using EIT-based storage of single photons to generate the entanglement, rather than the method suggested in the DLCZ proposal [34].

In addition to applications in quantum communication, the experimental demonstration of EIT at the single-photon level [35, 26] opens the way for investigations into controlled nonlinear interactions between quantum pulses of light. For example, Axel André and co-workers recently suggested combining the techniques of EIT-based stationary pulses of light [8] with resonantly enhanced Kerr nonlinearities to create efficient nonlinear interaction between two single-photon pulses [1]. This proposal is an extension of earlier theoretical work by Atac Imamoğlu and co-workers [85, 86]. Demonstration of EIT at the single-photon level is an important step toward realizing

these proposals for nonlinear interaction between two single-photon pulses.

All these developments indicate that the coming years will witness exciting experimental developments in the applications of EIT-based techniques to quantum communication and controlled nonlinear interactions of quantum pulses of light.

1.5 Overview

This thesis presents experiments that realize basic building blocks of the DLCZ protocol by utilizing EIT in atomic ensembles for the control of quantum pulses of light. Chapter 2 describes experiments utilizing Raman scattering and EIT-based retrieval of atomic excitations to generate nonclassically correlated photon pulses using atomic enembles [118]. In these experiments, the time delay between the pulses is coherently controlled via storage of photonic states in an ensemble of ^{87}Rb atoms. Chapter 3 describes experiments demonstrating a novel approach for conditionally generating nonclassical pulses of light with controllable photon numbers, propagation direction, timing, and pulse shapes [37]. Spatio-temporal control over the pulses is obtained by exploiting long-lived coherent memory for photon states and EIT in an optically dense atomic medium. We observe EIT-based generation and shaping of few-photon light pulses, and also observe nonclassical correlations in relative photon number between the Raman scattered photon pulses and the retrieved photon pulses. Chapter 4 demonstrates conditional generation of single photons with tunable frequency, timing, and bandwidth using a room-temperature atomic ensemble of ^{87}Rb [35]. Chapter 5 demonstrates a primitive quantum network by transmitting these single photons from the "source" ensemble in which they are created, to a second

"target" atomic ensemble, where we then use EIT to store them in atomic coherences, and retrieve these coherences back onto a photonic field at a later time [35]. We probe the spectral and quantum statistical properties of narrow-bandwidth single-photon pulses, revealing that their quantum nature is preserved under EIT propagation and storage. Finally, we measure the time delay associated with the reduced group velocity of the single-photon pulses and report observations of their storage and retrieval.

Chapter 2

Generation of Correlated Photon States using Atomic Ensembles

2.1 Introduction

In this chapter, we describe a proof-of-principle demonstration of a technique in which two correlated light pulses can be generated with a time delay that is coherently controlled via the storage of quantum photonic states in an ensemble of ^{87}Rb atoms. This resonant nonlinear optical technique is an important element of the DLCZ long-distance quantum communication proposal [34] described in the previous chapter.

2.2 Generating Correlated Photon States

Fig. A.1 in Appendix A.1 shows the full atomic level structure for the D_1 line ($5^2S_{1/2} \rightarrow 5^2P_{1/2}$) of ^{87}Rb, the transition used in our experiments. By using magnetic

shielding, the magnetic field experienced by the atoms is zero, meaning that the Zeeman states within each hyperfine level are degenerate. Our experiments can be understood qualitatively by considering a three-state "Λ configuration" of atomic states coupled by a pair of optical control fields (see Fig. 2.1(a)), where $|e\rangle$ represents the two hyperfine levels $|5^2P_{1/2}, F' = 1\rangle$ and $|5^2P_{1/2}, F' = 2\rangle$, $|g\rangle = |5^2S_{1/2}, F = 1\rangle$, and $|s\rangle = |5^2S_{1/2}, F = 2\rangle$.

To begin, a large ensemble of atoms is optically pumped into the ground state $|g\rangle$ ("spin down"). Atomic excitations to the state $|s\rangle$ ("spin up") are produced via spontaneous Raman scattering [106], induced by an off-resonant control beam with Rabi frequency Ω_W and detuning Δ_W, which we refer to as the write beam. In this process correlated pairs of frequency shifted photons (so-called Stokes photons) and flipped atomic "spins" are created (corresponding to atomic Raman transitions into the state $|s\rangle$). Energy and momentum conservation ensure that for each Stokes photon emitted in a particular direction, there exists exactly one flipped spin quantum in a well-defined spin-wave mode. As a result, the number of spin-wave quanta in a given mode and the number of photons in the Stokes field are strongly correlated. These atom-photon correlations closely resemble those between two electromagnetic field modes in parametric down-conversion [55, 62]. This Raman process creates a Stokes signal field (S), and a small population in the $|s\rangle$ state with a corresponding $|g\rangle\langle s|$ coherence. In addition, the momentum conservation equation

$$\mathbf{k}_{write} = \mathbf{k}_{Stokes} + \mathbf{k}_{spin}, \tag{2.1}$$

where $\mathbf{k}_{write}$, $\mathbf{k}_{Stokes}$, and $\mathbf{k}_{spin}$ are the wave vectors of the write laser, Stokes photon, and spin wave respectively, ensures that the Stokes photons detected in a small solid

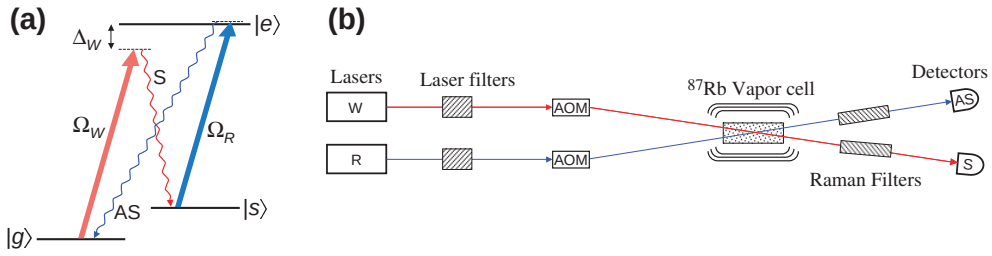

Figure 2.1: Atomic-level configuration and experimental setup. **(a)** ^{87}Rb levels used in the experiments (D_1 line, Zeeman sublevels and excited-state splitting are not shown in this simplified scheme, the ground-state hyperfine splitting is 6.835 GHz). Optical pumping prepares the atoms in the $|g\rangle = |5^2S_{1/2}, F = 1\rangle$ state. The write step (red) is a spontaneous Raman transition into the $|s\rangle = |5^2S_{1/2}, F = 2\rangle$ state. The transition is induced with a control beam with Rabi frequency Ω_W that couples $|g\rangle$ with detuning Δ_W to the excited state $|e\rangle$ (two nearly degenerate hyperfine levels $|5^2P_{1/2}, F' = 1\rangle$ and $|5^2P_{1/2}, F' = 2\rangle$). In the retrieve step (blue) this coherence is mapped back into an anti-Stokes field (AS) via a second Raman transition induced with a near-resonant retrieve control beam with Rabi frequency Ω_R. **(b)** Schematic of the experimental setup. Two lasers provide the write (W) and retrieve (R) control beams, with acousto-optic pulse modulation (AOM).

angle in the forward direction are correlated with a well-defined spin-wave mode.

In order to probe the state stored in the spin wave, it can then be retrieved with a second Raman transition: a coherent conversion of the atomic state into a different light beam (referred to as the anti-Stokes field) is accomplished by applying a second control laser (the retrieve laser) with Rabi frequency Ω_R (Fig. 2.1(a)). This retrieval process is not spontaneous; rather it results from the atomic spin coherence interacting with the retrieve laser to generate the anti-Stokes field. As mentioned in the the previous chapter, the physical mechanism for this process is identical to the retrieval of weak classical input pulses [42] discussed in the context of "light storage" experiments [79, 103]. Due to the suppression of resonant absorption associated with EIT, the retrieved anti-Stokes field is not reabsorbed by the optically dense cloud of

atoms. Hence, this retrieval process allows, in principle, for an ideal mapping of the quantum state of a spin wave onto a propagating anti-Stokes field, which is delayed but otherwise identical to the Stokes field in terms of photon-number correlations. The variable delay (storage time) and the rate of retrieval are controlled by the timing and the intensity of the retrieve beam.

We explore relative intensity correlations between the photon fields associated with the preparation (Stokes) and the retrieval (anti-Stokes) of the atomic state. The onset of quantum-mechanical correlations between the photon numbers of the Stokes and delayed anti-Stokes light (analogous to twin-mode photon-number squeezing [6, 114]) provides evidence for the storage and retrieval of nonclassical atomic states. The storage states used in our experiments are the long-lived hyperfine sublevels of the electronic ground state, $|g\rangle = \left|5^2S_{1/2}, F = 1\right\rangle$ and $|s\rangle = \left|5^2S_{1/2}, F = 2\right\rangle$.

2.2.1 Experimental Setup

A schematic of the experimental apparatus is shown in Fig. 2.1(b). The volumes of the write and retrieve lasers overlap in the ^{87}Rb vapor cell. The intensities of these lasers are modulated with acousto-optic modulators (AOMs). The Stokes (anti-Stokes) field co-propagates with the write (retrieve) control laser, and a small angle ($\sim 3\,\mathrm{mrad}$) between the control lasers allows for spatially separated detection of the Stokes and anti-Stokes signals. The vapor cell is placed in an oven inside three layers of magnetic shielding, allowing control of the atomic density via temperature, and zeroing of the magnetic field.

A warm ^{87}Rb vapor cell with external anti-reflection coated windows and a length

of 4 cm is maintained at a temperature of typically $\approx$ 85°C, corresponding to an atom number density of $\approx 10^{12}$ cm^{-3} (see Fig. A.2 in Appendix A.1). The hyperfine coherence time is in practice limited by atoms diffusing out of the beam volume, and is enhanced with a buffer gas (we used cells with 3 and 4 Torr Ne), resulting in measured atomic coherence lifetimes in the μs range. This agrees well with calculated diffusion times out of beam diameters of ~ 0.5 mm and 4 Torr of Ne buffer gas [119], corresponding to our experimental conditions (see Appendix A.1 for details).

Two extended-cavity diode lasers provide the write and retrieve control beams. The control beams have typical powers of 0.7 mW (write) and 3.2 mW (retrieve) and are focused in the cell to diameters of about 0.5 mm. The relevant number of atoms interacting with the laser beams along the cell length is about $10^9 - 10^{10}$. The write laser was typically tuned about $\Delta_W \sim +1$GHz away from resonance with the $F = 1 \rightarrow F' = 2$ transition of the D_1 absorption line ($|g\rangle \rightarrow |e\rangle$ transition in Fig. 2.1(a)), while the retrieve laser was tuned near resonance with the $F = 2 \rightarrow F' = 2$ transition ($|s\rangle \rightarrow |e\rangle$ in Fig. 2.1(a)). The retrieve laser was also used for preparation of the atoms into the ground state $|g\rangle$ via optical pumping.

Filters following each laser are used to suppress the spontaneous emission background and spurious modes of the lasers. Since both the write and retrieve beams are generated using diode lasers, the spontaneous emission background typically spans ~ 10 nm. The broad bandwidth of this noise means it cannot be easily filtered, and therefore can propagate through the setup to our detectors. Reflecting the lasers from diffraction gratings converts these different frequencies to different spatial positions. By selecting only a small portion of this spatial distribution with a pinhole, we were

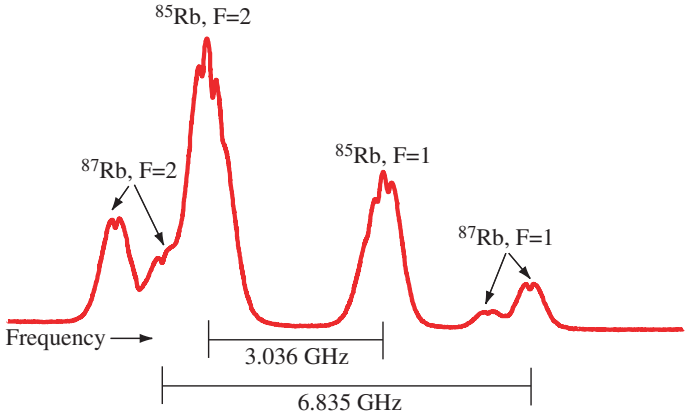

Figure 2.2: Fluorescence as a function of frequency for the D_1 line ($5^2S_{1/2} \rightarrow 5^2P_{1/2}$) of rubidium. Rubidium vapor is at room temperature and thus the transitions are Doppler-broadened. The splitting of the $\left|5^2S_{1/2}\right\rangle$ state for ^{85}Rb and ^{87}Rb is 3.036 GHz and 6.835 GHz respectively [119]. Peaks are labeled by the $\left|5^2S_{1/2}\right\rangle$ state from which the atoms are excited.

able to reduce the spontaneous emission noise bandwidth from $\sim 10\,\text{nm}$ to $\sim 100\,\text{GHz}$ ($\sim 0.21\,\text{nm}$) .

In general, we observed spontaneous Raman signals for both linear and circular polarizations of the control beams. Filters following the vapor cell block the transmitted control beams so that only Raman fields reach the detectors. For different experimental circumstances, we used filters based on isotopically pure ^{85}Rb absorption cells or crystal polarizers. For example, ^{85}Rb absorption cells were used to absorb the write and retrieve lasers and transmit the Stokes and anti-Stokes fields when the detunings of the write and retrieve lasers put them on resonance with ^{85}Rb. Fig. 2.2, which displays the fluorescence spectrum of rubidium, illustrates this principle. Since the write (retrieve) laser and the Stokes (anti-Stokes) field are separated in frequency by the $|g\rangle - |s\rangle$ frequency difference of 6.835 GHz, but the ground-state splitting of

^{85}Rb is only 3.036 GHz [119], the write (retrieve) laser can be detuned such that it is absorbed by ^{85}Rb , while the Stokes (anti-Stokes) photon is not resonant with ^{85}Rb .

Under conditions where the write or retrieve laser was not on resonance with ^{85}Rb, crystal polarizers were used to achieve the filtering. In this case, we utilized a Lin || Lin polarization configuration for the write and retrieve lasers, meaning they are both linearly polarized, and in the same direction. We observed that the scattered Stokes (anti-Stokes) photons that are emitted are primarily polarized orthogonally to the write (retrieve) laser polarization. Therefore, by placing a polarizing beamsplitter (PBS) after the ^{87}Rb cell in both the Stokes and anti-Stokes channels, the Stokes (anti-Stokes) and write (retrieve) fields can be separated to 1 part in 10^5, limited by the quality of the PBS [1]. The physics underlying the orthogonal polarizations of the Stokes (anti-Stokes) compared to the write (retrieve) has been explored theoretically. It is seen to result from a destructive interference for the production of Stokes (anti-Stokes) photons with the same polarization as the write (retrieve) laser when the full ^{87}Rb atomic-level structure (see Fig. A.1) is considered [60].

In addition to filtering based on frequency and polarization, it was also possible to spatially separate the Stokes (anti-Stokes) photons from the write (retrieve) laser to some degree by utilizing phase matching [15, 3, 98]. Fig. 2.3 shows the transverse spatial position of the retrieve laser and anti-Stokes field in the far-field, as imaged with a CCD camera. We observe that as the angle between the write and retrieve lasers (see Fig. 2.1) is increased, the angle between the anti-Stokes photons and retrieve laser increases. For large enough angles, the separation is large enough to

[1] In our experiments, each PBS is a beam-splitting Glan-Thompson crystal polarizer made of two cemented prisms of calcite

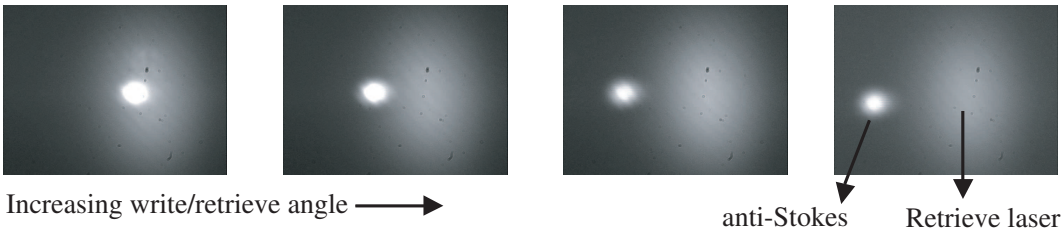

Figure 2.3: Transverse spatial position of the retrieve laser and anti-Stokes field in the far-field, as imaged with a CCD camera. Moving left to right, each picture was taken for successively larger angles between the write and retrieve lasers.

allow some degree of spatial filtering of the retrieve laser by selectively transmitting the anti-Stokes field with an aperture.

To detect the Raman (Stokes and anti-Stokes) fields, we used home-built detectors based on high-efficiency low-capacitance Si photo-diodes placed in low current-noise transimpedance amplifier circuits (see Appendix A.2 for details). The measured quantum efficiency was about 88%. Scanning Fabry-Perot etalons and beatnote detection of the Raman fields in the presence of the two transmitted control beams (i.e., without the Raman filters) were used for identifying the Raman modes. For small angles between the write and retrieve lasers, we only observed detectable Stokes (anti-Stokes) fields in narrow conical volumes near the write (retrieve) laser (see Fig. 2.3). This directionality is associated with a long pencil-shaped Raman gain medium (formed by the optically-pumped $|g\rangle$-state atoms dressed by the write beam), and is closely related to the concept of collective enhancement [34].

2.2.2 Continuous-Wave Regime

We first present the results of simultaneous, continuous-wave (cw) excitation by both the write and retrieve control beams. Fig. 2.4 presents an example of synchronously detected signals at the Stokes and anti-Stokes frequencies (Fig. 2.1(a)) in modes that co-propagate with the control beams. The observed Stokes light (Fig. 2.4(a)) is a sequence of spontaneous pulses, each containing a macroscopic number of photons, but with significantly fluctuating intensities and durations. The noisy character of the signals results from the thermal photon statistics (described by a Bose-Einstein distribution) of the spontaneous Stokes mode (see Refs. [91, 108] and Appendix A.3). The bandwidth of the fluctuations is limited by the Raman process (not by the detection bandwidth). The pulses were observed to have $10^3 - 10^7$ photons per pulse, with an average depending on the write beam intensity and detuning, and the atomic density. We estimate that the Raman gain coefficient could be varied over a broad range from $\approx e^1$ to e^{20} by relatively small changes of these parameters [106, 84].

The observation of fluctuations with thermal photon-number statistics (see Appendix A.3 and also Fig. 2.5(c)) indicates that the transverse mode structure of the Raman fields is approximated reasonably well by one, or at most a few, spatial modes [106]. In essence, each pulse corresponds to a spontaneously emitted Stokes photon that subsequently stimulates the emission of a number of other photons. As each Stokes photon emission results in an atomic transition from the state $|g\rangle$ into the spin-flipped state $|s\rangle$, the Stokes light fluctuations are mirrored in the anti-Stokes light, as shown in Fig. 2.4(b). Striking intensity correlations between the two beams

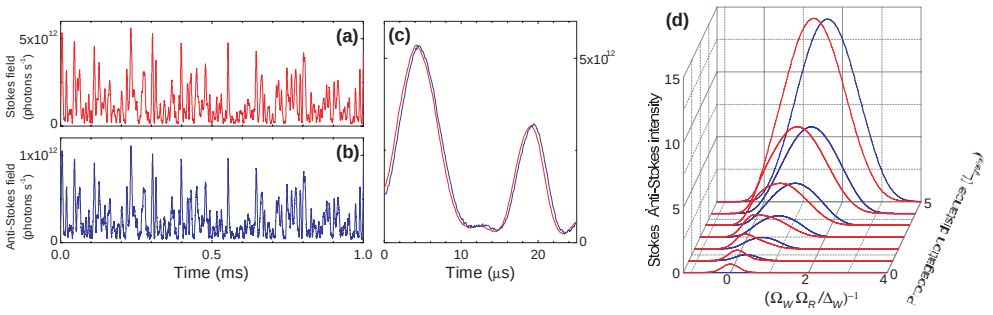

Figure 2.4: Correlations in the continuous-wave regime. Synchronously detected Stokes **(a)** and anti-Stokes **(b)** signals showing strong intensity correlations. The Raman transitions are induced with continuous-wave control beams. **(c)** The first 25 μs of the traces in (a) and (b). The Stokes signal (red) is plotted as in (a), the anti-Stokes signal (blue) is multiplied by 5.167 and given a small intensity offset (to correct for a weak constant background signal from the control beam leaking through the filter) to match the Stokes signal. **(d)** Theoretically simulated propagation dynamics of Stokes (red) and corresponding anti-Stokes (blue) intensities in the continuous-wave excitation regime. The propagation distance is in units of the four-wave mixing gain length $L_{gain} = v_g(\Omega_W\Omega_R/\Delta_W)^{-1}$, and time is in units of the inverse Raman bandwidth $(\Omega_W\Omega_R/\Delta_W)^{-1}$, see Refs. [84, 3] and Fig. 2.1(a).

are evident. The ratio between the observed Stokes and anti-Stokes fields was generally smaller than unity, due to incomplete retrieval. We experimentally determined that the observed retrieval efficiency $(10\% - 30\%)$ was limited by (in order of decreasing relevance): imperfect spatial mode matching, power limitation of our retrieve beam laser, and the ground-state coherence time.

These observations can be viewed as resulting from a resonant four-wave frequency mixing process in a highly dispersive medium [87, 58]. A high degree of intensity correlations is common for nonlinear parametric processes, as is well-known in the case of parametric down-conversion [55, 6, 114, 57]. However, the effect demonstrated here has one important distinction. In down-conversion, photon pairs are emitted simultaneously to an exceptionally high accuracy [62]. Close examination of the data

in Fig. 2.4(c) indicates that this is not true in the present case: the anti-Stokes fluctuations are delayed with respect to Stokes fluctuations. Experimentally, this delay could be varied in the range of 50 ns to about 1 μs; for example, increasing the intensity of the retrieve beam resulted in a smaller delay.

The delay in Fig. 2.4 (here measured to be 292 ns) corresponds to the finite time required for the retrieve laser to convert the $|g\rangle\langle s|$ atomic coherence into anti-Stokes light. To further illustrate this point, we have theoretically analyzed [3] the propagation dynamics of a fluctuation of the Stokes field in the presence of cw control beams (Fig. 2.4(d)). In these calculations, an initial Stokes fluctuation propagates and evolves into an amplified pair of Stokes and anti-Stokes light pulses with locked propagation. This semiclassical simulation represents the solution of a boundary-value problem, and is based on Eqs.(38-41,48,49) of Ref. [84], in which the effect of group velocities are included. The intensities are normalized to the amplitude of the initial Stokes fluctuation. The simulations assume non-decaying spin coherence, resulting in 100% retrieval efficiency.

At the beginning of the retrieval process, during the time required to convert the $|g\rangle\langle s|$ atomic coherence into anti-Stokes light, the group velocity of the Stokes field is close to the speed of light in vacuum c, whereas the group velocity v_g of the near-resonant anti-Stokes field is greatly reduced ($v_g \ll c$), since it propagates under EIT conditions. After this initial retrieval stage, the two pulses lock together and propagate with equal group velocities, being simultaneously amplified further in a four-wave mixing process. Thus, the observed delay corresponds to a storage of the excitation in atomic states. Theoretical estimates from Fig. 2.4(d) for parameters

corresponding to our experiment yield delays in the 100 ns - 1 μs range, comparable with the experimental observations.

2.2.3 Pulsed Regime

The essential feature of the present technique is that the delay and hence the storage time can be controlled using time-varying write and retrieve control beams. Fig. 2.5 presents the results of pulsed experiments in which a write pulse is followed by a retrieve pulse after a controlled time delay. The retrieve control laser is first used for optical pumping, followed by sequential write and retrieve control pulses that do not overlap in time, and which create and retrieve Stokes and anti-Stokes signals, respectively (see Fig. 2.5(e)). We find again that, at fixed control pulse intensities and durations, the Stokes and anti-Stokes pulses strongly fluctuate from pulse to pulse in a highly correlated manner (see Fig. 2.5(a) and (b)).

As a control experiment, we confirmed that without the write control pulse or without the optical pumping pulse, both the Stokes and anti-Stokes signals vanish. In addition, removing the retrieve control pulse after the write control pulse showed results with only Stokes signals. In these plots, weak background signals from control beams leaking through the filters are subtracted; the signal pulse shapes are limited by the detection bandwidth. Previous related experiments have been carried out for weak, coherent, classical pulses [79, 103]; our results demonstrate storage and retrieval of a spontaneously created hyperfine coherence.

Fig. 2.5(c) displays a histogram of the measured Stokes pulse energies. The distribution closely resembles a negative exponential as a function of pulse energy, con-

firming thermal photon-number statistics of the spontaneous Stokes transition (see Appendix A.3). This indicates that the transverse mode structure of the Raman fields is approximated reasonably well by one, or at most a few, spatial modes [106].

Fig. 2.5(d) plots the retrieval efficiency (ratio between the average energy in anti-Stokes and Stokes pulses) as a function of the time delay between the end of the write control pulse and the onset of the retrieve control pulse. The exponential decay in retrieve efficiency, with a characteristic 1/e time of $\sim 0.5\,\mu$s and observable retrieve signal out to $\sim 4\,\mu$s, agrees with the time scale for the atomic-diffusion limited coherence time expected for our experimental parameters (see Appendix A.1).

Fig. 2.6 presents data from the same experimental run as Fig. 2.5 in a slightly different form. The index $i = 1, 2, ..., 8$ labels consecutive realizations of pulsed experiments in which a write pulse is followed by a retrieve pulse after a controlled time delay. Each of the eight realizations have identical experimental parameters. We see again that at fixed control pulse intensities and durations, the Stokes pulse energy has large fluctuations from run to run, and that these fluctuations are strongly correlated with those of the anti-Stokes pulses. In the next section, we turn to the task of quantifying the strength of these correlations.

2.3 Observation of Correlations

We now turn to investigating the degree of correlations in relative intensity between the Stokes and anti-Stokes fields. In order to do this, we first need a method for quantifying the degree of the correlations; we introduce these methods in Section 2.3.1. In Section 2.3.2, we present data demonstrating nonclassical correlations

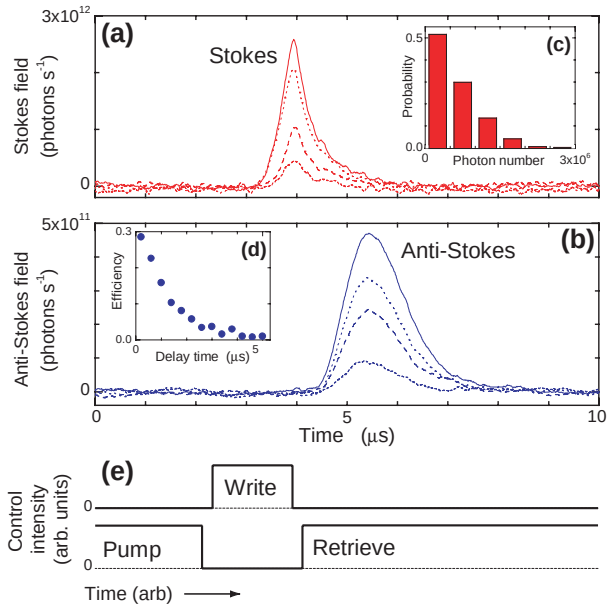

Figure 2.5: Correlations in the pulsed regime. Spontaneous Stokes signals **(a)** and retrieved anti-Stokes signals **(b)** obtained with pulsed control beams. The traces in panel (e) represent the modulation of the control beams. Consecutive realizations of the experiment with identical control parameters (solid, dotted, etc.) show strong fluctuations in the Stokes signal pulse energy, and correlated fluctuations in the anti-Stokes pulse. **(c)** Histogram of Stokes pulse energies. **(d)** Retrieval efficiency (ratio between the average energy in anti-Stokes and Stokes pulses) as a function of the time delay between the end of the write control pulse and the onset of the retrieve control pulse. **(e)** Modulation of the control beams as a function of time.

in the cw regime in the frequency domain.

2.3.1 Quantifying Correlations

Introduction

When the number of photons in two modes of light are measured in a repetitive manner (with paired results n_1 and n_2), the statistical criterion for correlations (here

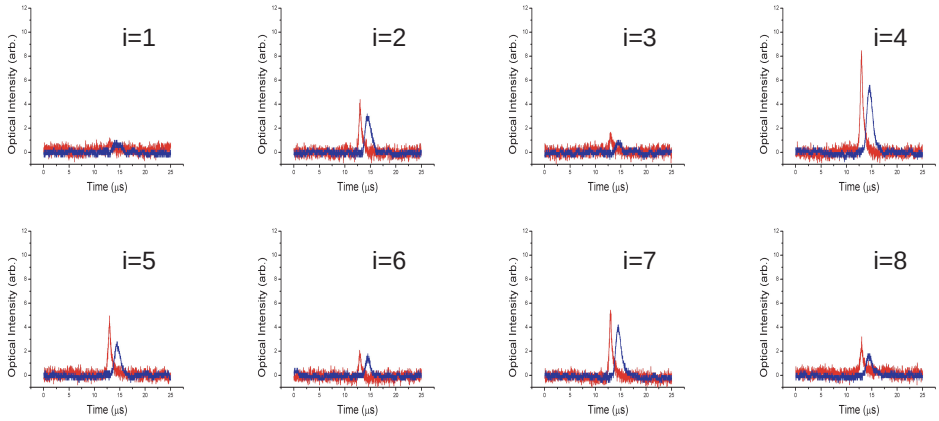

Figure 2.6: Fluctuations and correlations in the pulsed regime. Spontaneous Stokes signals (red) and retrieved anti-Stokes signals (blue) from light storage with pulsed control beams. The modulation of the control beams is the same as in Fig. 2.5(e). The index $i = 1, 2, ..., 8$ labels consecutive realizations of the experiment with identical control parameters, showing strong fluctuations in the Stokes signal pulse energy, and correlated fluctuations in the anti-Stokes pulse. Anti-Stokes pulses have been multiplied by the factor 5.

termed classical correlations) between n_1 and n_2 is

$$\mathrm{Var}(n_1 - n_2) < \mathrm{Var}(n_1) + \mathrm{Var}(n_2)\,, \tag{2.2}$$

where $\mathrm{Var}(x) \equiv \langle x^2 \rangle - \langle x \rangle^2$ denotes the variance of a set of measurements $x \equiv \{x_1, x_2, ...\}$. This makes sense, since for two completely independent signals x and y, $\mathrm{Var}(x - y) = \mathrm{Var}(x) + \mathrm{Var}(y)$. Therefore, any value of $\mathrm{Var}(x - y)$ less than this uncorrelated value indicates that the signals are correlated to some degree, a condition referred to as being classically correlated. A repetitive measurement on a single classical mode of light with average photon number $\langle n \rangle = \overline{n}$ yields a variance $\mathrm{Var}(n) \geqq \overline{n}$, due to quantum fluctuations with $\mathrm{Var}(n) = \langle n \rangle$ in the photon number of the mode. The case $\mathrm{Var}(n) = \overline{n}$ holds for a coherent state, which has Poissonian photon statistics, and is referred to as the standard quantum limit of noise (see

Appendix A.3 and Refs. [124, 109]). The standard quantum limit represents the minimum possible fluctuations according to the classical theory of electromagnetism. Accordingly, one can define that two modes of light have nonclassical correlations when for paired measurements n_1 and n_2

$$\mathrm{Var}(n_1 - n_2) < \overline{n}_1 + \overline{n}_2 \,, \tag{2.3}$$

and meeting this criterion is known as twin-mode intensity squeezing [6]. To summarize, two modes of light with recorded photon number statistics satisfying Eq. (2.2) are said to exhibit classical correlations; two modes satisfying Eq. (2.3) are said to be nonclassically correlated, or to exhibit twin-mode intensity squeezing.

The two Raman fields (Stokes and anti-Stokes) in light-storage experiments as presented in the previous sections are predicted to show such twin-mode intensity squeezing. However, to date, due to to losses and inefficiencies in the retrieval process, the measured values $\overline{n}_1 \neq \overline{n}_2$ (Fig. 2.4). While this inefficiency can probably be improved, in many future experiments losses and other imperfections will remain, causing significant differences between observed values of $\overline{n}_1$ and $\overline{n}_2$ in experiments where they are in principle equal. Furthermore, spontaneous Raman modes have thermal photon statistics (i.e., large excess noise [124, 109] compared to Poisson statistics, with $\mathrm{Var}(n) = \overline{n} + \overline{n}^2$). As a result, $\mathrm{Var}(n_1 - n_2)$ will be very large for data sets with $\overline{n}_1 \neq \overline{n}_2$. A second problem that hampers tests for twin-mode intensity squeezing is a delay between the detection of correlated pairs n_1 and and n_2 (Fig. 2.4(c)). Subtraction of measured values n_1 and n_2 without compensation for this delay will also lead to increased values for $\mathrm{Var}(n_1 - n_2)$.

The question that we address in the next section is how tests for twin-mode in-

tensity squeezing can be performed in experiments with significant unbalanced losses and delays between the Stokes and anti-Stokes fields. For a discussion of the requirements on detection systems for such measurements, see Appendix A.4; for a detailed description of the photodetectors used in these detection systems, see Appendix A.2.

Tests for twin-mode squeezing with unbalanced losses and delays

Fig. 2.4(c) illustrates that the residual signal $(n_1 - n_2)$ is strongly reduced by multiplying the retrieved anti-Stokes data set by a relative compensation factor A_r. Accordingly, the variance of $\mathrm{Var}(n_1 - A_r n_2)$ is reduced as well. This compensation can be carried out without adding noise, because it can be implemented as a simple multiplication of photon-count results after the results have been recorded. Alternatively, the measured values of n_1 and n_2 can be made equal by inserting additional losses into the stronger mode before detection. However, such optical attenuation will introduce additional noise. When implementing such strategies for reducing $\mathrm{Var}(n_1 - n_2)$, one needs to reexamine the definition and meaning of twin-mode intensity squeezing in Eq. (2.3). This will be analyzed below.

For this analysis we assume the simple model shown in the inset of Fig. 2.7. Two sources S_1 and S_2 send out states with well-defined photon numbers n_1 and n_2. The values for n_1 and n_2 fluctuate, but are perfectly correlated in pairs with $n_1 = n_2$. However, the emission from S_1 is delayed by Δt, with $(\Delta t)^{-1}$ larger than the emission repetition rate. The photon number in the emitted modes are detected at this repetition rate with photon counters D_1 and D_2. Losses in the channels between the sources and detectors are modeled with beam splitters with transmission T_1 and

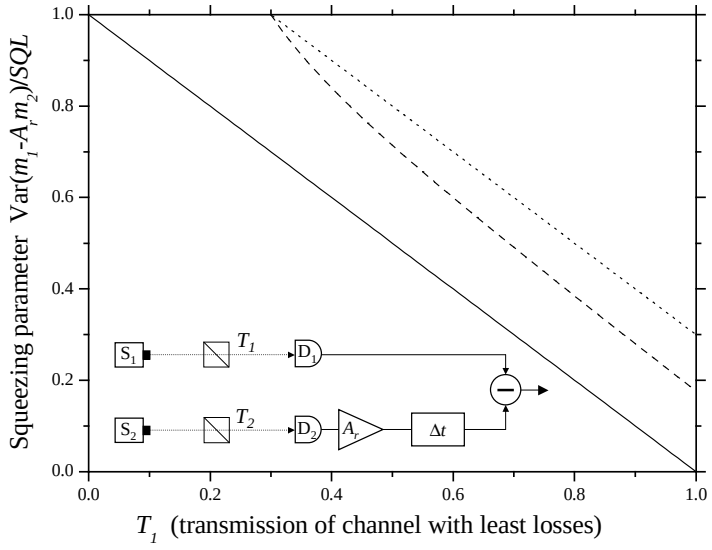

Figure 2.7: Modeling twin-mode intensity squeezing in the presence of unbalanced losses and delays. **(Inset)** Model used for investigating twin-mode intensity squeezing in the presence of unbalanced losses and delays (see text for details). **(Main graph)** Twin-mode intensity squeezing parameter $SQP = \mathrm{Var}(m_1 - A_r m_2)/SQL$, with $SQL = \overline{m}_1 + A_r^2 \overline{m}_2$, for the two modes detected in the model of the inset. The solid line is for $T_2 = T_1$ and $A_r = 1$. The dotted line is for $T_2 = T_1 - 0.3$, and compensating the difference between T_1 and $A_r T_2$ by inserting additional losses into channel 1 and keeping $A_r = 1$ (i.e., $T_1' = T_2$). The dashed line is for $T_2 = T_1 - 0.3$, and compensating the difference between T_1 and $A_r T_2$ with a noise-free amplification factor $A_r = T_1/T_2$.

T_2, and we assume $T_1 \geqq T_2$. Due to the losses, the measured photon numbers will be smaller than what is emitted, and the photon-count results will be denoted as m_1 and m_2. The detectors are assumed to be perfect (no dark counts, and imperfect detection efficiencies are included in T_1 and T_2). The detectors report photon number per event. Before subtraction and comparison to Eq. (2.3), the count results in channel 2 can be multiplied by a noise-free relative amplification factor A_r, and delayed by Δt.

When the paired fluctuations in n_1 and n_2 are large and $T_1 \neq T_2$, the variance in the subtracted signal $\mathrm{Var}(m_1 - m_2)$ will be large as well. In this case, the value

$\mathrm{Var}(m_1 - m_2)$ is not representative for the fundamental correlations between the signals, but a trivial artifact of the unequal losses in the two channels. As mentioned before, this can be dealt with by inserting additional losses into channel 1 to give $T_1' = T_2$ or by amplifying the results of channel 2 with $A_r = T_1/T_2 = \overline{m}_1/\overline{m}_2$. More generally, one needs to realize $T_1 = A_r T_2$. This suggests that one can replace the condition for twin-mode intensity squeezing (Eq. (2.3)) with

$$\mathrm{Var}(m_1 - A_r m_2) < \overline{m}_1 + A_r^2 \overline{m}_2 \,, \tag{2.4}$$

assuming that one has set

$$A_r = \overline{m}_1/\overline{m}_2 \,, \tag{2.5}$$

since the standard quantum limit in this case is given by

$$\mathrm{Var}(m_1) = \overline{m}_1 \,, \tag{2.6}$$

and

$$\mathrm{Var}(A_r m_2) = A_r^2 \,\mathrm{Var}(m_2) = A_r^2 \,\overline{m}_2 \,. \tag{2.7}$$

The right hand side of Eq. (2.4) is the adjusted level for the standard quantum limit, $SQL = \overline{m}_1 + A_r^2 \overline{m}_2$. The factor A_r^2 needs to be introduced because (2.4) compares the fluctuations of a mode to the fluctuations of a coherent state, and these are amplified in our model as well. Below we analyze four cases where this new definition for squeezing is used (see also Fig. 2.7). We will calculate the squeezing parameter SQP, defined as

$$SQP = \frac{\mathrm{Var}(m_1 - A_r m_2)}{\overline{m}_1 + A_r^2 \overline{m}_2} = \frac{\mathrm{Var}(m_1 - A_r m_2)}{SQL} \,, \tag{2.8}$$

which is smaller than 1 in case of twin-mode squeezing, and equal to 0 for perfect twin-mode squeezing.

(i) $T_1 = T_2$ *and* $A_r = 1$: The beam splitters, with equal transmission, randomly remove photons from the modes, and this process gives partition noise in m_i, with, for fixed n_i, a binomial variance $\mathrm{Var}(m_i) = n_i T_i(1-T_i)$, $i = 1, 2$, see Refs. [124, 109]. This leads to the familiar result $SQP = (n_1T_1(1-T_1)+n_2T_2(1-T_2))/(n_1T_1+n_2T_2) = 1-T_1$. Squeezing can still be observed, but the value for SQP approaches 1 for significant losses. See the solid line in Fig. 2.7.

(ii) $T_1 > T_2$, *which is compensated by inserting additional losses into channel 1 to give* $T_1' = T_2$, $A_r = 1$: The analysis goes as for the previous case, but now the result is $SQP = 1-T_2$. The squeezing parameter is set by the channel with the most losses. See the dotted line in Fig. 2.7.

(iii) $T_1 > T_2$ *and* $A_r = T_1/T_2 = \overline{m}_1/\overline{m}_2$: Working it out as for case (i) gives $SQP = (1 - T_1 + (T_1/T_2)(1 - T_2))/(1 + T_1/T_2)$. As compared to case (ii) there is an improvement in the observable minimum SQP. See the dashed line in Fig. 2.7.

(iv) $T_1 > T_2$ *and* $A_r = T_1/T_2 = \overline{m}_1/\overline{m}_2$, *but the sources* S_1 *and* S_2 *send out classical pulses of light instead of Fock states*: For comparison, we analyze SQP for the parameters of (iii) for the situation where the sources S_1 and S_2 send out classical pulses of light (coherent states, with uncorrelated quantum fluctuations) with photon-number expectation values $\overline{n}_1 = \overline{n}_2$. We consider the simplest case where $\overline{n}_1$ and $\overline{n}_2$ are constant in time. When a coherent state is attenuated its photon statistics remain Poissonian [124, 109]. This gives $\overline{m}_i = T_i\overline{n}_i$ with $\mathrm{Var}(m_i) = \overline{m}_i$, and yields $SQP = 1$. This shows that $SQP < 1$ cannot be realized with very stable classical fields.

The above analysis shows that Eqs. (2.4)-(2.8) provide a valid test for twin-mode intensity squeezing useful in many realistic experimental situations. Squeezing is

identified by values $SQP < 1$, and this cannot be realized with two classical fields (coherent states) with uncorrelated fluctuations. However, as usual, observation of significant squeezing (say $SQP < 0.5$, i.e., more than 3 dB squeezing) requires both $T_1 > 0.5$ and $T_2 > 0.5$.

The method used in the experiments described in Section 2.3.2 corresponds to case (iii) above. We digitally record the signals m_1 and m_2, then compensate for the loss and delay by multiply the data m_2 by the factor $A_r = T_1/T_2 = \overline{m}_1/\overline{m}_2$, and advancing or delaying signal m_2 by the appropriate delay.

2.3.2 Nonclassical Correlations in the Continuous-Wave Regime

We now turn to investigating the degree of correlations between the Stokes and anti-Stokes beams in the cw regime. To this end we obtained Raman signals with cw control beams, recorded signal intensities with high resolution, and analyzed the spectral densities of the Stokes and anti-Stokes signal fluctuations using the discrete Fourier transform [21]. The fluctuation spectra of the Stokes and anti-Stokes fields are peaked at low frequencies, with the large noise reflecting the super-Poissonian nature of single-mode spontaneous Raman excitations (Fig. 2.8(a)). The spectral half-width of this spontaneous noise could be tuned in the range from 100 kHz to 1 MHz (with tails up to about 2 MHz), by varying the write and retrieve beam intensities and the write beam detuning. At higher frequencies, larger than any physical process in the atomic medium, the measured spectra generally approach a flat noise floor. Correlations between the two fields result in a large noise reduction in the spectrum of the signal that is formed by subtracting the Stokes and anti-Stokes signals in

the time domain, and then taking the discrete Fourier transform. In this difference intensity analysis it was essential to compensate for the unbalanced intensities and the delay between the Stokes and anti-Stokes beams.

In the case that the optical fields have losses before detection, the level of twin-mode squeezing that can be observed is reduced (see Section 2.3.1 and Ref. [6]). For our data, the anti-Stokes signal appears identical to the Stokes signal except for an apparent attenuation by a factor of ≈ 5 and a time shift (Fig. 2.4(c)). In this case, twin-mode squeezing can still be investigated when the time shift is compensated and when the unbalanced attenuation is compensated by unbalanced linear amplification of the two signals. We have developed a method using fast, high-accuracy sampling of the Raman signals followed by software compensation of the time shift and linear amplification. In this procedure the re-scaling of photon shot noise and detector dark noise levels are accounted for accordingly. The resulting signals are subtracted for calculation of the spectrum in Fig. 2.8. The details of this procedure are described in Section 2.3.1.

Fig. 2.8(a) shows the fluctuation spectral density of the anti-Stokes field (blue) and of the signal formed by subtraction of the Stokes and anti-Stokes signal in the time domain (green). The spectrum of the Stokes fluctuations is not shown, but is nominally identical to that of the anti-Stokes signal. The super-Poissonian character of the Raman signals leads to strong fluctuations at low frequencies (within the Raman bandwidth). At high frequencies (outside the Raman bandwidth) the fluctuation spectrum is flat and set by the shot-noise level for photon detection, and agrees with the independently determined level for the photon shot noise (PSN). The PSN

represents an experimental measurement of the SQL defined in the previous section. At frequencies near the high end of the Raman bandwidth (around 1.6 MHz, see the inset), the fluctuations in the subtracted signal fall bellow the measured PSN (gray curve in the inset).

We routinely observed 30 dB of intensity correlations over a broad range of low frequencies. The degree of subtraction is limited by the precision of the electronic components used in our detection system (see Appendix A.2). Although this level of subtraction was not sufficient to eliminate spontaneous noise entirely at low frequencies, this was readily achieved in the higher frequency range where fluctuations in the Raman fields were smaller. Whereas at large frequencies the difference intensity noise approaches a flat noise floor, at intermediate values, near the high end of the Raman bandwidth, the difference intensity noise consistently drops a few percent below that level.

To quantify the degree of correlations in this intermediate regime, we performed several experimental tests. The benchmark level representing nonclassical effects is set by the photonic shot noise (PSN) associated with the Poissonian photon-number statistics of coherent classical light, and it corresponds to a flat fluctuation spectrum.

As described in the previous section, the criterion for two modes of light to be photon-number squeezed is that for a sequence of photon-number measurements n_1 and n_2 the variance in $(n_1 - n_2)$ is less than the sum of the averages $(\overline{n}_1 + \overline{n}_2)$ [6]. For measurements on two continuous photon flux signals, analyzed in the frequency domain, this corresponds to the fluctuation spectrum of the time-domain difference signal being less than such a fluctuation spectrum from two classical fields with the

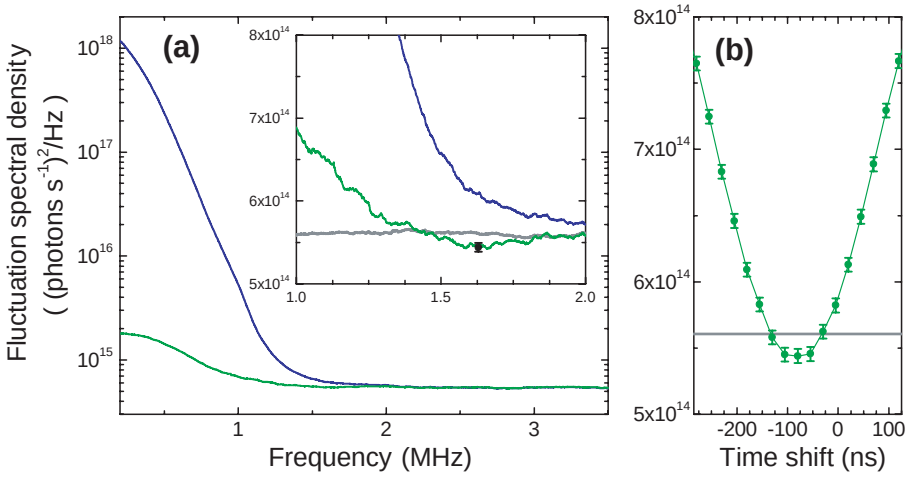

Figure 2.8: Twin-mode intensity squeezing in the continuous-wave regime. **(a)** The fluctuation spectral density of the anti-Stokes field (blue) and of the signal formed by subtraction of the Stokes and anti-Stokes signals in the time domain (green). The data point at 1.6 MHz shows a ± 1 standard deviation error bar. The data is the result of averaging over 23 data sets, each of 2 ms duration and 10% retrieval efficiency, taken with identical control parameters over the course of one hour. The spectra have an averaging bandwidth of 200 kHz. **(b)** The fluctuation spectral density levels at 1.6 MHz (green) for the green line in (a), for different values of the time-shift between Stokes and anti-Stokes signal before subtraction subtraction. The level at 1.6 MHz only drops below the measured PSN level (gray line) for time-shifts around 81 ns, in agreement with the observed delay between the Stokes and anti-Stokes signal for this data set.

same average photon flux and classical intensity correlations, such as obtained by splitting a single light beam on a perfect 50-50 beam splitter.

We performed several checks to define the PSN level. The difference signal for two output beams from a single laser beam on a beam splitter possessed a flat fluctuation spectrum at a level that was linearly (rather than quadratically) dependent on beam intensity, characteristic for PSN. Fig. A.6 in Appendix A.2 shows this for the frequency range of 200 kHz - 300 kHz; similar results were obtained for the entire bandwidth of the detector. The measured level of the fluctuation spectrum is

in excellent agreement with PSN values calculated using the shot-noise formula and independently determined detector and amplifier parameters taking into account an offset from the detector dark-noise levels; the data in Fig. 2.8 represents noise with contributions from both detected fields and detector dark noise. The observed onset of nonclassical correlations is limited by the finite retrieval efficiency, the dark-noise levels of the detectors, and the similarity of the gain versus frequency behavior of the detectors.

In addition to this PSN calibration, we performed a control experiment by measuring the difference signal between two beams formed by splitting the Stokes field on a beam splitter. In this measurement, the average intensity in each detection channel was carefully adjusted to match the Stokes and anti-Stokes channels in the correlation measurement of Fig. 2.8. This control experiment yielded a flat noise spectrum in agreement with the PSN level (gray line in the inset of Fig. 2.8(a)) and, unlike the green line in Fig. 2.8(a), did not show the reduced noise level around 1.6 MHz. This confirms that the Stokes/anti-Stokes difference spectrum in Fig. 2.8(a) (green) drops at intermediate-frequencies about 4% below the PSN level. Finally, Fig. 2.8(b) shows that the degree of correlations depends sensitively upon the delay compensation between the Stokes and anti-Stokes signals: the onset of nonclassical correlations appears only when one properly compensates for the time that the atoms spend in a spin-flipped state. This sensitivity to delay compensation represents evidence for the storage of nonclassical states in atomic ensembles.

Several factors limit the degree of the observed quantum correlations. One of the most significant limitations is associated with the incomplete retrieval process. The

retrieval efficiency (10%-30%), limited in our experiments by imperfect spatial mode matching and the available laser power, did not allow for large quantum correlations to be observed in the presence of uncorrelated noise. In principle, the observed bandwidth of the nonclassical correlations could be greatly improved by working at lower light levels, since the relative magnitude of the super-Poissonian noise would then be lower.

2.4 Conclusions

The experiments described in this chapter demonstrate the generation and temporary storage of spin-wave states in an atomic ensemble, and retrieval of these states by mapping onto correlated nonclassical states of light. We have probed the correlations between photonic and atomic states by measuring the correlations between the separate photon fields produced in the generation and retrieval of the atomic state. Strong correlations in the relative intensity of these two photon fields were observed in both the pulsed and cw regimes in the time domain. In the cw regime, large excess noise at low frequencies prevented the observation of nonclassical correlations in the time domain, but by analyzing the correlations in the frequency domain, nonclassical correlations were observed in the frequency range of $\sim 1 - 2\,\mathrm{MHz}$. At the time, this was the first observation of nonclassical correlations in such a system, and represented a first step towards implementation of the DLCZ long-distance quantum communication proposal.

Chapter 3

Shaping Quantum Pulses of Light using Atomic Ensembles

3.1 Introduction

The existence of nonclassically correlated photon pairs demonstrated in the previous chapter implies the ability to create nonclassical states of the radiation field by performing conditional detection on one of the fields of this correlated pair. In recent years much effort has been directed toward generating quantum-mechanical states of the electromagnetic field with a well-defined number of quanta (i.e., photon-number or Fock states). Motivated in part by the ideas of quantum information science, tremendous progress has been made in generating single-photon states by using photon pairs in parametric down-converters [61], single emitters [99, 110], and single atoms in high-finesse cavities [74, 97]. While parametric down-conversion techniques have recently been used to generate multi-photon states [123], it remains experimentally challenging

to implement schemes that allow for simultaneous control over both photon number and spatio-temporal properties of the pulse. Control over the spatio-temporal properties of a pulse may prove useful in experiments where the indistinguishability of single photons is a requirement, such as linear-optics quantum computation [72].

In this chapter, we describe proof-of-principle experiments demonstrating a novel approach for generating pulses of light with controllable, well-defined photon numbers, propagation direction, timing, and pulse shapes. These experiments exploit long-lived coherent memory for photon states in an optically dense atomic medium [83], and combine aspects of earlier studies on "light storage" [79, 103] and the Raman-scattering based preparation and retrieval of atomic excitations [34, 118, 76, 30, 64, 104] discussed in Chapter 2. These experiments expand previous studies of EIT-based control of light propagation [54, 79, 103, 16] into the domain of few-photon nonclassical light pulses.

3.2 Few-Photon Pulse Shaping

As was the case for the experiments described in Chapter 2, the experiments in this chapter utilize an ensemble of ^{87}Rb atoms inside magnetic shielding, allowing us to approximate the full rubidium level structure shown in Fig. A.1 with a three-level "Λ-type" atomic configuration as shown in Fig. 3.1(a). In our approach we first optically pump a large ensemble of N atoms to the ground state $|g\rangle = |5^2S_{1/2}, F = 1\rangle$. Spontaneous Raman scattering [106] is induced by a weak, off-resonant laser beam with Rabi frequency Ω_W and detuning Δ_W, referred to as the write laser. This two-photon process flips an atomic "spin" into the metastable state $|s\rangle$ while producing

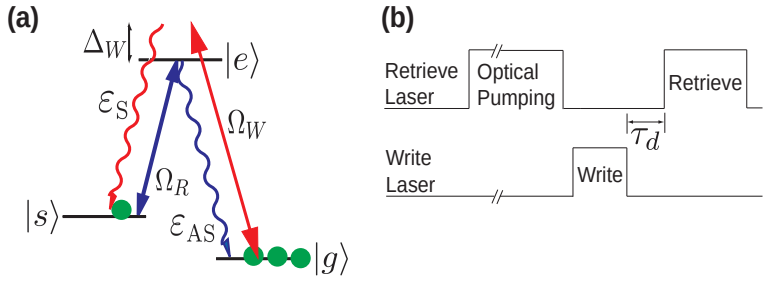

Figure 3.1: Experimental procedure. **(a)** ^{87}Rb levels used in the experiments (D_1 line): $|g\rangle = |5^2S_{1/2}, F = 1\rangle$, $|s\rangle = |5^2S_{1/2}, F = 2\rangle$, and $|e\rangle$ corresponds to $|5^2P_{1/2}, F' = 1\rangle$ and $|5^2P_{1/2}, F' = 2\rangle$. The write (retrieve) laser and Stokes (anti-Stokes) beam are illustrated in red (blue). The write (retrieve) laser has a diameter of 200 μm (2 mm) at the center of the atomic ensemble. $\Delta_W \approx 1$GHz. **(b)** After the optical pumping pulse (provided by the retrieve laser), the 1.6 μs-long write pulse is followed by the retrieve pulse after a controllable delay τ_d.

a correlated frequency-shifted Stokes photon. Energy and momentum conservation ensure that for each Stokes photon emitted in certain direction there exists exactly one flipped spin quantum in a well-defined spin-wave mode. The number of spin wave quanta and the number of photons in the Stokes field thus exhibit strong correlations, and as a result, measurement of the Stokes photon number n_S ideally projects the spin-wave onto a nonclassical collective state with n_S spin quanta [34]. After a controllable delay time τ_d (see Fig. 3.1(b)), the stored spin-wave can be coherently converted into a light pulse by applying a second near-resonant laser beam with Rabi frequency Ω_R (retrieve laser), see Fig. 3.1(a). As discussed in previous chapters, the retrieval process utilizes EIT [54, 113, 87, 14, 42]. The direction, delay time τ_d, and rate of retrieval are determined by the direction, timing, and intensity of the retrieve laser, allowing control over the spatio-temporal properties of the retrieved anti-Stokes pulse. Since the storage and retrieval processes ideally result in identical photon numbers in the Stokes and anti-Stokes pulses [87], this technique should allow preparation of

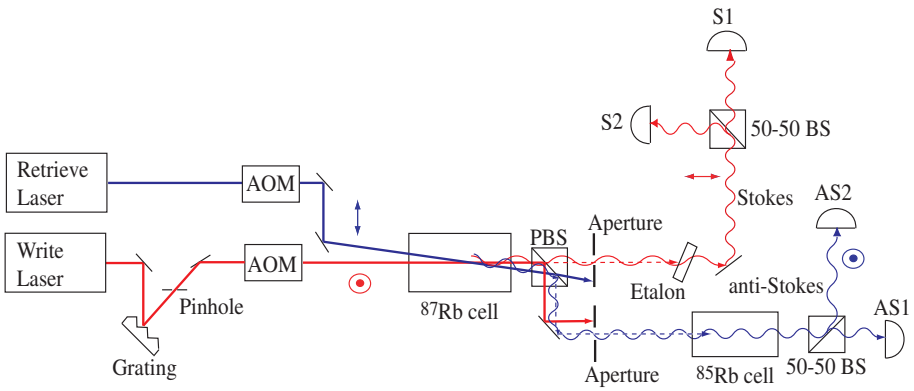

Figure 3.2: Schematic of the experimental setup. The write and retrieve lasers overlap at a small angle ($\sim$ 10 mrad) inside a magnetically-shielded ^{87}Rb vapor cell held at $\approx$ 75^{o}C with 6 Torr of Ne buffer gas. AOM is acousto-optical modulator. Arrows and circles give the polarization of the write and retrieve lasers and the Stokes and anti-Stokes fields. PBS is a polarizing beamsplitter (beam-splitting Glan-Thompson crystal polarizer). S1,S2 (AS1,AS2) are avalanche photodetectors (APDs) for the Stokes (anti-Stokes) channel (Perkin-Elmer model SPCM-AQR-16-FC, with a dark count rate of less than 25 s^{-1}).

an n-photon Fock state in the anti-Stokes pulse conditioned on detection of n Stokes photons.

The experimental apparatus (see Figs. 3.2 and 3.3) is similar to that described in Chapter 2. The primary difference between these experiments and the experiments described in Chapter 2 is that the experiments in this chapter investigate few photon pulses, whereas the experiments described in Chapter 2 involved pulses with $\sim 10^3$ to 10^7 photons per pulse. As a result, the experiments of Chapter 2 utilized photodetectors with PIN (positive-intrinsic-negative) photodiodes [59] for photon detection (see Appendix A.2), while those described in this chapter use avalanche photodetectors (APDs).

The primary experimental challenge lies in transmitting the few-photon Stokes and anti-Stokes pulses while simultaneously blocking the write and retrieve laser beams.

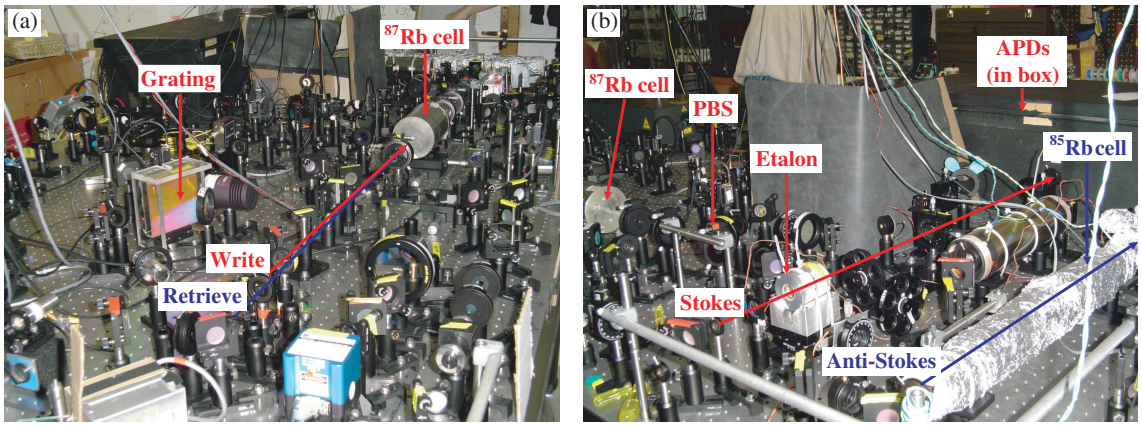

Figure 3.3: Photograph of the experimental setup. **(a)** The ^{87}Rb ensemble (inside three layers of magnetic shielding), and the paths for the write and retrieve lasers, are marked. As described in Section 2.2.1, the grating is used to filter the spontaneous emission noise from the write laser diode. **(b)** Polarizing beamsplitter (PBS) used for polarization filtering. Etalon used for frequency filtering of the write laser from the Stokes field, and the ^{85}Rb ensemble used for frequency filtering of the retrieve laser from the anti-Stokes field.

As described in Chapter 2, this is accomplished by a combination of polarization and frequency filtering. As shown in Fig. 3.2, the write and retrieve laser polarization are in a Lin $\perp$ Lin configuration, with both of the fields being linearly polarized but in orthogonal directions. In this case, we observe that the scattered Stokes (anti-Stokes) photons that are emitted are primarily polarized orthogonally to the write (retrieve) laser polarization. Therefore, by placing a polarizing beamsplitter after the ^{87}Rb cell as shown in Fig. 3.2, the Stokes (anti-Stokes) and write (retrieve) fields can be separated to 5 parts in 10^6 (measured value), limited by the quality of the beamsplitter. As discussed in Chapter 2, the physics underlying the orthogonal polarizations of the Stokes (anti-Stokes) compared to the write (retrieve) has been explored theoretically. It is seen to result from a destructive interference for the production of Stokes (anti-Stokes) photons with the same polarization as the write

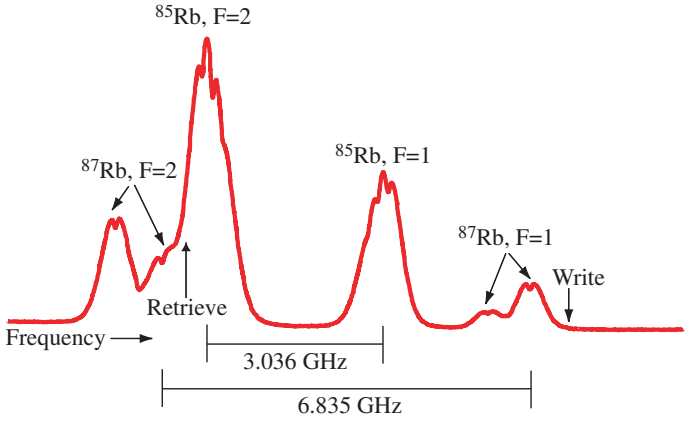

Figure 3.4: Write and retrieve laser frequencies, relative to the fluorescence spectrum of the D_1 line ($5^2S_{1/2} \rightarrow 5^2P_{1/2}$) of rubidium. Rubidium vapor is at room temperature and thus the transitions are Doppler-broadened. The write laser is detuned 1 GHz above the $F = 1 \rightarrow F' = 2$ transition; Stokes photon frequency is 6.835 GHz smaller than that of the write laser. In order to filter out the retrieve laser via ^{85}Rb absorption, the retrieve laser is detuned 400 MHz above the $F = 2 \rightarrow F' = 2$ transition; the anti-Stokes photon frequency is 6.835 GHz larger than that of the retrieve laser, and is therefore off-resonance with ^{85}Rb .

(retrieve) lasers [60].

Further filtering is provided by an etalon or an optically-pumped ^{87}Rb cell in the write channel, and a ^{85}Rb cell in the retrieve channel; this combined filtering separates the write (retrieve) laser from the Stokes (anti-Stokes) Raman light to a few parts in 10^9 (10^{12}). The principle behind using ^{85}Rb to filter the retrieve laser from the anti-Stokes field is shown in Fig. 3.4. By detuning the retrieve laser slightly from resonance with the $F = 2 \rightarrow F' = 2$ transition of ^{87}Rb , the retrieve laser frequency is on resonance with ^{85}Rb , and thus will be absorbed by the ^{85}Rb ensemble; the anti-Stokes field, which is 6.835 GHz higher in frequency than the retrieve laser, is then far-off resonant with ^{85}Rb (the ^{85}Rb ground-state hyperfine splitting is just 3.036

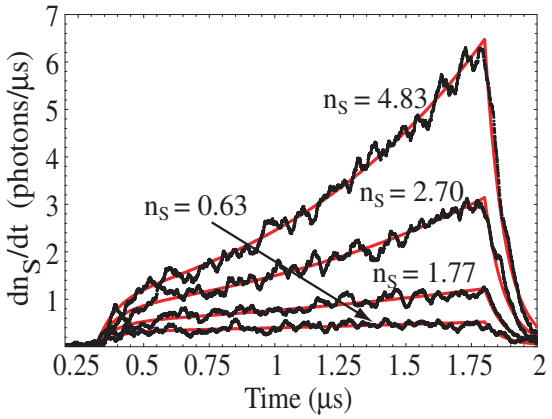

Figure 3.5: Stokes pulse shapes. Experimentally measured (black) and theoretically calculated (red) values of the Stokes photon flux dn_S/dt. For each plot, $n_S = \int dt\, dn_S/dt$ represents the total number of photons emitted from the cell. Write laser power was varied from 25 μW to 100 μW.

GHz [119]), and therefore propagates through the ^{85}Rb ensemble unabsorbed.

Experimentally, we take advantage of the long coherence time of the atomic memory ($\sim 3\,\mu$s in the present experiment, see Fig. 3.8) to create few-photon pulses with long coherence lengths ($\sim$ few μs) that significantly exceed the dead-time of the APDs (~ 50 ns). This allows us to directly count the photon number in each of the pulses and to directly measure the pulse shapes by averaging the time-resolved APD output over many experimental runs. Connected to each APD is a multi-mode fiber, meaning we detect more than one transverse spatial mode.

Fig. 3.5 shows the average number of detected Stokes photons per unit time (photon flux) in the write channel as a function of time during the 1.6 μs-long write pulse. The magnitude of the photon flux is controlled by varying the excitation intensity of the write laser. The shape of the Stokes pulse in time changes qualitatively as the total number of photons in the pulse exceeds unity: for pulses containing on average

one photon or less, the flux is constant in time, whereas for pulses containing more than one photon, the flux increases with time.

The observed evolution of the Stokes pulses can be understood qualitatively by considering the mutual growth of the photon field and spin excitation: the first flipped spin *stimulates* subsequent spin excitations which are accompanied by increased probability of Stokes photon emission [3]. This process is governed by the collective Raman scattering rate $\xi = \eta|\Omega_W|^2\gamma/\Delta_W^2$, which is equal to the product of the optical depth η and the single atom scattering rate $|\Omega_W|^2\gamma/\Delta_W^2$, where γ is the decay rate of $|e\rangle$. For short excitation times t, we consider the evolution of several Hermite-Gaussian modes of Stokes radiation [106], and find that the photon flux is given by $dn_s/dt = \bar{N}\xi(1+\xi t+...)$, where $\bar{N}$ is the effective number of transverse modes (from experimental measurements we infer $\bar{N} \sim 4$) [3]. This prediction for dn_s/dt agrees with our observation that the flux will increase with time for $n_s \sim \xi t \geq 1$. The transition from a spontaneous to stimulated nature of the Stokes process also affects the spatial distribution of the atomic spin wave. For $n_s \leq 1$ the excitation is calculated to be uniformly distributed in the cell, while for $n_s > 1$ the spin-wave amplitude grows toward the end of the cell (see inset to Fig. 3.6(b)). The observed dynamics provide evidence for the collective nature of the atomic spin excitations.

After a time delay τ_d, we apply the retrieve beam to convert the stored spin wave into anti-Stokes photons. Fig. 3.6 demonstrates that the duration and peak flux of the anti-Stokes pulse can be controlled via the intensity of the retrieve laser. The resonant retrieve laser converts the spin coherence into a dark-state polariton, and eventually into an anti-Stokes photon. Note that the retrieve laser establishes an

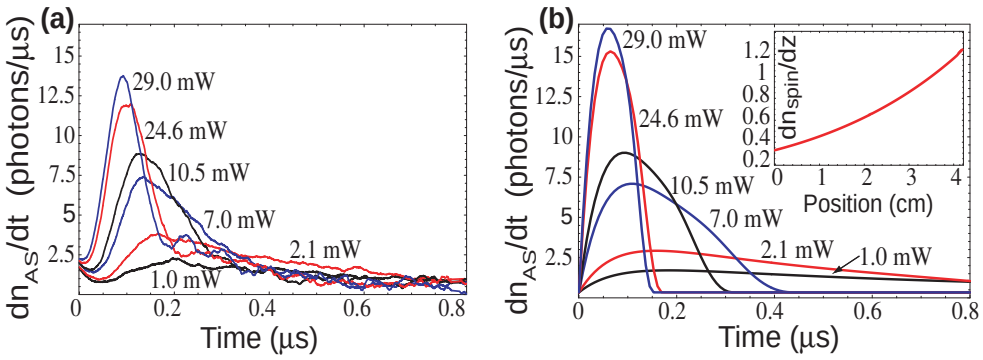

Figure 3.6: Anti-Stokes pulse shapes. **(a)** Experimentally measured, and **(b)** theoretically calculated values of the anti-Stokes photon flux dn_{AS}/dt. The experimental pulse shapes correspond to a Stokes pulse with $n_S \approx 3$ photons, and the theoretical curves assume an initial spin wave with $n_{spin} = 3$ excitations and an optical depth of $\simeq 20$. Each curve is labeled with the power of the retrieve laser. **(b, inset)** Theoretical calculation of the number of flipped spins per unit length dn_{spin}/dz (cm^{-1}) for $n_{spin} = 3$.

EIT configuration for the generated anti-Stokes field, so that the anti-Stokes light propagates unabsorbed through the cell. In the ideal limit of perfect EIT and large optical depth, the temporal shape of the anti-Stokes pulse is equivalent to the spatial shape of the atomic spin coherence, delayed by the time required to propagate out of the atomic cell at the group velocity $v_g(t) \propto |\Omega_R(t)|^2$ [42]. For larger (smaller) retrieve laser intensity, the excitation is released faster (slower), while the amplitude changes in such a way that the total number of anti-Stokes photons is always equal to the number of spin-wave excitations. In practice, decay of the spin coherence during the delay time τ_d and finite optical depth flatten and broaden the anti-Stokes pulse, reducing the total number of anti-Stokes photons which can be retrieved within the coherence time of the atomic memory, as indicated by theoretical calculations [3] (Fig. 3.6) based on Ref. [42]. The detailed comparison between theory and experiment in

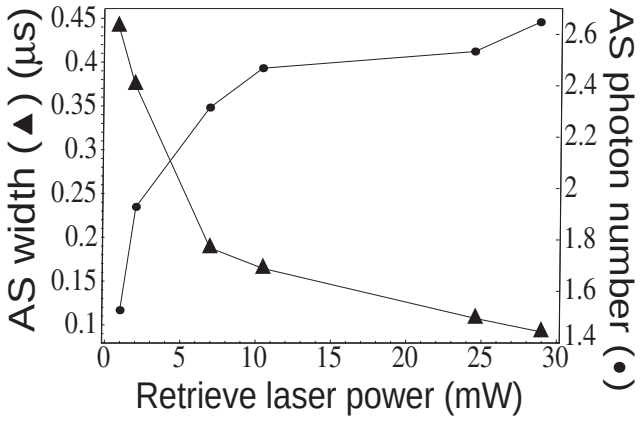

Figure 3.7: Measured anti-Stokes pulse width (full-width at half-max) and total photon number as a function the retrieve laser power. Lines are to guide the eye.

Figs. 3.5 and 3.6 suggests that the bandwidth of the generated anti-Stokes pulse is close to being Fourier-transform limited, while the transverse profile effectively corresponds to only a few spatial modes.

Figure 3.7 shows a plot of the full-width at half-max and total photon number for the retrieved anti-Stokes pulses shown in Fig. 3.6. Since the retrieve laser acts as an EIT control laser for the anti-Stokes field, as the strength of the retrieve laser is decreased, the group velocity should decrease (see Eq. (1.6)), corresponding to an increase in the time duration of the pulse. This is in agreement with the data shown in Fig. 3.7, which shows the width in time of the retrieved pulse increases as the intensity of the retrieve laser is decreased. In addition, as the strength of the retrieve laser is decreased, the photon-to-atom ratio of the polariton propagating through the atomic medium should also decrease (see Eqs. (1.9) and (1.10)). Since the total number of photons retrieved depends not on the retrieve laser, but on the amplitude of the initial atomic coherence, the changes in group velocity and photon-to-atom

ratio should compensate each other so that the total number of retrieved photons is the same regardless of the retrieve laser intensity. Under ideal conditions, where the $|g\rangle - |s\rangle$ atomic coherence does not decay, this would indeed be the case. However, we see from Fig. 3.7 that the decay of the $|g\rangle - |s\rangle$ coherence (characteristic time $\sim 3\,\mu$s, see Fig. 3.8) does result in a decreased number of retrieved photons as the width of the retrieved pulse increases.

3.3 Quantum-Correlated Photon States

As demonstrated in Chapter 2, at fixed laser intensities and durations, the number of Stokes and anti-Stokes photons fluctuates from event to event in a highly correlated manner [118]. In order to quantify these correlations in the present experiment, we directly compare the number of Stokes and anti-Stokes photons for a large number of pulsed events (each with identical delay times τ_d and laser parameters). The variance of the resulting distributions is then compared to the photon shot noise level $\mathrm{PSN}_{th} = \bar{n}_S + \bar{n}_{AS}$, which represents the maximum degree of correlations possible for classical states [91]. We experimentally determine the photon shot noise for each channel by using a 50-50 beamsplitter and two APDs per detection channel (see Fig. 3.2) which allows us to accurately determine the measured $\mathrm{PSN}_{meas} = \mathrm{Var}(n_{AS1} - n_{AS2}) + \mathrm{Var}(n_{S1} - n_{S2})$ value for each experiment. To quantify the correlations, we consider the normalized variance $\mathrm{V} = \mathrm{Var}(\{n_{AS} - n_S\})/\mathrm{PSN}_{meas}$, which is one for classically correlated pulses and zero for pulses exhibiting perfect number correlations. Using this method, we measure $V = 0.942 \pm 0.006$ for the data shown in Fig. 3.8 at delay time $\tau_d = 0$. For the experimental conditions of Fig. 3.8, we estimate that

dead-time effects reduce the measured $\bar{n}_{AS}$ by 2.5% from its actual value and increase $\mathrm{V} = \mathrm{Var}(\{n_{AS} - n_S\})/\mathrm{PSN}_{meas}$ by less than 0.2% from its actual value (well within the $\sim 0.6\%$ error bars).

Fig. 3.8 shows the normalized variance V as a function of storage time τ_d. Non-classical correlations ($V < 1$) between Stokes and anti-Stokes pulses are clearly observed for storage times up to a few microseconds. The time scale over which the correlations decay is determined by the coherence properties of the atomic spin-wave: nonclassical correlations are obtained only as long as the coherence of the stored excitation is preserved. Fig. 3.8 also shows that the retrieval efficiency (the ratio of the average number of anti-Stokes photons to the average number of Stokes photons) decreases in a similar manner as τ_d is increased. A fit to this time dependence (dashed line) yields a 1/e characteristic decoherence time $1/\gamma_c$ of about 3 μs, consistent with the timescale for atomic diffusion from the detection-mode volume (see Appendix A.1 for details). These results demonstrate that within the atomic coherence decay time, it is possible to control the timing between preparation and retrieval, while preserving nonclassical correlations.

It is important to note that at $\tau_d = 0$ the observed value $V = 0.942 \pm 0.006$ is far from the ideal value of $V = 0$. One source of error is the finite retrieval efficiency, which is limited by two factors. Due to the atomic memory decoherence rate γ_c, the finite retrieval time τ_r always results in a finite loss probability $p \approx \gamma_c \tau_r$. Moreover, even as $\gamma_c \to 0$ the retrieval efficiency is limited by the finite optical depth η of the ensemble, which yields an error scaling as $p \sim 1/\sqrt{\eta}$ [3]. The anti-Stokes pulses in Fig. 3.8 have widths on the order of the measured decoherence time, so the

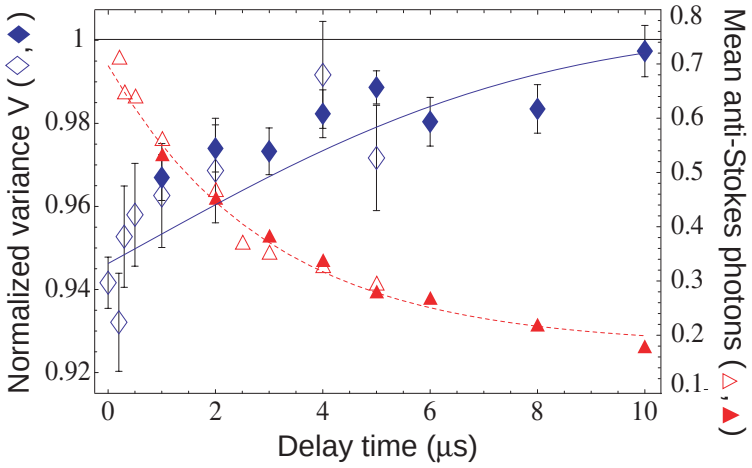

Figure 3.8: Observation of nonclassical correlations. Normalized variance V (blue diamonds) and mean number of anti-Stokes photons (red triangles) versus delay time τ_d. The open and closed symbols represent two experimental runs with similar experimental parameters. The dashed line is an exponential fit (characteristic time $\sim 3\,\mu$s) to the mean number of anti-Stokes photons. The solid line is the result of a theoretical model described in the text.

atomic excitation decays before it is fully retrieved. The measured maximum retrieval efficiency at $\tau_d = 0$ corresponds to about 0.3.

In addition to finite retrieval efficiency, other factors reduce correlations, including losses in the detection system, background photons, APD afterpulsing effects, and imperfect mode matching. To understand the effects of such imperfections, we created a theoretical model which incorporates loss, background, and several spatial modes. Based on experimental measurements, the overall detection efficiency (α) and number of background photons (n_{BG}) used in the model are $\alpha_S = 0.07$, $n_S^{BG} = 0.3$ ($\alpha_{AS} = 0.21$, $n_{AS}^{BG} = 0.12$) on the Stokes (anti-Stokes) channel, with a retrieval efficiency decay time of $3\,\mu s$ and 4 transverse spatial modes assumed. The results of this model are represented by the solid line in Fig. 3.8, and agree quite well with experimental

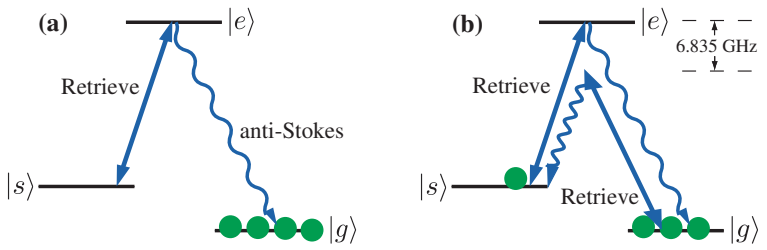

Figure 3.9: Signal and noise processes in EIT-based retrieval of atomic coherences. **(a)** Ideal picture of EIT-based retrieval. Retrieve laser on-resonance with the $|s\rangle \rightarrow |e\rangle$ transition coherently generates an anti-Stokes photon (the signal) at a frequency equal to the $|g\rangle - |e\rangle$ frequency difference. **(b)** Four-wave mixing process that produces noise photons uncorrelated with the stored atomic coherence. The process results because the retrieve laser couples not only the $|s\rangle \rightarrow |e\rangle$ transition, but also the $|g\rangle \rightarrow |e\rangle$ transition at a detuning of 6.835 GHz (the $|g\rangle - |s\rangle$ frequency difference.)

observation.

Losses arise from decoherence of the atomic memory, imperfect transmission through the filtering etalon (Stokes) and ^{85}Rb ensemble (anti-Stokes), and coupling into the detection fibers. Background is caused by imperfect filtering of the write and retrieve lasers, as well as a four-wave mixing process resulting from the undesired coupling of the $|g\rangle$ and $|e\rangle$ states by the retrieve laser.

Fig. 3.9 shows an atomic level structure demonstrating the origin of this four-wave mixing process. Fig. 3.9(a) shows an ideal picture of EIT-based retrieval. The retrieve laser is on-resonance with the $|s\rangle \rightarrow |e\rangle$ transition, and coherently generates an anti-Stokes photon at a frequency equal to the $|g\rangle - |e\rangle$ frequency difference. This retrieved anti-Stokes photon is the "signal" we wish to detect. In addition to these signal photons, however, are noise photons generated in a four-wave mixing process shown in Fig. 3.9(b). The process results because the retrieve laser couples not only the $|s\rangle \rightarrow |e\rangle$ transition, but also the $|g\rangle \rightarrow |e\rangle$ transition. This results in photons

generated at +6.835 GHz (anti-Stokes) and −6.835 GHz (Stokes) from the retrieve laser frequency. These photons are not correlated with stored atomic coherence, and therefore serve as noise background for our detection of the "signal" anti-Stokes photons shown in Fig. 3.9(a). While the retrieve laser is filtered by the ^{85}Rb ensemble (see Fig. 3.2), the Stokes and anti-Stokes noise photons are not on resonance with ^{85}Rb , and therefore are not absorbed by the ^{85}Rb ensemble.

3.4 Conclusions

The experiments described in this chapter utilized Raman scattering and EIT-based retrieval of atomic coherences in atomic ensembles to investigate the spatiotemporal and quantum statistical properties of correlated photon states produced in the generation and retrieval of few-excitation collective atomic coherences. By measuring the spatiotemporal properties of the Stokes photons emitted upon generation of the atomic coherence, we verified the collective nature of the atomic coherence. Using EIT-based retrieval of these atomic coherences, we demonstrated the ability to shape the temporal envelope of the retrieved anti-Stokes photon pulses. We studied the quantum statistical properties of this process by observing nonclassical photon-number correlations between the Stokes and anti-Stokes pulses.

Chapter 4

Conditional Generation of Single Photons using Atomic Ensembles

4.1 Introduction

In this chapter, we describe experiments that utilize the nonclassical correlations demonstrated in the previous chapter to generate single-photon anti-Stokes pulses conditional on detection of a single Stokes photon. In Section 4.2.1 we theoretically analyze the experimental conditions necessary for generating high-fidelity single photons using this method. Section 4.2.2 describes the experimental generation of nonclassical anti-Stokes light, conditioned on detection of $n_S = 2$ Stokes photons, using the experimental setup described in Chapter 3. Section 4.3 describes changes and improvements made to the experimental setup in order to achieve single-photon generation. Finally, in Section 4.4 we describe experiments demonstrating the generation of single-photon anti-Stokes pulses, conditioned on detection of $n_S = 1$ Stokes

photon.

Single-photon generation, an essential capability for many applications in quantum information [20], has been accomplished in many different systems, including parametric down-converters [61, 117, 116, 105, 25], semiconductor quantum dots [99, 128, 111, 110, 126, 127], mesoscopic quantum wells [69], molecules [92, 22, 82], single atoms in cavities [74, 97], single ions [13, 67], one-atom masers (i.e., micromasers) [122, 17], nitrogen-vacancy centers in diamond [75, 10, 11], microstructure fiber [38, 39], and most recently, in experiments performed in our group and others, atomic ensembles [64, 30, 9, 35, 26]. There are several criteria a single-photon source needs to meet for applications in quantum-information science. These criteria include: directional emission, narrow bandwidth, high emission rate, high fidelity (i.e., very low probability of more than one photon being emitted), and on-demand emission (i.e., a photon can be produced with certainty at any desired time). In addition, each photon emitted by the source should be indistinguishable from all the others, a requirement necessary for the realization of linear-optics quantum computation [72], for example. Each method for single-photon generation listed above has its own advantages and disadvantages, and because of this, specific methods may be more suited to some applications than others.

The method of producing single photons described in this chapter has many desirable properties. As described in previous chapters, momentum conservation ensures that detection of a Stokes photon in a well-defined spatial mode ensures direction emission of the single-photon anti-Stokes pulse upon retrieval of the atomic coherence. This directional emission means that our photons can easily be coupled into a

single-mode fiber for transmission to other locations, as is done in the experiments described in Chapter 5. The single-photons produced in our experiments have narrow bandwidths of a few MHz (as measured in the experiments described in Chapter 5), because the single-photons are retrieved using EIT, which has a transmission window with a bandwidth of a few MHz in our experiments. This is important since a narrow bandwidth reduces group-velocity dispersion in optical-fiber propagation [125], and also implies large coherence lengths, which makes the indistinguishability criterion easier to achieve. Narrow bandwidth photons also allow narrow filtering that may enable daytime free-space quantum cryptography [5, 107]. In addition to the long coherence lengths of our photons enabled by EIT-based retrieval, EIT also gives us the ability to control the shape of our photons pulses to some degree (as demonstrated in Chapter 3 and Ref. [37]), giving us an additional degree of control over the indistinguishability criterion. We plan to explicitly verify the indistinguishability of different photons emitted by our source in future Hong-Ou-Mandel-type [62] experiments.

While our source meets the necessary criterion for directionality, bandwidth, and indistinguishability, the on-demand emission, emission rate, and fidelity need to be improved in order to be useful for applications in quantum cryptography and quantum communication. The current status and potential improvements to these properties are discussed in the conclusion to this chapter.

4.2 Conditionally Generated Nonclassical States of Light

4.2.1 Conditions for High-Fidelity Single-Photon Generation

The correlations between the Stokes and anti-Stokes pulses allow for the conditional preparation of the anti-Stokes pulse with intensity fluctuations that are suppressed compared with classical light. That is, under ideal conditions, conditioning on detection of n Stokes photons creates and atomic excitation with n excitations, which is transferred to an n-photon anti-Stokes pulse upon retrieval. We now turn to a quantitative examination of the feasibility of conditional Fock state generation using our preparation and retrieval technique. For applications in long-distance quantum communication, the quality of the atomic state preparation is the most important quantity. Assuming perfect atom-photon correlations in the write Raman processes, we can find the density matrix $\hat{\rho}$ for the number of atomic spin-wave excitations conditioned on the detection of n_S Stokes photons. Here we consider only the spin-wave modes correlated with our detection mode. For example, in the absence of losses and background, the conditional atomic density matrix is simply $\hat{\rho}(n_S) = |n_S\rangle\langle n_S|$. Loss on the Stokes channel (characterized by transmission coefficient α_S) leads to a statistical mixture of spin-wave excitations,

$$\hat{\rho}_{\alpha_S}(n_S) = \frac{1}{P_{\alpha_S}(n_S)} \sum_{n=n_S}^{\infty} P^{SW}(n) \begin{pmatrix} n \\ n_S \end{pmatrix} \alpha_S^{n_S}(1-\alpha_S)^{n-n_S} \mid n\rangle\langle n \mid, \tag{4.1}$$

where $P^{SW}(n)$ is the unconditional probability to obtain n spin-wave excitations, $P_{\alpha_S}(n_S)$ is the probability to detect n_S Stokes photons (ensuring normalization), and

$\begin{pmatrix} n \\ n_S \end{pmatrix}$ represents the binomial coefficient. Background on the Stokes channel further complicates the picture, as one cannot distinguish between Stokes signal photons and background photons. Including the probability for m background counts $P_B(m)$ in our model, we find

$$\hat{\rho}_{\alpha_S}^{(B)}(n_S) = \frac{1}{\tilde{P}_{\alpha_S}(n_S)} \sum_{i=0}^{n_S} \hat{\rho}_{\alpha_S}(n_S - i) P_{\alpha_S}(n_S - i) P_B(i), \tag{4.2}$$

where the normalization factor $\tilde{P}_{\alpha_S}(n_S)$ is the overall probability to have n_S counts of either Stokes signal or background photons.

Since we are primarily interested in the conditional quantum state of the atomic ensemble, we can use the density-matrix formalism to calculate the fidelity with which we create the desired atomic state, $|n_S\rangle$:

$$F = \langle n_S | \hat{\rho}_{\alpha_S}^{(B)}(n_S) | n_S \rangle. \tag{4.3}$$

We can furthermore calculate the Mandel Q-factor [91] associated with this atomic state

$$Q = \frac{\langle n_{SW}^2 \rangle - \langle n_{SW} \rangle^2}{\langle n_{SW} \rangle} - 1, \tag{4.4}$$

where $\hat{n}_{SW}$ is the number operator for spin-wave excitations. This quantity can also be interpreted as the Mandel Q-factor associated with a perfectly retrieved anti-Stokes pulse. $Q \geq 0$ for classical states and $Q = -1$ for Fock states.

To determine the unconditional probability distribution for the spin-wave excitations $P^{SW}(n)$, we must find the effective number of transverse modes which contribute to the Raman processes. We identify two extreme regimes which permit analytic treatment: a single mode regime where the number of excitations in the ^{87}Rb cell follows

Bose-Einstein (thermal) statistics because they are created in a spontaneous process, and a multimode regime that has Poisson statistics since the statistics of many Bose-Einstein modes quickly approach Poisson statistics as the number of modes increases (see Appendix A.3 and Ref. [109]). We find in both cases that the quantities F and Q depend on two experimental parameters θ ($\sim$ number of lost Stokes photons) and υ ($\sim$ noise to signal ratio on the Stokes channel), which are defined in Table 4.1.

Regime	*Single mode*	*Multimode*
Parameters	$\theta_T = \frac{\bar{n}}{1+\bar{n}}(1-\alpha_S)$	$\theta_P = \bar{n}(1-\alpha_S)$
	$\upsilon_T = \frac{\bar{n}_S^{BG}}{\frac{\alpha_S \bar{n}}{1+\alpha_S \bar{n}}}$	$\upsilon_P = \frac{\bar{n}_S^{BG}}{\alpha_S \bar{n}}$
Q ($\upsilon = 0$)	$\frac{\theta_T}{1-\theta_T} - \frac{n_S}{n_S+\theta_T}$	$-\frac{n_S}{n_S+\theta_P}$
Q ($\upsilon \neq 0$)	$\sim Q[\upsilon_T = 0] + \upsilon_T(1+\theta_T)$	$\frac{-n_S}{(1+\upsilon_P)(n_S+\theta_P+\upsilon_P\theta_P)}$
F ($\upsilon = 0$)	$(1-\theta_T)^{n_S+1}$	$e^{-\theta_P}$
F ($\upsilon << 1$)	$\sim (1-\theta_T)^{n_S+1}(1-\upsilon_T)$	$\sim \frac{e^{-\theta_P}}{(1+\upsilon_P)^{n_S}}(1+O(\upsilon_P\theta_P))$

Table 4.1: Scaling for the anti-Stokes pulse Q-parameter and Fock state fidelity F. $\bar{n}$ refers to the mean number of excitations in the rubidium cell, $\bar{n}_S^{BG}$ is the mean photon number of background counts in the write channel (we assume they are mainly due to leak of the write laser and so follow Poisson statistics), α_S is the Stokes detection efficiency and n_S is the number of Stokes photons on which we condition. The mean number of atomic excitations is calculated via $\langle n_{SW} \rangle = tr(\hat{\rho}_{\alpha_S} \hat{n}_{SW})$; similarly $\langle n_{SW}^2 \rangle = tr(\hat{\rho}_{\alpha_S} \hat{n}_{SW}^2)$. The subscript T (P) refers to thermal (Poisson) photon statistics of the unconditional Stokes light.

We now turn to the conditions under which high-quality Fock states can be generated in the presence of loss and background. In principle, one can compensate for loss in the Stokes channel by decreasing the probability for excitations in the atomic ensemble, so that the probability for more than one spin excitation is negligible. In

this situation, a lossy Stokes channel will rarely register a photon, but when a photon is detected, it almost certainly came from a single spin-wave excitation. Conversely, one can compensate for background in the absence of loss by increasing the number of spin-wave excitations so that $\bar{n} \gg \bar{n}_S^{BG}$. When both losses and background are present, there exists an optimum value for $\bar{n}$ that maximizes fidelity and minimizes the Mandel Q-parameter. Tuning the mean number of excitations to this optimum gives us the smallest possible Q. However, this minimum is not always negative, which means that for certain conditions we cannot conditionally produce nonclassical states. For example, in the multimode case, the border between classical and nonclassical state generation is determined by the parameter

$$\zeta = \frac{\upsilon_P \theta_P}{n_s} = \frac{\bar{n}_S^{BG}}{n_S} \left(\frac{1 - \alpha_S}{\alpha_S} \right). \tag{4.5}$$

Provided that $\zeta \ll 1$, one can always find a specific number of excitations in the cell that allows conditional production of number-squeezed atomic states. For instance, if $\zeta \sim 0.1$, the optimal Q is found to be ~ -0.5 in both multi-mode and single-mode cases.

4.2.2 Experimental Observations

In order to quantify the performance of this technique, we measured the second-order intensity correlation function $g_{n_S}^{(2)}(AS)$ (from which we calculate the Mandel Q parameter) and mean number of photons $\bar{n}_{n_S}^{AS}$ for the anti-Stokes pulse conditioned on the detection of n_S photons in the Stokes channel, using the experimental setup shown in Fig. 3.2. The results of these measurements are shown in Fig. 4.1. The second-order intensity correlation function, first defined and utilized in a pair of seminal papers

published by Roy Glauber in 1963 [48, 49], can be defined for a field at position x at time t, and position y at time t' as

$$g^{(2)}(x\,t, y\,t') \equiv \langle : \hat{n}_x(t)\,\hat{n}_y(t') : \rangle / \langle \hat{n}_x(t) \rangle \langle \hat{n}_y(t') \rangle, \tag{4.6}$$

where $\hat{n}_i(t)$ denotes the photon-number operator for the field at position i and time t, and $::$ denotes operator normal ordering.

In our experiments, the positions x and y are the anti-Stokes detectors $AS1$ and $AS2$ in the two arms of the 50-50 beamsplitter that divide the anti-Stokes field (see Fig. 3.2), and we measure these two fields at the same time. We denote this specific second-order correlation function $g^{(2)}(AS)$, defined as

$$g^{(2)}(AS) = \langle \hat{n}_{AS1}\,\hat{n}_{AS2} \rangle / \langle \hat{n}_{AS1} \rangle \langle \hat{n}_{AS2} \rangle, \tag{4.7}$$

where $(\hat{n}_{AS1}, \hat{n}_{AS2})$ is the number operator for detector $(AS1, AS2)$. For classical anti-Stokes fields, $g^{(2)}(AS) \geq 1$, whereas an ideal Fock state with n photons has $g^{(2)}(AS) = 1 - 1/n$ (see Appendix A.3 for details).

In the measurements shown in Fig. 4.1, we measure $g^{(2)}(AS)$ and the mean number of anti-Stokes photons $\bar{n}^{AS}$ conditioned on detection of n_S Stokes photons, which we denote $g^{(2)}_{n_S}(AS)$ and $\bar{n}^{AS}_{n_S}$, respectively. Note that the mean number of anti-Stokes photons grows linearly with n_S, while $g^{(2)}_{n_S}(AS)$ drops below unity, indicating the nonclassical character of the anti-Stokes photon states. In the presence of background counts, $g^{(2)}_{n_S}(AS)$ does not increase monotonically with n_S as expected in the ideal case, but instead exhibits a minimum at $n_S = 2$ of $g^{(2)}_{n_S=2}(AS) = 0.78 \pm 0.08$. Physically this behavior results from the trade-off between smaller n_S giving a smaller ideal value for $g^{(2)}$, and smaller n_S resulting in a smaller signal-to-noise ratio. In other words, for our experimental conditions, the parameter ζ (see Eq. (4.5) is minimum for $n_S = 2$.

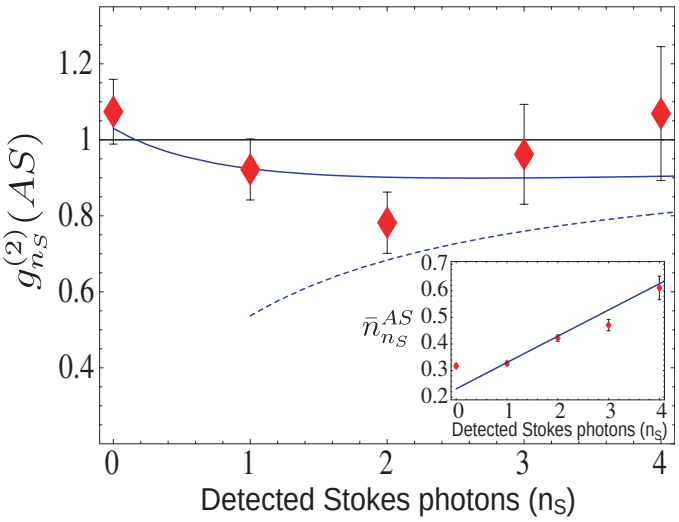

Figure 4.1: Conditional nonclassical state generation. Diamonds show experimentally measured values of $g^{(2)}_{n_S}(AS)$ as a function of the number of detected Stokes photons. The measured mean photons numbers were $\bar{n}_S = 1.06$ and $\bar{n}_{AS} = 0.36$. The solid line shows the result of a theoretical model. (**Inset**) Measured mean anti-Stokes number $\bar{n}^{AS}_{n_S}$ conditioned on the Stokes photon number n_S. The solid line represents $\bar{n}^{AS}_{n_S}$ as predicted by the model. Statistical error bars are ± one standard deviation (see Appendix B.1).

The Mandel Q parameter [91] can be calculated using $Q^{AS}_{n_S} = \bar{n}^{AS}_{n_S}(g^{(2)}_{n_S}(AS) - 1)$; from the measurements we determine $Q^{AS}_{n_S=2} = -0.09 \pm 0.03$ for conditionally generated states with $n_S = 2$ ($Q \geq 0$ for classical states and $Q = -1$ for Fock states). Experimental imperfections such as loss and background can be accounted for in a theoretical model that yields reasonable agreement with experimental observations (solid curve in Fig. 4.1). The parameter values used in the model were estimated from experimental measurements and given by: $\alpha_S = 0.35$, $n^{BG}_S = 0.27$ ($\alpha_{AS} = 0.1$, $n^{BG}_{AS} = 0.12$) on the Stokes (anti-Stokes) channel. Using this model corrected for loss and background on the retrieval channel (dashed line in Fig. 4.1), we estimate ($\bar{n}^{AS}_{n_S=2}$, $Q^{AS}_{n_S=2}$) to be approximately (2.5, -0.85).

Although the corrected parameters are closer to the ideal limit, they still do not correspond to a perfect Fock state. This is due to loss and background in the preparation channel, which prevent measurement of the exact number of created spin excitations. In principle, the conditional state preparation can be made insensitive to overall Stokes detection efficiency α_S by working in the regime of a very weak excitation [34]; however, Stokes channel background counts n_S^{BG} prevent one from reaching this regime in practice. As discussed in the previous section, a qualitative condition for high quality Fock state generation is given by $\zeta \equiv n_S^{BG}(1-\alpha_S)/n_S\alpha_S \ll 1$. This condition is only marginally fulfilled in our experiments ($\zeta \sim 0.3$ for $n_S = 2$), accounting for the imperfectly prepared atomic states. We shall see in the next section that refinements in the Stokes detection system and better transverse mode selection, in addition to reduced noise on the anti-Stokes channel, resulted in conditional Fock state generation with significantly improved purity, allowing us to reach the regime of conditional single-photon generation.

4.3 Experimental Conditions allowing Conditional Single-Photon Generation

In this section, we describe changes made to the experimental setup shown in Figs. 3.2 and 3.3, designed to improve the conditions for high-fidelity single-photon generation. In Section 4.4 we describe the experimental generation of conditional single-photon pulses using this improved experimental setup.

A schematic and photograph of the improved setup are shown in Figs. 4.2 and 4.3,

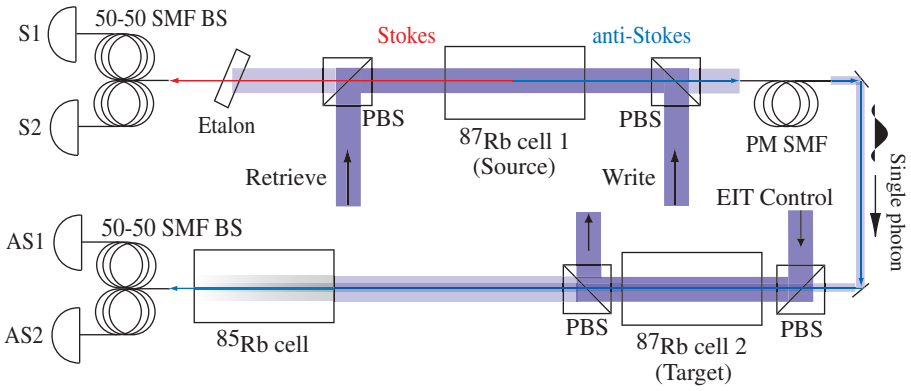

Figure 4.2: Experimental setup. The write and retrieve lasers (EIT control laser and anti-Stokes field) counter-propagate [3] (co-propagate) inside the magnetically-shielded source (target) ensemble. The write (retrieve) laser has a diameter of 1 mm (3 mm) at the center of the source ensemble. The single spatial mode defined by the detection fibers and optics has a diameter of 200 μm at the center of the source ensemble. The etalon (^{85}Rb cell) is used to reflect (absorb) the fraction of the write (retrieve / EIT control) laser not filtered by the polarizing beamsplitters; this requires a retrieve and EIT control laser detuning of +400 MHz. The source (target) ensemble is a 4.5 cm-long isotopically pure ^{87}Rb vapor cell with 7 Torr (8 Torr) of neon buffer gas. Target ensemble and EIT control field are absent (present) for the experiments described in Chapter 4 (Chapter 5). Abbreviations: PBS for polarizing beamsplitter (beam-splitting Glan-Thompson crystal polarizer); SMF for single-mode fiber; PM for polarization maintaining; BS for beamsplitter; and S1,S2 (AS1,AS2) for avalanche photodetectors (APDs) for the Stokes (anti-Stokes) channel.

respectively. The primary difference compared to setup shown in Figs. 3.2 and 3.3 is that in the improved setup, the write and retrieve lasers are counter-propagating, overlapping inside the magnetically shielded "source ensemble". As before, the write (retrieve) laser is filtered (to 5 parts in 10^6) from the Stokes (anti-Stokes) field using polarizing beamsplitters. The Stokes field is sent through further frequency-based filtering (etalon), and then detected using a single-mode fiber beamsplitter and two APDs. The anti-Stokes field is sent to the "target ensemble" via a 3-meter long polarization-maintaining fiber, then sent through frequency-based filtering (^{85}Rb en-

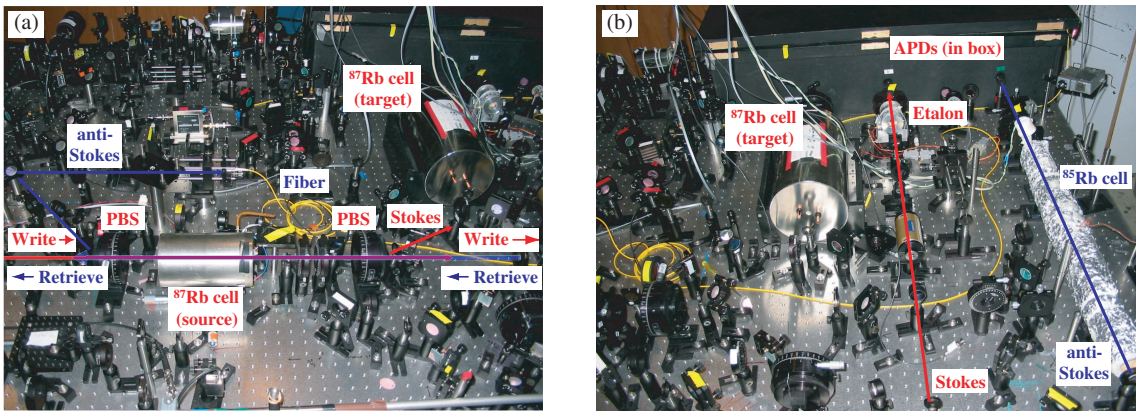

Figure 4.3: Photograph of the experimental setup. **(a)** The source ensemble (inside three layers of magnetic shielding), with the paths for the write and retrieve lasers, and Stokes and anti-Stokes photons marked. The anti-Stokes photons are separated from the retrieve laser at a polarizing beamsplitter (PBS) and directed to a polarization maintaining single-mode fiber (yellow fiber in the picture), which directs the photons to the target cell. **(b)** Etalon and ^{85}Rb cell used for frequency filtering of the Stokes from the write laser and the anti-Stokes from the retrieve laser. Target ensemble and EIT control field are absent (present) for the experiments described in Chapter 4 (Chapter 5)

semble), and finally is detected using a single-mode fiber beamsplitter and two APDs.

The creation and retrieval of the atomic coherence used to generate single photons occurs in the source ensemble. In the experiments described in Chapter 5, we then transmit the single photons to the target ensemble to perform EIT-based slowing, storage, and retrieval. For the experiments described in this chapter, the target ensemble was removed from the setup and the EIT control field was turned off, in order to characterize the single photons emitted from the source ensemble.

The counter-propagating geometry serves two functions, one practical, and the other fundamental. The practical function involves the precise alignment of the single modes defined by the Stokes and anti-Stokes single-mode detection fibers. In the experiments described in previous chapters, our detection fibers were multi-mode,

and alignment was accomplished by using intense write and retrieve lasers to generate strong Stokes and anti-Stokes signals; the detection fibers were then aligned simply by maximizing the Stokes and anti-Stokes signals detected by the two fibers.

The experiments described in this chapter use single-mode detection fibers. Momentum conservation (see Eq. (1.14)) means that correlations between the Stokes and anti-Stokes fields only occur within a single spatial mode. Since we excite multiple modes, simply aligning on maximum signal does not ensure that the single modes defined by the Stokes and anti-Stokes detection fibers are correlated modes. The counter-propagating geometry, however, allows us to precisely align these modes. By turning on the write and retrieve lasers, and sending a laser field at the Stokes frequency backwards through the anti-Stokes detection fibers, we preferentially seed emission into this mode. By then aligning the Stokes detection fiber to maximize the signal, we ensure that the Stokes and anti-Stokes fiber modes are connected by momentum conservation, and therefore correlated. In addition, we observe experimentally that in the case of perfectly counter-propagating write and retrieve lasers, it is sufficient to simply send a laser field backwards through the Stokes fibers and maximize detection of this field with the anti-Stokes fibers, without turning on the write and retrieve lasers.

In addition to these practical considerations, more fundamental theoretical considerations also suggest the use of counter-propagating write and retrieve lasers. A theoretical analysis of the optimal geometry for retrieval of a stored atomic excitation is given in Ref. [3]. This analysis concludes that a geometry where the write and retrieve lasers are counter-propagating plane waves maximizes the correlations between

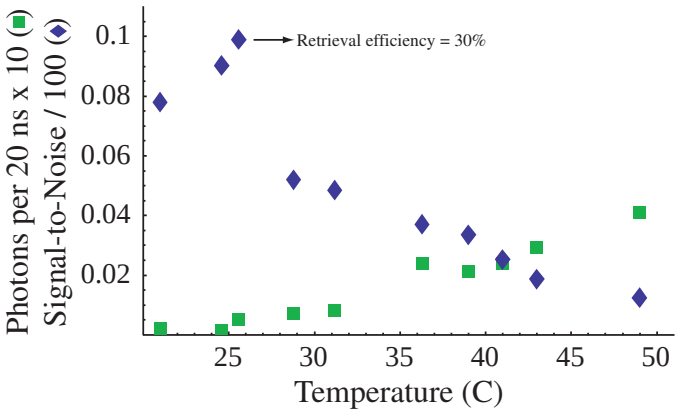

Figure 4.4: Noise ×10 (green squares) and signal-to-noise ratio/100 (blue diamonds) on the anti-Stokes channel as a function of temperature. Data was taken for the first 20 ns after turn-on of the retrieve laser. The data point at T = 26°C corresponds to a retrieval efficiency of 30%.

the Stokes and anti-Stokes fields. It is shown that if the write and retrieve lasers are co-propagating, an atomic excitation stored in a single transverse Hermite-Gaussian mode cannot be retrieved into a single-mode anti-Stokes field; in this co-propagating geometry, the retrieved anti-Stokes will inevitably occupy more than one transverse Hermite-Gaussian mode. If the write and retrieve lasers are counter-propagating plane waves, however, it is shown that retrieval of an atomic excitation in a single transverse mode leads to an anti-Stokes field in a single transverse mode. The physical basis for this behavior involves the phase conjugation property [15, 98, 3] of the four-wave mixing interaction involving the write, retrieve, Stokes, and anti-Stokes fields.

In addition to this improved geometry, by decreasing the temperature of the atomic ensemble relative to the experiments described in Chapter 3, we were able to greatly improve the signal-to-noise ratio on the anti-Stokes channel. As described

in Chapter 3, the dominant noise mechanism on the anti-Stokes channel was four-wave mixing due to the undesired coupling of the retrieve laser to the $|g\rangle \rightarrow |e\rangle$ transition (see Fig. 3.9). Since the scattering rate for the four-wave mixing process and the rate of retrieval of the atomic coherence depend differently on the atomic density, by decreasing the temperature of the ensemble, and therefore the atomic density, the signal-to-noise ratio was greatly increased.

Specifically, in Ref. [3], it is shown that in the zeroth-order adiabatic solution (i.e., the limit of infinite optical depth, $d_0 \rightarrow \infty$) of the problem of retrieval of a stored atomic excitation, the number of retrieved anti-Stokes photons emitted per unit time from the end of the atomic ensemble (at position $z = L$) is given by

$$dn_{AS}(z = L, t)/dt = \frac{|\Omega_R|^2}{(d_0\gamma)} e^{-2t/\tau} \langle \hat{S}^\dagger(L - v_g t, t = 0) \hat{S}(L - v_g t, t = 0) \rangle, \tag{4.8}$$

where Ω_R is the retrieve-laser Rabi frequency and is assumed to be constant, d_0 is the optical depth, L is the length of the ensemble, γ is the decay rate of the excited atomic state, τ is a characteristic ground-state decoherence time, and $\langle \hat{S}^\dagger(z, t = 0) \hat{S}(z, t = 0) \rangle$ is the mean number of $|g\rangle - |s\rangle$ atomic-coherence excitations at position z prior to retrieval.

Meanwhile, at short times, the number of noise photons emitted per unit time due to the undesired four-wave mixing process scales as

$$dn_{noise}/dt \sim \xi(1 + \xi t + ...), \tag{4.9}$$

where $\xi = \frac{|\Omega_R|^2}{\Delta^2} \gamma d_0$, where Δ is the detuning of the retrieve laser from resonance.

From these expressions, we see that the signal-to-noise ratio should increase indefinitely as the optical depth decreases. As shown in Fig. 4.4, the signal-to-noise

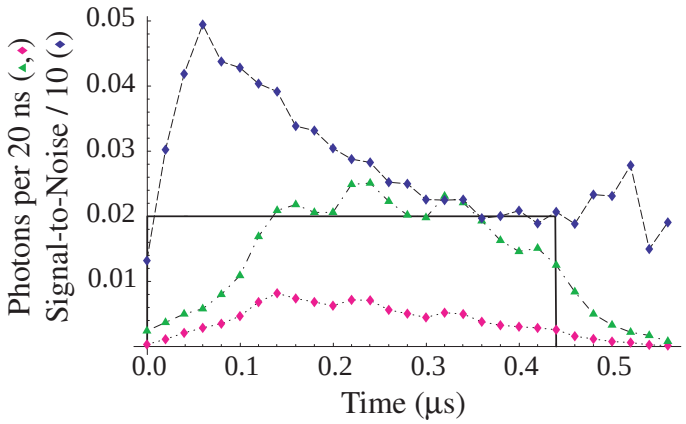

Figure 4.5: Signal (magenta diamonds), noise (green triangles), and signal-to-noise ratio/10 (blue diamonds) on the anti-Stokes channel as a function of time. Atomic ensemble temperature = 54°C. Solid line represents retrieve laser amplitude modulation. The differing growth of the signal and noise with time results in a maximum in the signal-to-noise ratio in the first hundred nanoseconds. Lines are only to guide the eye.

ratio is increased by a factor of 10 by decreasing the temperature from 50°C to 26°C. At 26°C, we observe a maximum in signal-to-noise ratio, with lower temperatures resulting in lower ratios. This maximum occurs because the derivation of Eq. (4.8) is only the zeroth order adiabatic solution. Performing a calculation of the first-order non-adiabatic solution (i.e., finite d_0) shows that the error in retrieval increases with decreasing d_0 [3, 50]. Therefore the maximum signal-to-noise ratio at 26°C results from a competition between the increasing ratio of EIT retrieval rate to four-wave mixing rate with decreasing atomic density, and the decreasing EIT retrieval efficiency with decreasing atomic density.

Finally, we were also able to utilize the differing growth in time of the rate of EIT retrieval and four-wave mixing to improve the signal-to-noise ratio. Fig. 4.5 shows the detected number of signal and noise photons per 20 ns as a function of time after

the retrieve laser is turned on; also plotted is the signal-to-noise ratio as a function of time. The different time dependence of the signal and noise results in a peak of signal-to-noise ratio in the first few hundred nanoseconds after the the turn-on of the retrieve laser. By gating the APDs to only detect in the first few hundred nanoseconds after the retrieve laser turn-on, the signal-to-noise ratio can be increased relative to detecting the entire pulse.

We can understand this time dependance by comparing the time dependance of Eqs. (4.8) and (4.9). While the rate of anti-Stokes emission decays exponentially with time due to the ground-state spin decoherence, the four-wave mixing rate increases with time. This should result in a signal-to-noise ratio that is maximum at the beginning of retrieval and decays as time increases. From Fig. 4.5 we see that the signal-to-noise ratio is not maximum at the onset of retrieval, but at $t \sim 50\,\mathrm{ns}$ after the onset. This is due to transient dynamics not included in the zeroth-order adiabatic solution that prevent the anti-Stokes field from being generated immediately [3].

4.4 Single-Photon Generation

4.4.1 Experimental Demonstration

The basic idea of our experiments is illustrated in Fig. 4.6. Single photons are prepared using an ensemble of room-temperature ^{87}Rb atoms called the source ensemble, by first creating a single spin excitation via Raman scattering combined with single-photon detection, and later converting this atomic excitation "on demand" into a single photon propagating in an optical fiber [76, 118, 30, 37, 64, 4, 9, 94, 95].

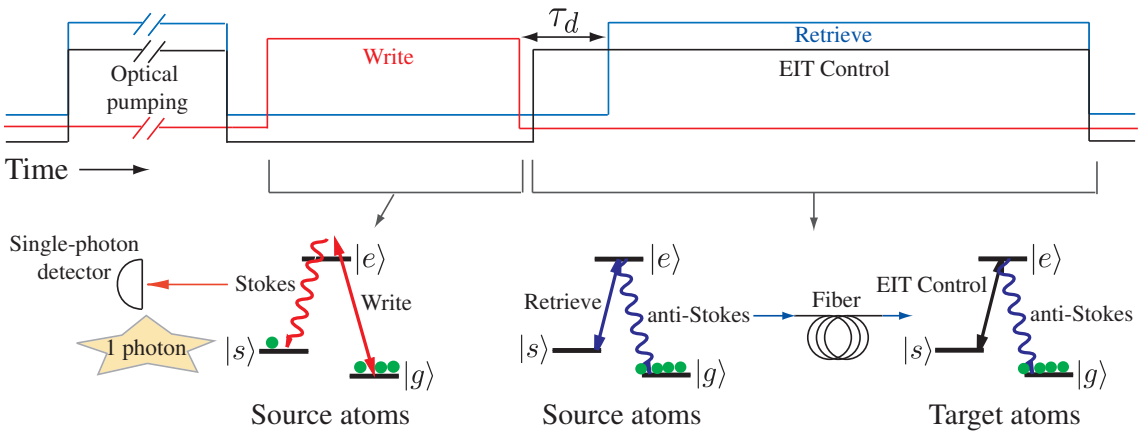

Figure 4.6: Experimental procedure. Two ensembles of ^{87}Rb atoms are used, the source and target ensembles. In zero magnetic field, the atoms can be pictured as a three-level atom, with: $|g\rangle = |5^2S_{1/2}, F = 1\rangle$, $|s\rangle = |5^2S_{1/2}, F = 2\rangle$, and $|e\rangle$ corresponds to $|5^2P_{1/2}, F' = 1\rangle$ and $|5^2P_{1/2}, F' = 2\rangle$. The write (retrieve) laser couples the $|g\rangle - |e\rangle$ ($|s\rangle - |e\rangle$) transition of the source atoms; the EIT control laser couples the $|s\rangle - |e\rangle$ transition of the target atoms. Target ensemble and EIT control field are absent (present) for the experiments described in Chapter 4 (Chapter 5).

Successful preparation of the single-photon pulse is conditional on detecting a single Raman-scattered photon [37, 30]. In the experiments described in the next chapter, the single photons are directed via an optical fiber to a second atomic ensemble (target ensemble), where their controlled interaction with coherently driven atoms is studied by combining EIT-based high-resolution spectroscopy and photon-counting measurements. For the experiments described in this chapter, we remove the target ensemble from the setup and turn off the EIT control laser in order to characterize the single photons emitted from the source ensemble.

Our measurements demonstrate that the source ensemble emits narrow-bandwidth, frequency-tunable single photons with properties matching those of narrow atomic resonances [30, 37]. As illustrated in Fig. 4.6, the source ensemble is initially pre-

pared in the ground state $|g\rangle$. As in the experiments described in Chapters 2 and 3, we represent the structure of the ^{87}Rb atoms in zero magnetic field as a three-level atom with $|g\rangle = |5^2S_{1/2}, F = 1\rangle$, $|s\rangle = |5^2S_{1/2}, F = 2\rangle$, and $|e\rangle = |5^2P_{1/2}, F' = 1\rangle$ and $|5^2P_{1/2}, F' = 2\rangle$. Atomic spin excitations to the state $|s\rangle$ are produced via spontaneous Raman scattering, induced by the write laser. In this process, correlated pairs of Stokes photons and atomic excitations into the state $|s\rangle$ are created. Conditioned upon detecting a single Stokes photon, the stored single spin-wave quantum is coherently converted into a single-photon anti-Stokes pulse by applying a second near-resonant laser beam (retrieve laser) after a controllable delay time [79, 103]. The direction, bandwidth, and central frequency of the single-photon anti-Stokes pulse are determined by the direction, intensity, and frequency of the retrieve laser [37]. Specifically, the retrieve laser controls the rate of retrieval and propagation of the anti-Stokes pulse, thereby controlling its duration, and consequently its bandwidth. The central frequency of the single-photon pulse differs from the frequency of the retrieve laser by a fixed amount given by the $|g\rangle - |s\rangle$ atomic transition frequency. We study the photon-number fluctuations in the Stokes and the anti-Stokes pulses using a Hanbury-Brown-Twiss-type setup, which allows us to measure the normalized second-order correlation function, see Eq. (4.6) [48, 49, 91, 85].

As previously mentioned, to quantify the properties of the single-photon source, the target ensemble was removed from the beam path. Fig. 4.7 shows a measurement of the photon-number fluctuations of the anti-Stokes field conditioned on detecting a single Stokes photon, as a function of the detection probability $p\eta_S$ in the Stokes channel. The function $g^{(2)}(AS||n_S = 1)$ (see Fig. 4.7) represents a measure of the

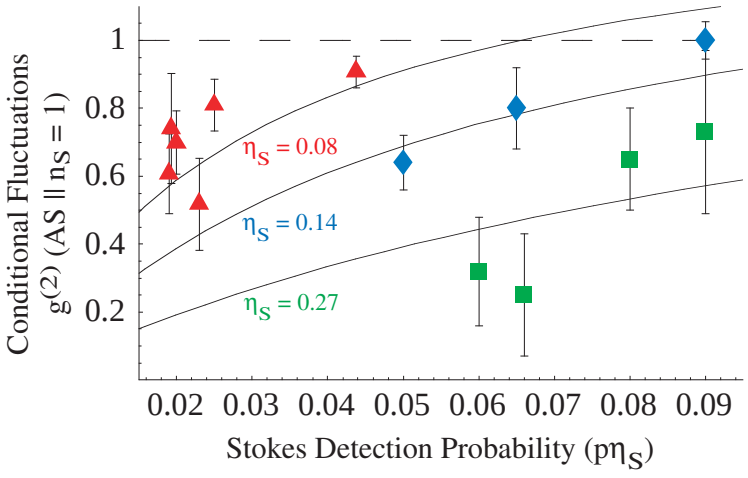

Figure 4.7: Observation of conditional single-photon generation. Anti-Stokes fluctuations, conditioned on detection of a single Stokes photon, are characterized by the correlation function $g^{(2)}(AS||n_S = 1) = \langle \hat{n}_{AS1}\, \hat{n}_{AS2}\rangle / \langle \hat{n}_{AS1}\rangle \langle \hat{n}_{AS2}\rangle$, where $(\hat{n}_{AS1}, \hat{n}_{AS2})$ is the number operator for detector $(AS1, AS2)$, see Fig. 4.2. The dashed line represents the classical limit of $g^{(2)}(AS||n_S = 1) = 1$. Measurements are shown for three values of the Stokes channel transmission: $\eta_S = 0.08$ (red triangles), $\eta_S = 0.14$ (blue diamonds), and $\eta_S = 0.27$ (green squares). Solid lines represent a theoretical model (see Section 4.4.2 and Ref. [36]) for η_S equal to 0.08, 0.14, and 0.27 respectively. For this data, source ensemble temperature ≈ 26°C (estimated optical depth ≈ 4). Anti-Stokes channel transmission is 10%. Experimental repetition rate = 72 kHz. Statistical error bars (see Appendix B.1) are $\pm$ one standard deviation and represent averages of $\sim 400,000$ anti-Stokes detection events, corresponding to total averaging times of ~ 1 hour per point.

photon-number fluctuations in the anti-Stokes pulses. An ideal single-photon source has no photon-number fluctuations ($g^{(2)}(AS||n_S = 1) = 0$); for classical coherent states $g^{(2)}(AS||n_S = 1) = 1$ (see Appendix A.3). In Fig. 4.7, $p\eta_S$ is varied by changing the Raman excitation probability p via the write laser intensity (η_S is the overall Stokes channel transmission). As p becomes much smaller than unity, we observe substantial suppression of the conditional intensity fluctuations in the anti-Stokes pulses ($g^{(2)} = 0.3 \pm 0.2$ for $p\eta_S = 0.06$ and $\eta_s = 0.27$) compared to the classical limit of unity. Typical conversion efficiencies of atomic excitations into anti-Stokes photons is

8% - 15%. These observations are in good agreement with a simple theoretical model (see solid lines in Fig. 4.7, Ref. [36], and Section 4.4.2) that considers realistic losses and background photons. The presence of loss on the Stokes channel means that detection of a single Stokes photon can result in more than one atomic excitation. Upon retrieval, this results in the undesired emission of more than one anti-Stokes photon. Even in the presence of loss, one can obtain almost perfect preparation of an atomic state with a single excitation by ensuring that the Raman excitation probability p is much less than one. In this case, the probability of emitting two photons is suppressed by $p \ll 1$. This condition is satisfied when $p\eta_S \ll \eta_S$, in agreement with the experimental observations in Fig. 4.7.

4.4.2 Theoretical Model

To model the effects of loss and noise on the anti-Stokes channel on the fidelity of single photon generation [36], we consider the system shown in Fig. 4.8. We assume the atomic state has been prepared by the write laser, and we characterize this state by the expectation value $\langle N_s \rangle$ and variance $\mathrm{Var}(N_s) \equiv \langle N_s^2 \rangle - \langle N_s \rangle^2$ of the number of atoms in state $|s\rangle$. We assume perfect retrieval of the atomic state such that the probability distribution of the anti-Stokes photons retrieved from such an atomic state is characterized by an expectation value $\langle N_{AS} \rangle = \langle N_s \rangle$ and variance $\mathrm{Var}(N_{AS}) = \mathrm{Var}(N_s)$. We model loss in the system by assuming the anti-Stokes photons must pass through a beamsplitter with transmission η_{AS}. We model noise in the system by assuming the presence of two fields of background photons: one with Poissonian statistics ($\mathrm{Var}(N) = \langle N \rangle$), and the other with thermal statistics ($\mathrm{Var}(N) = \langle N \rangle +$

$\langle N\rangle^2$). We then assume that the attenuated anti-Stokes field, Poissonian background field, and thermal background field are detected via a beamsplitter and two APDs as in the actual experiment (see Fig. 4.2).

Employing this model to calculate the second-order correlation function $g^{(2)}(AS) = \langle \hat{n}_{AS1}\, \hat{n}_{AS2}\rangle / \langle \hat{n}_{AS1}\rangle \langle \hat{n}_{AS2}\rangle$, where $(\hat{n}_{AS1}, \hat{n}_{AS2})$ is the number operator for detector $(AS1, AS2)$, see Fig. 4.2, we obtain:

$$g^{(2)}(AS) = 1 - \frac{1}{\langle N_s\rangle} \cdot \frac{1 - \bar{b}_t^2/(\eta_{AS}^2\langle N_s\rangle) - \mathrm{Var}(N_s)/\langle N_s\rangle}{(1 + (\bar{b}_t + \bar{b}_p)/(\eta_{AS}\langle N_s\rangle))^2}, \tag{4.10}$$

where $\bar{b}_t$ and $\bar{b}_p$ represent the average number of background photons with thermal and Poissonian statistics respectively, and η_{AS} represents the overall transmission fraction of the anti-Stokes channel. Although seemingly complicated at first glance, the physical process each term represents can be easily understood. First of all, for single-photon generation, one desires to prepare the atomic state such that there is exactly one atom in the state $|s\rangle$, which will then be retrieved to create one anti-Stokes photon. That is, ideal preparation results in an atomic state where $\mathrm{Var}(N_s) = 0$ and $\langle N_s\rangle = 1$. In the ideal limit of perfect preparation and zero background photons, Eq. (4.10) reduces to $1 - 1/\langle N_s\rangle$, the well-known expression for the second-order correlation function of a Fock state with N_s photons (see Appendix A.3 for details). The other terms in the expression represent corrections to this ideal case. The term $(\bar{b}_t + \bar{b}_p)/(\eta_{AS}\langle N_s\rangle)$ in the denominator essentially represents the competition between "signal" $(\eta_{AS}\langle N_s\rangle)$ and "noise" $(\bar{b}_t + \bar{b}_p)$ to the calculation of $g^{(2)}(AS)$. The term $\bar{b}_t^2/(\eta_{AS}^2\langle N_s\rangle)$ in the numerator represents the increase in $g^{(2)}(AS)$ due to the excess noise of background photons with thermal statistics. The term $\mathrm{Var}(N_s)/\langle N_s\rangle$ in the numerator represents the increase in $g^{(2)}(AS)$ due to non-zero variance of the prepared

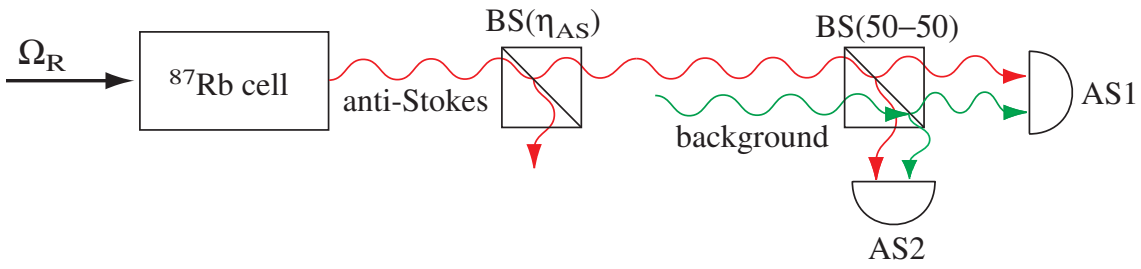

Figure 4.8: Model system used to calculate $g^{(2)}(AS)$ in the presence of loss and background photons on the anti-Stokes channel. Application of the retrieve laser (Ω_R) to the prepared atomic state leads to the coherent retrieval of anti-Stokes photons. Loss is modeled by assuming the anti-Stokes photons travel through a beamsplitter with transmission η_{AS}. In the model we consider the background photon field to consist of some part Poissonian statistics and some part thermal statistics. The 50-50 beamsplitter and two APDs (AS1, AS2) allow detection of $g^{(2)}(AS)$.

atomic distribution.

We are interested in calculating $g^{(2)}(AS)$ for the case where we condition on detection of a single photon in the Stokes channel, as we do in our experiments. We will denote $g^{(2)}(AS)$ conditioned on detection of n_S Stokes photons as $g^{(2)}(AS|n_S)$. Of the physical quantities appearing in the expression for $g^{(2)}(AS|n_S)$, all are measurable except for $\langle N_s|n_S\rangle$ and $\mathrm{Var}(N_s|n_S)$, the expectation value and variance of the atomic distribution in state $|s\rangle$, conditioned on detection of n_S Stokes photons. In the case of interest where $n_S = 1$, even though the variance of the detected Stokes photon distribution is always zero (since we condition on detection of a single Stokes photon), the variance of the resulting atomic distribution (and thus the variance of the retrieved anti-Stokes photon distribution) can be non-zero due to loss and background photons on the Stokes detection channel. Because of background photons, the detection of a single photon in the Stokes channel will sometimes result in zero atoms in the $|s\rangle$ state. Upon retrieval, such an atomic state results in zero anti-Stokes pho-

tons. In practice, however, the experiments are carried out under conditions of "weak excitation" ($p \ll 1$), meaning that background on the Stokes channel is negligible. Therefore, in the model we assume zero background on the Stokes channel. The effect of loss on the Stokes channel is more profound. The presence of loss means that detection of a single Stokes photon can result in an atomic state with N_s atoms in the state $|s\rangle$, where N_s can be any number greater than or equal to one. Upon retrieval, such an atomic state results in one or more anti-Stokes photons, which does increase the value of $g^{(2)}(AS|n_S = 1)$ from the ideal single-photon value of zero. Experimentally, in the case of single-photon generation, one can still obtain almost perfect preparation of the atomic state ($\mathrm{Var}(N_s)$=0,$\langle N_s\rangle$=1) in the presence of loss by ensuring that the probability p of emitting a single Stokes photon during the preparation by the write laser is much less than one. In terms of experimentally measurable parameters, this condition $p \ll 1$ becomes $p\eta_S \ll \eta_S$, where η_S is the Stokes channel transmission, and $p\eta_S$ is the probability of detecting a single Stokes photon during preparation of the atomic state. Physically, this condition simply means that if the probability of a single atomic excitation is sufficiently small, the probability of more than one atomic excitation is negligibly small.

In order to calculate $g^{(2)}(AS|n_S = 1)$, we must first calculate $\mathrm{Var}(N_s|n_S = 1)$ and $\langle N_s|n_S = 1\rangle$ as a function of measurable parameters such as $p\eta_S$ and η_S. To do this, we consider a simple model where we assume that a Stokes photon emitted from the atomic ensemble with probability p undergoes some loss (modeled by a beamsplitter with transmission η_S) and travels to a detector where we measure the probability of detecting a Stokes photon as $p\eta_S$. Using this model, we wish to calculate the variance

$\mathrm{Var}(N_s|n_S = 1)$ and expectation value $\langle N_s|n_S = 1\rangle$. To calculate these quantities, we need to calculate the probability $P(N_s|n_S)$ of exciting N_s atoms to the state $|s\rangle$ conditional on detecting n_S Stokes photons (where $n_S = 1$ in our specific case of single-photon conditioning). To do this, we employ the relation [24], $P(N_s|n_S) = P_J(N_s, n_S)/P(n_S)$, where $P_J(N_s, n_S)$ is the joint probability of exciting N_s atoms to state $|s\rangle$ and detecting n_S Stokes photons, and $P(n_S)$ is the overall probability of detecting n_S Stokes photons. We can solve for $P_J(N_s, n_S)$ via the analogous relation for $P(n_S|N_s)$, namely $P_J(N_s, n_S) = P(n_S|N_s) \cdot P(N_s)$. Since the atoms are excited via spontaneous Raman scattering, the distribution describing the probability of exciting N_s atoms to state $|s\rangle$ is a thermal distribution given by

$$P(N_s) = \langle N_s\rangle^{N_s}/(1 + \langle N_s\rangle)^{1+N_s}. \tag{4.11}$$

$P(n_S|N_s)$ is given by the binomial distribution resulting from the assumed linear loss, modeled by a beamsplitter with transmission η_S:

$$P(n_S|N_s) = \frac{N_s!}{n_S!(N_s - n_S)!}\eta_S^{n_S}(1 - \eta_S)^{N_s - n_S}. \tag{4.12}$$

Finally, $P(n_S)$ is found by just summing over N_s in the joint probability $P_J(N_s, n_S)$: $P(n_S) = \sum_{N_s=n_S}^{\infty} P_J(N_s, n_S)$. Putting all this together, we have the following expression for $P(N_s|n_S)$:

$$P(N_s|n_S) = P(n_S|N_s) \cdot P(N_s)/\sum_{N_s=n_S}^{\infty} P(n_S|N_s) \cdot P(N_s), \tag{4.13}$$

where the expressions for $P(N_s)$ and $P(n_S|N_s)$ are given in Eqs. (4.11) and (4.12), respectively. Using this expression for $P(N_s|n_S)$, we can then calculate $\langle N_s|n_S = 1\rangle$ and $\mathrm{Var}(N_s|n_S = 1) = \langle N_s^2|n_S = 1\rangle - \langle N_s|n_S = 1\rangle^2$ via the relations

$$\langle N_s|n_S = 1\rangle = \sum_{N_s=1}^{\infty} P(N_s|n_S = 1) \cdot N_s, \tag{4.14}$$

and

$$\langle N_s^2 | n_S = 1 \rangle = \sum_{N_s=1}^{\infty} P(N_s | n_S = 1) \cdot N_s^2. \tag{4.15}$$

The expressions for $\mathrm{Var}(N_s|n_S = 1)$ and $\langle N_s|n_S = 1\rangle$ can then be substituted into Eq. (4.10) to obtain an expression for $g^{(2)}(AS|n_S = 1)$ in terms of the quantities $\bar{b}_t$, $\bar{b}_p$, η_S, η_{AS}, and $\langle N_s\rangle$, the unconditional mean number of atoms excited to state $|s\rangle$. To compare with experimental measurements, we make the substitution $\langle N_s\rangle = p\eta_S/\eta_S$, valid in the regime of weak excitation ($p \ll 1$). This produces an expression for $g^{(2)}(AS|n_S = 1)$ that depends on the experimentally-measurable quantities $p\eta_S$ and η_S. A comparison of this theoretical model to the measured data is shown in Fig. 4.7. The agreement between theory and experiment is good, with any deviation from agreement most likely due to variation from point to point of η_S and η_{AS}, parameters that the theory assumes to be constant. The parameter values used in Fig. 4.7 (based on experimental measurements) are: $\bar{b}_t = 0.0021$, $\bar{b}_p = 0$, and $\eta_{AS} = 0.05$.

4.5 Conclusions

In this chapter, we utilized the nonclassical correlations between the Stokes and anti-Stokes photon numbers demonstrated in Chapter 3 to create nonclassical states of the anti-Stokes field via conditional detection of the Stokes field. First we demonstrated conditional generation of nonclassical anti-Stokes pulses by conditioning on $n_S = 2$ Stokes photons. These experiments used co-propagating write and retrieve lasers with orthogonal linear polarizations, multi-mode detection fibers, and an atomic ensemble temperature of $\approx 75°$C. Under these experimental conditions, we were unable to achieve conditional single-photon generation by conditioning on $n_S = 1$ Stokes

photon. A theoretical consideration of the conditions necessary for high-fidelity single-photon generation indicated that experimental improvements were necessary to reach the single-photon regime.

By reducing the temperature to $\approx 26°$C, and switching to a counter-propagating geometry with parallel linear polarizations for the write and retrieve lasers, and single-mode detections fibers, we were able to improve the signal-to-noise ratio enough to allow single-photon generation. With this improved experimental configuration, we demonstrated conditional single-photon generation via EIT-based retrieval of single-excitation atomic coherences, with experimentally measured $g^{(2)}(AS||n_S = 1)$ values as low as 0.3 ± 0.2. A theoretical treatment of the single-photon generation that included loss and background agreed well with the experimental observations, explaining the contribution of the remaining experimental imperfections to the non-ideal value of $g^{(2)} = 0.3$.

As discussed in the introduction, our single-photon source meets the necessary criteria for directionality and bandwidth. The directionality allows coupling into single-mode fibers, as performed in the experiments discussed in Chapter 5. The bandwidth of a few MHz (explicitly measured in Chapter 5) should eliminate any group-velocity dispersion during optical fiber propagation, and also allow storage into quantum memories with finite bandwidth (see Chapter 5). The long-coherence length implied by the narrow bandwidth should mean that the indistinguishability criterion is easily satisfied. Future Hong-Ou-Mandel-type [62] experiments will explicitly test the indistinguishability criterion.

Further improvements are necessary, however, regarding the on-demand emission,

emission rate, and fidelity of our source. Ideally, our single-photon source is on-demand: once a single Stokes photon has been detected, the single-photon anti-Stokes pulse can be retrieved from the atomic coherence at any desired time. In practice, the finite decoherence time ($\sim$ few μs) of the atomic coherence and the finite probability of successfully retrieving the atomic coherence ($\sim 10\%$) limit the on-demand reliability of our source. The rate of successful single-photon generation in our experiments is ~ 430 Hz (due to loss between the atomic ensemble and the detectors, the rate of successfully *detecting* a single photon is ~ 43 Hz). This rate is not fundamental, but for our experiments is limited by the finite retrieval efficiency, which limits the probability of successful generation, and the counting electronics and optical pumping duty cycle, both of which limit the repetition rate. These limitations can certainly be improved in future experiments. Finally, the fidelity is determined in our experiments by measuring the second-order correlation function, measured to be as low as $g^{(2)}(AS||n_S = 1) = 0.3 \pm 0.2$ in the experiments described in this chapter. This value deviates from the ideal value of $g^{(2)}(AS||n_S = 1) = 0$ primarily due to background noise resulting from the four-wave mixing process described in Section 3.3. This noise source is not fundamental, but a consequence of the specific atomic levels and optical polarizations used in the experiment. Recent experiments performed in our lab, in which we initially optically pumped to a specific Zeeman state ($F = 2, m_F = 2$) and used circularly polarized write and retrieve lasers, eliminated this four-wave mixing process, and yielded a measured value of $g^{(2)}(AS||n_S = 1) = 0.1 \pm 0.1$.

Chapter 5

EIT-Based Slowing, Storage, and Retrieval of Single-Photon Pulses using Atomic Ensembles

5.1 Introduction

In this chapter, we present an experimental demonstration of EIT in a novel, quantum regime using frequency-tunable single-photon pulses [35]. First we generate single photons using the single-photon source described in the previous chapter, and then we transmit them to a second ensemble using an optical fiber. In this second ensemble, we study EIT at the single-photon level. By investigating the transmission of these single photons through the second ensemble, we demonstrate that EIT propagation preserves the quantum nature of the single photons. In addition, we utilize EIT-based high-resolution spectroscopy to probe the spectral properties of

narrow-bandwidth single-photon pulses, observe single-photon-pulse time delay associated with reduced group velocity, and report the first evidence for the storage and retrieval of such pulses.

5.2 Single-Photon EIT

In this section, we consider the interaction of the anti-Stokes single-photon pulses generated by the source ensemble, with the optically dense target ensemble (see Figs. 4.2, and 4.3, and 4.6). The main idea behind our experimental implementation is to match the bandwidth and the central frequency of our single-photon source to the EIT transparency resonance of the target ensemble by tuning, respectively, the retrieve and the control laser intensities and frequencies [37]. The relative detuning between the retrieve and EIT control lasers is carefully controlled via acousto-optic modulators. Fig. 5.1(a) shows the conditional probability of detecting an anti-Stokes photon transmitted through the target ensemble, $\langle n\rangle(AS||n_S = 1)$, as a function of the two-photon detuning δ (EIT control laser frequency minus anti-Stokes frequency, minus the $|g\rangle - |s\rangle$ transition frequency). The clear resonance structure displays maximum transmission for $\delta = 0$. At this point, the central frequency of the single photons coincides with the EIT resonance window, resulting in a three-fold increase in transmission, which corresponds to 60% transmission of the incident pulse. The observed conditional probabilities can be used to quantify the correlations between the Stokes (S) and anti-Stokes (AS) photon numbers using the normalized correlation function $R \equiv g^{(2)}(S, AS)^2/g^{(2)}(S, S)\, g^{(2)}(AS, AS)$. Classical fields must obey the Cauchy-Schwartz inequality $\mathrm{R} \leq 1$; $\mathrm{R} > 1$ indicates nonclassical correlations [91]. For

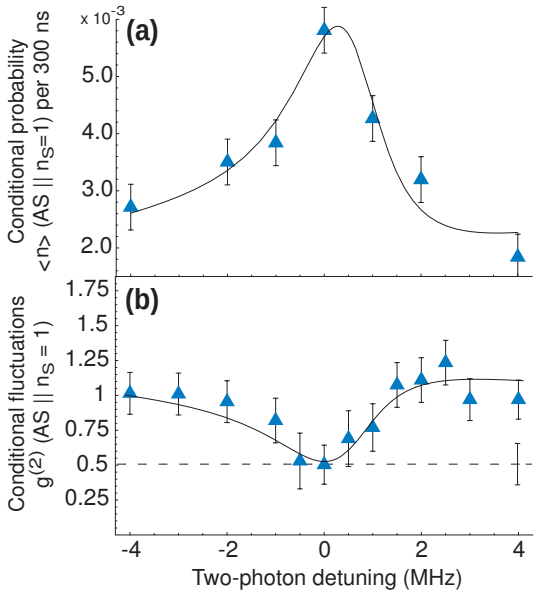

Figure 5.1: Observation of single-photon EIT. **(a)** Conditional probability (per 300 ns) of detecting an anti-Stokes photon transmitted through the target ensemble, $\langle n \rangle (AS||n_S = 1)$, versus the EIT two-photon detuning δ. Background (detection probability with write laser off) has been subtracted for transmission data in Figs. 5.1(a), 5.2(a), and 5.3(a). For incident pulses, $\langle n \rangle (AS||n_S = 1) \sim 0.01$. **(b)** Second-order correlation function of the anti-Stokes field conditioned on detecting one Stokes photon, $g^{(2)}(AS||n_S = 1)$, as a function of δ. Dotted line and error bar represent measured value with no target ensemble present. Statistical error bars (see Appendix B.1) are $\pm$ one standard deviation and represent averages of ~ 1 million anti-Stokes detection events, corresponding to total averaging times of ~ 2 hours per point. The solid line results from the theoretical model described in the text.

the data at $\delta = 0$, $\mathrm{R} = 1.85 \pm 0.12$, including all background and dark counts; as δ is tuned away form zero in either direction, R approaches the classical limit of unity.

For the data shown, δ is varied by varying the EIT control frequency. For these experiments, $p\eta_S \approx 0.06$, $\eta_S \approx 0.25$, and the source (target) ensemble temperature $\approx 26°\mathrm{C}$ ($30°\mathrm{C}$). The overall probability per trial to detect anti-Stokes photons is 6×10^{-3} for incident (target cell absent) photons and 3×10^{-3} for transmitted (target cell present, $\delta = 0$) photons.

Figure 5.1(b) shows the normalized photon-number fluctuations for the transmitted anti-Stokes field conditioned upon detection of $n_S = 1$ Stokes photon, $g^{(2)}(AS||n_S = 1)$, versus δ. We observe that $g^{(2)}(AS||n_S = 1)$ retains its nonclassical character upon transmission through the target ensemble only when near the center of the EIT transparency window. The minimum measured value of $g^{(2)}(AS||n_S = 1)$, occurring at $\delta = 0$ (0.50 ± 0.14) is essentially equal to the value measured by removing the target ensemble from the beam path (0.51 ± 0.15 for the displayed set of data). It is important to emphasize that the maximum of $\langle n \rangle (AS||n_S = 1)$ and the minimum $g^{(2)}(AS||n_S = 1)$ both occur at $\delta = 0$. As δ is tuned away from zero in either direction, $\langle n \rangle (AS||n_S = 1)$ decreases while $g^{(2)}(AS||n_S = 1)$ approaches classical limit of unity, indicating that the nonclassical nature of the anti-Stokes pulse is preserved only within the EIT transparency window [2]. The classical limit is also observed when the EIT control field is turned off. Likewise, $g^{(2)}(AS)$ obtained *without conditioning* exhibits no structure as a function of δ and again yields the classical limit of unity. Finally, we note that the photon-correlation data display a noise-enhancement feature on the high-frequency side of the EIT resonance. Preliminary calculations suggest that this enhancement is related to the presence of spectrally broad two-photon events, but further investigation is needed.

The narrow resonances observed in transmission and photon-correlation data set an upper bound to the bandwidth (of order MHz) of the single-photon pulses generated in our experiments. Photons with bandwidths larger than the target-ensemble EIT transmission bandwidth would be absorbed in the target ensemble. The significant transmission (60%) of the incident field and nonclassical $g^{(2)}$ values on EIT

resonance indicate that the single-photon bandwidth is less than or equal to the width of the EIT transmission window. These narrow bandwidths result because we produce the single photons in the source ensemble by retrieving an atomic coherence onto a dark-state polariton that propagates through the ensemble under EIT conditions. Therefore, the single photons should have bandwidths equal to the EIT transmission bandwidth in the source ensemble (of order MHz), as we observe.

These observations clearly demonstrate that EIT transmission preserves the nonclassical statistics of the anti-Stokes pulses. To analyze these observations, we consider a theoretical model that describes the propagation of single photons of finite bandwidth and purity (i.e., finite probability of two-photon events) in an optically dense, coherently driven medium of three-level atoms. Included in this model is Doppler broadening, realistic detunings (resulting in an asymmetric spectrum), finite decay of the $|g\rangle - |s\rangle$ coherence, and spectrally broad noise associated with two-photon events. The parameter values used in the model (retrieve laser Rabi frequency = 35 MHz, retrieve laser detuning = +400 MHz, anti-Stokes background = 0.003 photons per pulse, optical depth = 2.5, single-photon bandwidth = 0.7 MHz, $|g\rangle - |s\rangle$ coherence decay = 0.02 MHz), are similar to experimental conditions. As shown in Fig. 5.1, the theoretical predictions are in good agreement with experimental observations.

5.3 EIT-based Slowing, Storage, and Retrieval of Single Photons

One application of EIT involves the controllable delay of optical pulses by slowing their group velocity [56, 66] and stopping their propagation [79, 103, 80, 42]. Figures 5.2 and 5.3 present an experimental realization of such controllable delay and storage for single-photon pulses. For these measurements, the single-photon anti-Stokes pulses were tuned to the center of the EIT transmission window ($\delta = 0$); the retrieve laser was turned on for approximately 150 ns, generating anti-Stokes pulses of corresponding duration. Time-resolved measurements shown in Fig. 5.2(a) reveal substantial delay, relative to free-space propagation, of the conditionally generated anti-Stokes pulses upon transmission through the EIT medium. Measurements are shown for three cases: vacuum propagation (target ensemble absent and EIT control laser off), target ensemble at 34.6°C with EIT control field on, and target ensemble at 47°C with EIT control field on. Temperature is used to adjust the atomic density, which is inversely related to the group velocity (see Eq. (1.6)).The solid lines in Fig. 5.2(a) represent a theoretical prediction for EIT-propagation in a Doppler-broadened medium [3].

As shown in Fig. 5.2(b), we observe delays up to 45 ns in our 4.5 cm-long ensemble, corresponding to single photon velocities of about 10^3 km/s (~ 0.003 times the speed of light in vacuum). In Fig. 5.2(a), the observed delay of 40 ns corresponds to a substantial fractional delay of about 30% when compared to the 140 ns full-width at half-maximum of the reference pulse .

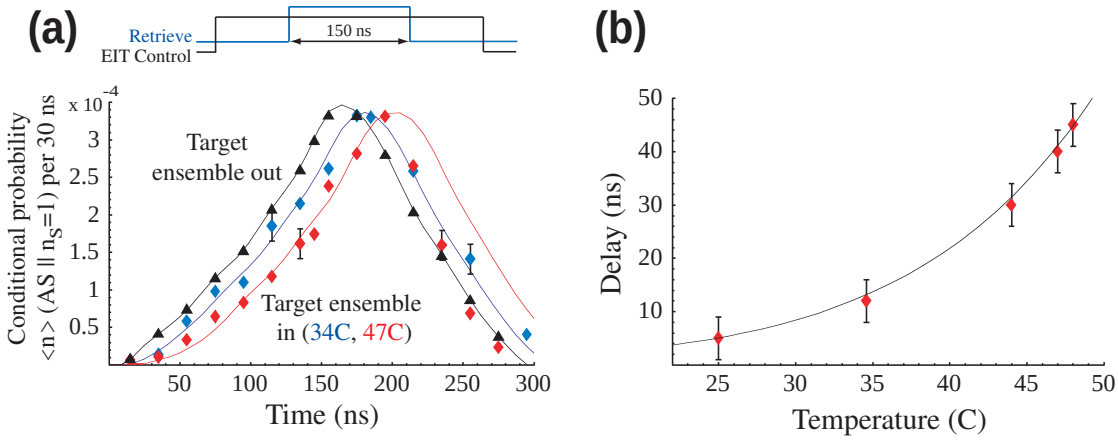

Figure 5.2: Measurement of single-photon pulse delay. **(a)** Conditional probability (per 30 ns) of detecting an anti-Stokes photon transmitted through the target ensemble. Target ensemble absent (black triangles); target ensemble present at 34.6°C (blue diamonds) and 47°C (red diamonds). Delayed pulse at 34.6°C (47°C) is scaled by the factor 1.34 (2.14). Solid lines represent theoretical calculations for EIT propagation in a Doppler-broadened medium. **(b)** Delay, relative to free-space propagation, of single-photon anti-Stokes pulses, as a function of target-ensemble temperature. Solid line is a theoretical prediction for an EIT control field Rabi frequency of 35 MHz.

Fig. 5.3(a) demonstrates that a fraction of the incoming single-photon pulses can be stored by dynamically reducing single-photon group velocity to zero. This is accomplished by turning off the EIT control laser as the anti-Stokes pulse propagates in the target ensemble. At speeds of $c/300$, about 40 ns of the 140 ns full-width at half-maximum single-photon pulse fits inside the target ensemble. The first peak in Fig. 5.3(a) is the front edge of the single-photon pulse leaking out of the ensemble. When most of the pulse is inside the ensemble, the EIT control field is turned off, storing the pulse in the $|g\rangle - |s\rangle$ atomic coherence. The stored fraction is released when the control laser is turned back on [79, 103, 80].

Figure 5.3(b) shows the conditional storage and retrieval probability as a function of storage time. Storage and retrieval of up to 10% of the incoming pulse was

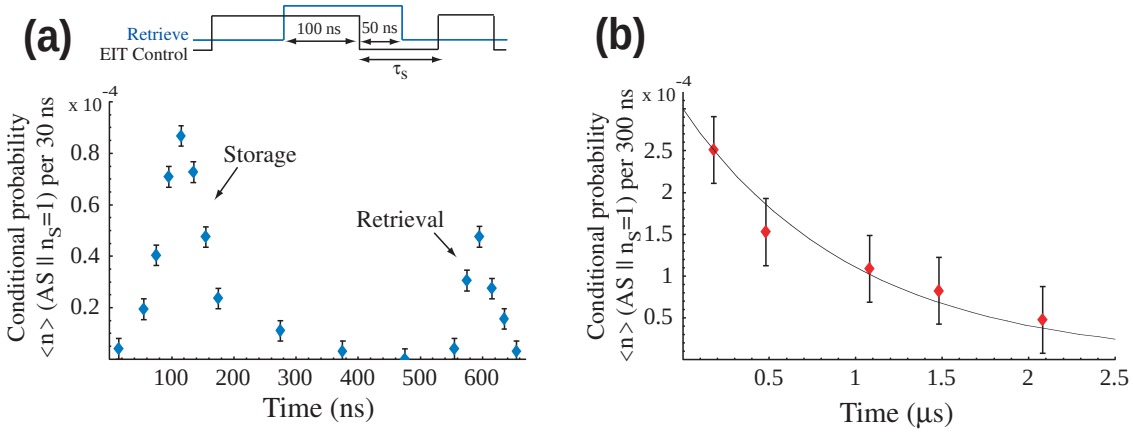

Figure 5.3: Measurement of single-photon storage. **(a)** Storage and retrieval of a single-photon anti-Stokes pulse. EIT control laser is turned off 100 ns after the retrieval from the source ensemble begins; after waiting for a storage time of τ_s = 460 ns, the EIT control laser is turned back on, resulting in the retrieved pulse centered at 600 ns. Target ensemble temperature $\approx 47°$C. **(b)** Conditional probability (per 300 ns) of detecting an anti-Stokes photon retrieved from the target ensemble after storage interval τ_s. $\langle n \rangle (AS||n_S = 1) = 0.003$ for the incident pulse (measured with target ensemble absent). For short storage times, the overall probability per trial to detect incident (retrieved) anti-Stokes photons is $\sim 1.5 \times 10^{-3}$ (1.5×10^{-4}). Decay of probability is fit by an exponential with a 1/e characteristic time of about 1 μs; this is consistent with diffusion of atoms from the detection volume.

observed at short storage times; retrieved pulses were observed for times up to a few microseconds, limited by atomic diffusion in the target ensemble (see Appendix A.1 for details). Even with these limited efficiencies, the retrieved pulses preserve some nonclassical features after considerable storage intervals. For example, for a storage time of 0.5 μs, we deduce R = 1.08 $\pm$ 0.01 > 1.

The storage and retrieval efficiency could be improved by, for example, increasing the optical depth or utilizing an optical cavity with modest finesse [12]. Recent theoretical work on the optimization of storage and retrieval efficiency suggests that the efficiency could be significantly improved by appropriate temporal shaping of the EIT control field used to store and retrieve [50]. In addition, the storage times could be

considerably extended by reducing the effect of atomic diffusion, either by expanding the detection-mode diameter, working with ultra-cold atoms in dipole traps or optical lattices, or using a doped solid [80]. A factor of ten increase in the detection-mode diameter should extend storage times to a fraction of millisecond [103].

5.4 Conclusions

The results presented in this chapter were the first demonstration and investigation of EIT propagation and storage at the single-photon level. First we transmitted conditional single-photons generated via EIT-based retrieval of single-excitation atomic coherences (see Chapter 4) to a second atomic ensemble using an optical fiber. In the second ensemble, we demonstrated that EIT propagation preserved the nonclassical photon statistics of the single-photon pulses. Finally, we demonstrated EIT-based slowing, storage, and retrieval of single-photon pulses, and demonstrated that the nonclassical nature of the correlations between the Stokes and anti-Stokes photon numbers are preserved under EIT storage and retrieval.

These results demonstrate that EIT represents a very effective technique for generation and controlled propagation of narrow-bandwidth single-photon light pulses in optically dense atomic ensembles. Applications of these techniques to quantum-optical processes involving simultaneous control over temporal, spectral, and quantum-statistical properties of single photons are possible [20, 34, 112, 1]. For example, these techniques can be applied to the realization of quantum networks [20] and the DLCZ protocol for long-distance quantum communication [34]. At the same time, coherent nonlinear-optical interactions at the single-photon level have been proposed by

combining these techniques with resonantly enhanced atomic nonlinearities [1].

Chapter 6

Conclusion

As discussed in the introduction, since the proposal in 2001 of the DLCZ scheme for long-distance quantum communication with atomic ensembles and linear optics, experimental progress toward realization of the protocol has been rapid. From 2003 to the time of this writing in 2006, experiments have provided proof-of-principle demonstration of many elements necessary for the realization of the DLCZ protocol, including conditional single-photon generation using an atomic ensemble [64, 30, 35, 26], measurement-induced entanglement between two atomic ensembles [29], and atomic-ensemble based quantum memory using dynamic EIT [35, 26]. This thesis has focused on the contribution of our group at Harvard to this effort, including the demonstration of nonclassically correlated photon pairs [118], demonstration of EIT-based shaping of few-photon pulses [37], the generation of narrow-bandwidth single-photon pulses [35], and the EIT-based slowing, storage, and retrieval of single-photon pulses [35].

This works, together with developments in other laboratories, have demonstrated the principle components of the DLCZ scheme. The field now enters a new stage,

where high-performance, robust operation is central. In order to ultimately find real-world applicability, the efficiencies, backgrounds, and fidelities of these experiments must be improved enough to allow high-fidelity entangled pairs to be generated at large distances. In addition, the experimental implementation must be sufficiently robust to allow scaling to tens or hundreds of nodes.

One important figure of merit in the DLCZ scheme is the ratio of the quantum memory time to the time needed for a typical operation. The polynomial scaling of time with distance in the DLCZ scheme depends on the fact that successfully generated entanglement between two nodes will be preserved by the quantum memory while one attempts (and sometimes fails) to generate entanglement between two other nodes. If the quantum memory decoheres before entanglement can be successfully generated between other nodes, entanglement cannot be extended via entanglement swapping, and the scaling of time with distance will no longer be polynomial.

The decoherence times measured in our experiments in room temperature atomic ensembles were on the order of a few microseconds, limited by the diffusion time out of the detection mode volume. This should be compared with the typical period of our experiment ($\sim 1/72\,\mathrm{kHz} = 14\,\mu\mathrm{s}$), divided by the probability of successful atomic excitation per repetition (~ 0.06), giving a typical "operation time" of $\sim 230\,\mu\mathrm{s}$. Clearly, the ratio of decoherence time to operation time needs to be greatly improved. Increasing the decoherence time from their current values of microseconds is fairly straightforward; by sufficiently increasing the size of the detection mode to increase the diffusion time, the primary cause of decoherence will become collisions with other rubidium atoms. In this case, the decoherence times will be on the order of tens

of milliseconds. By optimizing the counting electronics and optical pumping cycle, and increasing the transmission on the Stokes (heralding) channel to allow greater success probability, it should be possible to decrease the "operation time" to a few microseconds. Therefore, it is feasible that improvements to the current experimental setup will lead to decoherence-time-to-operation-time ratios of $\sim 10^3$.

An alternative method for increasing this ratio is to use a system with longer decoherence times, such as a dipole trap or a solid-state material. Using a solid-state material also has the potential to improve the scalability of the system. For example, praseodymium-doped Y_2SiO_5 is a solid-state material that has already been shown to have decoherence times of tens of seconds [46, 47], and was recently used to store light via EIT for up to ten seconds [80]. In principle, the solid-state nature of the material could greatly improve the scalability, but the need for helium cryogenics will need to be overcome first.

In addition to these experimental challenges, theoretical challenges also remain. For example, the figures of merit needed to achieve long-distance quantum communication in practical systems must be defined. In addition, the DLCZ protocol is not necessarily the ultimate scheme - theoretical challenges certainly remain in developing more efficient and robust protocols.

The next few years promise to be a very interesting time, as we see whether these challenges can be sufficiently overcome to allow practical application of these ideas. In addition, the demonstration of EIT at the single-photon level has the potential to open up a new era in nonlinear optics, in which controlled nonlinear interactions between individual photons [85, 86, 1] are finally realized.

Appendix A

Appendices to Chapter 2

A.1 Properties of Rubidium 87

This appendix lists properties of ^{87}Rb relevant to our experiments. Table A.1 displays relevant physical properties of ^{87}Rb .

Atomic Number	37
Neutrons and Protons	87
Relative Natural Abundance	27.83(2)%
Atomic Mass	$1.443\,160\,60(11) \times 10^{-25}$ kg
Density at 25°C	1.53 g/cm^3
Melting Point	39.31 °C
Boiling Point	688 °C
Vapor Pressure at 25°C	3.0×10^{-7} Torr
Nuclear Spin	3/2

Table A.1: ^{87}Rb physical properties. All values are taken from Ref. [115].

In our experiments, we only excite the D_1 line ($5^2S_{1/2} \rightarrow 5^2P_{1/2}$) of ^{87}Rb. Fig. A.1 shows the full atomic level structure for the D_1 line. Due to interaction with the

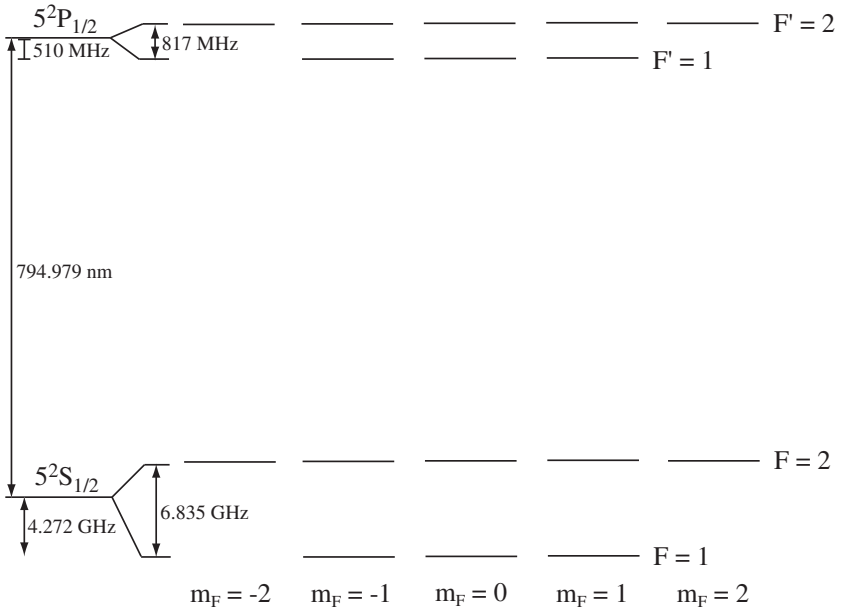

Figure A.1: Atomic-level structure for the D_1 line ($5^2S_{1/2} \rightarrow 5^2P_{1/2}$) of ^{87}Rb . Numbers are taken from Ref. [115].

nuclear spin $I = 3/2$, the $J = 1/2$ levels for both the ground state ($L = 0$, i.e. S) and the excited state ($L = 1$, i.e. P) each have two hyperfine sublevels with total angular momentum $F = 1$ and $F = 2$. For $S_{1/2}$ ($P_{1/2}$) these are designated by $F(F')$.

Table A.2 displays relevant optical properties for the D_1 line ($5^2S_{1/2} \rightarrow 5^2P_{1/2}$) of ^{87}Rb .

Frequency	$2\pi \cdot 377.107\,463\,5(4)$ THz
Wavelength (Vacuum)	794.978 850 9(8) nm
Wavelength (Air)	794.765 69 nm
Wave Number (Vacuum)	12 578.950 985(13) cm^{-1}
Lifetime	27.70(4) ns
Natural Line Width	$2\pi \cdot 5.746(8)$ MHz

Table A.2: Optical properties for the D_1 line ($5^2S_{1/2} \rightarrow 5^2P_{1/2}$) of ^{87}Rb . All values are taken from Ref. [115].

In all of our experiments, we control the atomic density by changing the temperature of the ensemble. A plot of the number density of ^{87}Rb as a function of temperature is shown in Fig. A.2.

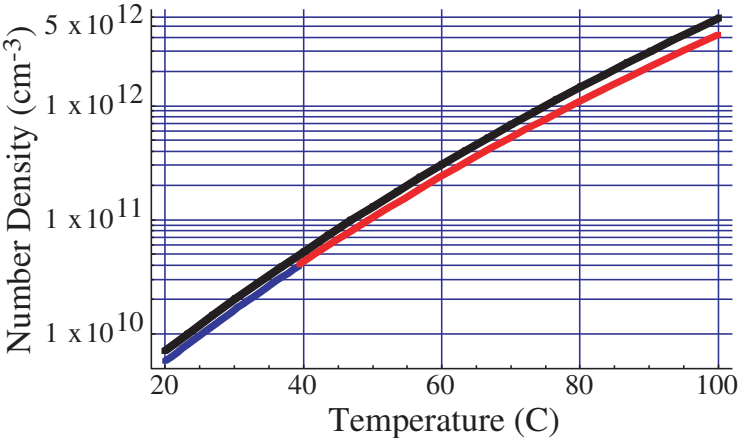

Figure A.2: Calculated number density of ^{87}Rb (assuming an isotopically pure ensemble) as a function of temperature. Black line calculated using the pressure-temperature relation from Ref. [120], and the ideal gas law. Blue and red lines calculated using the ideal gas law and the pressure-temperature relation from Ref. [115]. Blue line used relation for the solid phase, red for the liquid phase (melting point of ^{87}Rb is 39.31°C.)

All of the experiments in this thesis utilize isotopically pure ^{87}Rb vapor cells filled with Ne buffer gas to slow the diffusion of ^{87}Rb atoms out of the detection-mode volume (the volume inside the ensemble defined by our detection fibers and lenses). For the conditions in our experiments, the decoherence of the ground-state $|g\rangle - |s\rangle$ coherence is due to diffusion out of the detection volume. Therefore, the buffer gas serves to slow the ground-state decoherence rate by slowing the diffusion out of the detection mode volume. The ground-state $|g\rangle - |s\rangle$ coherence itself is not greatly affected by collisions with buffer-gas atoms [53, 121].[1]

[1]The excited states $|e\rangle = |^2 5P_{1/2}, F' = 1, 2\rangle$ are affected to a greater extent by collisions with

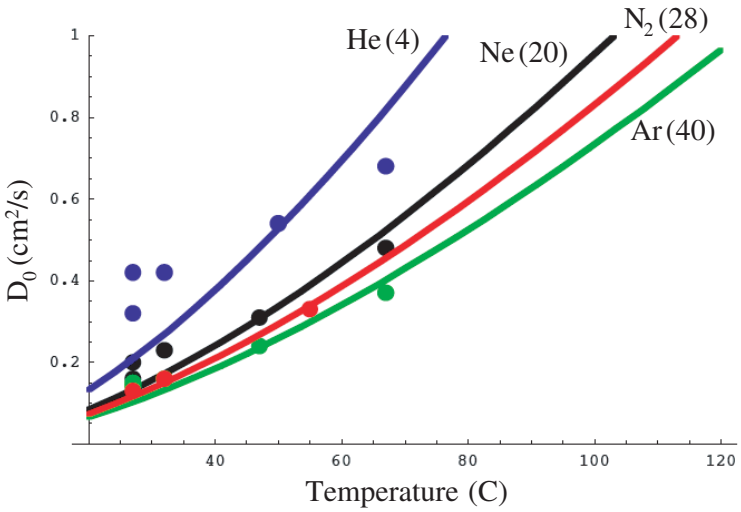

Figure A.3: Diffusion constant D_0 as a function of temperature for four buffer-gas atoms: He (blue), Ne (black), N_2 (red), and Ar (green). Mass number is shown in parentheses. Points represent experimental measurements taken from Ref. [119]. Solid lines represent fits to the data points scaling as $T^{3/2}$, where T is temperature.

In our case of a cylindrical geometry with transverse diameter of a few hundred micrometers, and a length of $\sim 5\,\mathrm{cm}$, we are interested in how long it takes an atom to diffuse out of the transverse cross-section (i.e., the detection mode volume). In two dimensions, the standard deviation in position σ_r (defined such that $\sim 32\%$ of atoms have moved a distance greater than σ_r) is given by

$$\sigma_r = 2\sqrt{2}\sqrt{Dt}, \tag{A.1}$$

where t is time, and the diffusion constant D is given by

$$D = D_0 \left(\frac{P_0}{P}\right), \tag{A.2}$$

buffer gas atoms, resulting in significant broadening of the excited-state linewidths [53, 68]. Qualitatively, the greater effect on the excited states $|e\rangle = |^2 5P_{1/2}, F' = 1, 2\rangle$ compared to the ground states $|g\rangle = |^2 5S_{1/2}, F = 1\rangle$ and $|s\rangle = |^2 5S_{1/2}, F = 2\rangle$ can be understood by the different geometry of $|e\rangle$ compared to $|g\rangle$ and $|s\rangle$ in relation to the $n = 4$ electrons of rubidium.

where $P_0 = 760\,\text{Torr}$, P is the buffer-gas pressure in Torr, and D_0 is a constant with units of cm^2/s that can be assumed to be proportional to $T^{3/2}$, where T is temperature [119]. Fig. A.3 shows a plot of D_0 for four types of buffer gas: He, N_2, Ne, and Ar. The data points represent measured values. The solid lines represents fits to these data points scaling as $T^{3/2}$.

Using these values of D_0, we can calculate σ_r for any experimental conditions. Fig. A.4(a) shows σ_r as a function of time for four different experimental conditions: those of Ref. [118] (Chapter 2), Ref. [37] (Chapters 3 and Section 4.2.2), the source ensemble in Ref. [35] (Section 4.4 and Chapter 5), and the target ensemble in Ref. [35] (Chapter 5). These experiments had (buffer-gas pressure, detection-mode diameter, temperature) of: (4 Torr, 500 μm, 85°C), (6 Torr, 400 μm, 75°C), (7 Torr, 200 μm, 26°C), and (8 Torr, 200 μm, 47°C), respectively. The target ensemble temperature of 47°C was the temperature used in the storage and retrieval experiments shown in Fig. 5.3. The horizontal solid lines on the plot correspond to the detection-mode diameter used for that experiment. The time value at which this line intersects the given curve is the predicted diffusion time for that experiment, corresponding to the time at which $\sim 1/e$ of the original atoms remain in the detection-mode volume. Fig. A.4(b) shows the same data, but this time plots the time required for $\sigma_r/2$ to equal to the detection-mode radius as a function of buffer-gas pressure. This condition corresponds to $\sim 62\%$ of the atoms moving outside the detection-mode volume, with $38\% \sim 1/e$ of the atoms still within the detection mode. The vertical solid lines on the plot correspond to the buffer-gas pressure used for that experiment. The time value at which this line intersects the given curve is the predicted diffusion time for

that experiment, corresponding to the time at which $\sim 1/e$ of the original atoms remain in the detection-mode volume. This time (the same time as predicted by Fig. A.4(a)) should approximately equal the $1/e$ decoherence time of the $|g\rangle - |s\rangle$ transition. Indeed, the times predicted by Fig. A.4 are in good agreement with the experimental observations presented in Chapters 2 - 5.

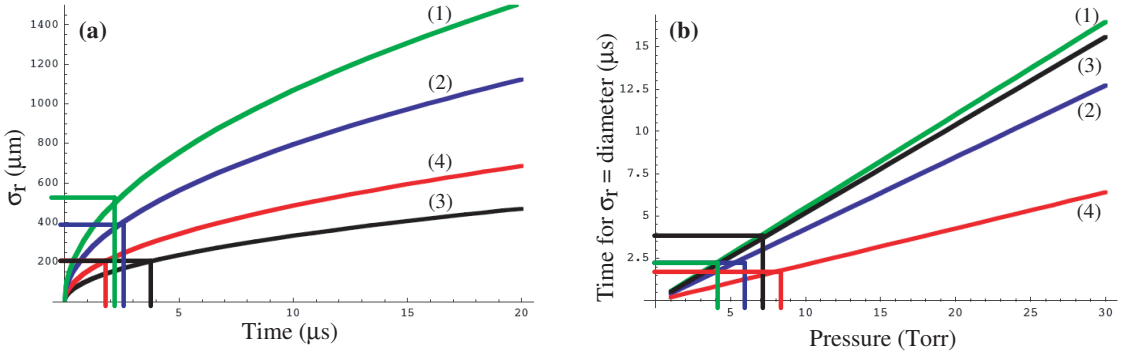

Figure A.4: Predicted diffusion times for various experimental conditions. Times are estimated for the experimental conditions of: Ref. [118] (green, labeled (1)), Ref. [37] (blue, (2)), the source ensemble of Ref. [35] (black, (3)), and the target ensemble of Ref. [35] (red, (4)). See text for details. **(a)** Standard deviation in position due to diffusion, σ_r, as a function of time. **(b)** Time required for $\sigma_r/2$ to equal the detection-mode radius, as a function of buffer-gas pressure.

To understand many effects of buffer-gas atoms, it is important to know the rate at which a given rubidium atom collides with buffer-gas atoms. The mean collision rate is τ_c^{-1}, where the mean time between collisions τ_c is given by (see Ref. [119])

$$\tau_c = \frac{M D_0}{k_B T} \frac{P_0}{P}, \tag{A.3}$$

where M is the rubidium atomic mass, D_0 is the diffusion constant shown in Fig. A.3, k_B is Boltzmann's constant, T is temperature, P_0 is 760 Torr, and P is pressure in Torr. For parameters corresponding to the experiments described in this thesis

($\sim$ 7 Torr of Ne buffer gas at temperatures between 20°C - 70°C), τ_c^{-1} is on the order of a few MHz, approximately equal to the natural linewidth of the excited state $\left|^2 5P_{1/2}\right\rangle$ (see Table A.2).

A.2 Low-Noise Photodetector Details

In this appendix, we provide a detailed description of the low-noise photodetectors constructed for the experiments described in Chapter 2. We designed and constructed the detectors ourselves, with the primary requirements being that they have large gain, low noise, and that the two detectors be well matched in terms of their noise properties and gain versus frequency behavior [59, 51, 7].

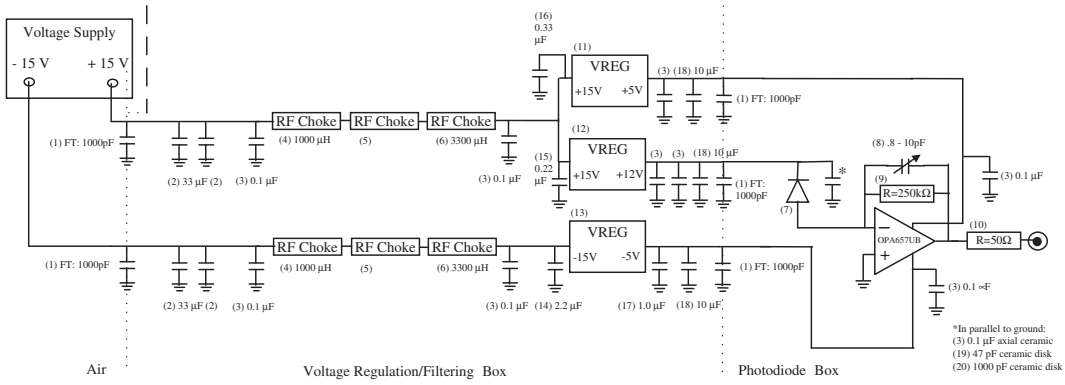

Figure A.5: Schematic of the low-noise photodetector circuit. Details of the labeled parts are provided in Table A.3.

Fig. A.5 shows a schematic of the photodetector. The detectors consists of two separate shielded boxes: one containing the voltage filtering, and the other containing the photodiode and transimpedance amplifier. The purpose of the voltage filtering box is to filter out and reduce noise present on the input voltages. Any noise will increase the overall noise floor of the detector, making it difficult to obtain the sensitivity required to observe squeezing. It is very important to place the voltage filtering and photodiode transimpedance circuit in different shielded boxes in order to avoid any coupling between the two.

The principle of operation of the detector is fairly straightforward. A photodiode

is reverse biased with a voltage of 12 V, such that the current generated by the photodiode is linearly proportional to the incident optical intensity. The photodiode is connected to an operational amplifier and resistor in a so-called transimpedance configuration such that this current is converted into an output voltage. For the photodetector shown in Fig. A.5, the 250 kΩ transimpedance resistor, combined with the current-voltage relation V = IR, means that the output voltage is equal to the photodiode current multiplied by $2.5 \cdot 10^5$. This configuration converts the photodiode current to an output voltage with the resistor value acting as a gain. The capacitor connected in parallel with the transimpedance resistor is used to "roll-off", that is decrease, the gain at higher frequencies. This avoids nonlinearities associated with phase shifts at higher frequencies [63, 59, 51].

Using the schematic shown in Fig. A.5, we constructed two photodetectors used in the experiments described in Chapter 2. For these detectors, we measured a constant gain as a function of frequency from 200 kHz (frequencies lower than this are obscured by technical 1/f noise [45]) out to the "roll-off" frequency of ~ 5 MHz. We measured the gain versus frequency response of the detectors to be the same to within a few parts in 10^4; this precise matching was achieved by using a laser-matched pair of resistors for the transimpedance resistors of the two detectors. The saturation of the detectors occurs at an optical power of $\sim 14\,\mu$W, limited by the maximum voltage output of the operational amplifier. The dark noise of the each detector was measured to be $30\,\mathrm{nV}/\sqrt{\mathrm{Hz}}$.

Table A.3 lists the parts used in the photodiode construction, including the label used for the part in Fig. A.5 and the quantity required to build one photodetector.

Label	Description	Quantity
1	1000 pF feedthrough capacitor, Newark part 90F2268	5
2	33 μF tantalum capacitor	4
3	0.1 μF capacitor, axial ceramic	10
4	1000 μH RF choke, DigiKey part M9251-ND	2
5	RF choke, DigiKey part FB20010-3B	2
6	3300 μH RF choke, DigiKey, M9257-ND	2
7	PIN Photodiode, Hamamatsu, S3883	1
8	0.7-20 pF surface mount trimmer cap, DigiKey, 2807S020-ND	1
9	250 kΩ surface mount resistor (1 of matched pair)	1
10	50 Ω resistor	1
11	+5V Voltage Regulator, Fairchild, LM7805C	1
12	+12V Voltage Regulator, National Semiconductor, LM7812	1
13	-5V Voltage Regulator, Fairchild, LM7905C	1
14	2.2 μF tantalum capacitor	1
15	0.22 μF metal poly (ideally tantalum) capacitor	1
16	0.33 μF metal poly (ideally tantalum) capacitor	1
17	1.0 μF tantalum capacitor	1
18	10 μF tantalum capacitor	3
19	47 pF ceramic disk capacitor	1
20	1000 pF ceramic disk capacitor	1

Table A.3: Photodetector parts list.

Note that it is important to use matched resistors in the two detectors for resistor (9) in order to guarantee similar behavior in gain versus frequency for the two detectors.

Fig. A.6 is a measurement of the standard quantum limit (see Section 2.3.1) of laser light, to verify that the detectors are well matched. The measurement also determines the range of incident optical powers for which we can measure the standard quantum limit. For very large optical power, the detectors will saturate, while at very low power, the electrical output of the detector will eventually be overwhelmed by the dark noise of the detectors.

To perform this test, we directed a laser beam incident onto a 50-50 beamsplitter,

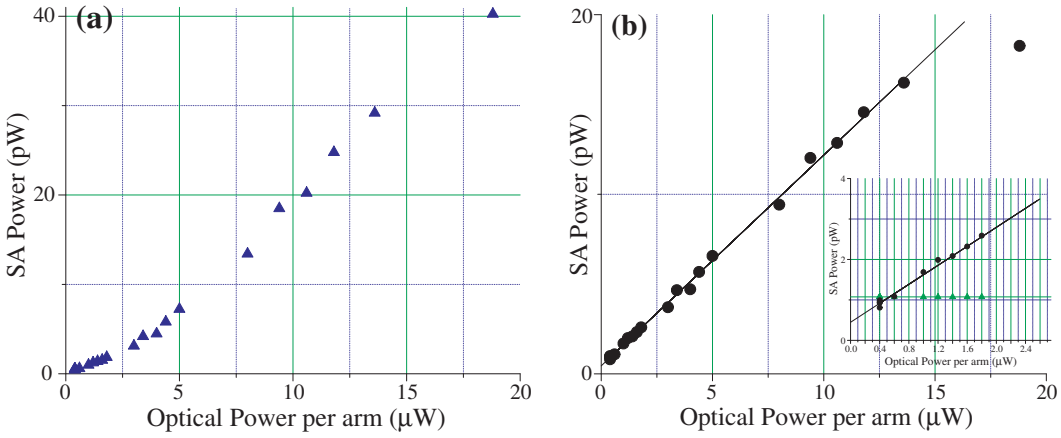

Figure A.6: Measurement of the standard quantum limit and noise floor. **(a)** Electronic power recorded by the spectrum analyzer (SA) at photodetector 1 (PD1) as a function of the optical power incident on PD1. Dark noise from PD1 and spectrum analyzer is included. **(b)** Electronic power (black circles) recorded by the spectrum analyzer (SA) of the signal formed by subtracting the electronic signals from PD1 and PD2, as a function of the optical power incident on each photodetector. A 50-50 beamsplitter splits an incident laser field into two equal-intensity beams, which propagate to PD1 and PD2 respectively. A constant value representing the measured dark noise from PD1, PD2, and the spectrum analyzer has been subtracted. Solid black line is a linear fit to the data. **(inset)** Black line and squares are the same as in (b). Green triangles represent the total dark noise of the system, including noise from the spectrum analyzer, PD1, and PD2. All measurements were averages taken over the bandwidth 200 kHz - 300 kHz

with one photodetector in each arm of the output, PD1 and PD2, respectively. The electrical outputs of the photodetectors are then directed to a spectrum analyzer, which measures the electrical power in a given frequency bandwidth, in units of V^2/Hz (over a $50\,\Omega$ resistance), for example [7]. By averaging the results over a given bandwidth and multiplying by the width of the band, this measurement essentially gives the average electrical power in that frequency band, equivalent to a measurement of the variance of the incident optical power. In this way, we can test if we observe the standard quantum limit of noise by verifying that the electrical power measured

by the spectrum analyzer (equivalent to the variance of the optical power incident on the detectors) scales linearly with increasing average incident optical power (see Appendix A.3 and Section 2.3.1).

Fig. A.6(a) shows the measured electrical power averaged over the bandwidth 200 kHz - 300 kHz, as a function of average incident optical power for PD1. We observe the electrical power does not scale linearly with average optical power, but also contains some quadratic dependence, and therefore contains extra noise in addition to the standard quantum limit. This is not surprising since we do not expect the incident laser beam to be at the standard quantum limit. Extra classical noise may be present for many reasons, such fluctuating laser-diode current, temperature, or frequency, all of which can affect the output power of the laser diode.

This classical noise can be removed by subtracting the electrical output of the two photodetectors PD1 and PD2. Any extra classical noise from the laser itself will be identical for the two beamsplitter arms, and will perfectly cancel, assuming well matched photodetector circuits. The only noise left will be due to the "partition noise" that arises from the random nature of photons at the beamsplitter [109]. This partition noise is equal to the standard quantum limit.

Fig. A.6(b) shows the measured electrical power averaged over the bandwidth 200 kHz - 300 kHz, as a function of average incident optical power in one arm of the beamsplitter, for the signal formed by subtracting the electrical outputs of PD1 and PD2. In this case, we see that the electrical power does scale linearly with average optical power, indicating that the detectors are well matched and that any classical noise in addition to the standard quantum limit is subtracted. The sub-linear behavior

that occurs for optical powers greater than $\sim 14\mu$W is simply due to saturation of the detectors. The inset to Fig. A.6(b) zooms in on the low-power values, and also plots the measured dark noise floor, which includes the dark noise from the spectrum analyzer and both photodetectors. This dark floor is approximately equal to 1 pW and crosses the measured standard quantum limit at an incident optical power per detector of $0.4\,\mu$W. This value represents the incident optical power below which we cannot measure the standard quantum limit. The upper limit of detection is given by the detector saturation at$\sim 14\mu$W.

A.3 Photon-Number Statistics

A useful method for characterizing a photon field is by quantifying the field's photon-number statistics, by which we mean the probability $P(n)$ of detecting n photons in a given photon-number measurement of the field.

First we consider the case of a photon field with thermal statistics. In thermal equilibrium at temperature T, the probability $P(n)$ that the radiation mode at frequency ω is thermally excited to its nth excited state is given by

$$P(n) = e^{(-n\hbar\omega/k_BT)} / \sum_n e^{(-n\hbar\omega/k_BT)}, \tag{A.4}$$

where $\hbar$ is Planck's constant, and k_B is Boltzman's constant. In this case, the mean and variance of the photon-number, are given by the expressions

$$\langle n \rangle = \sum_n nP(n) = 1/(e^{(\hbar\omega/k_BT)} - 1) \tag{A.5}$$

and

$$\mathrm{Var}(n) = \sum_n (n - \langle n \rangle)^2 P(n) = \langle n^2 \rangle - \langle n \rangle^2 = \langle n \rangle^2 + \langle n \rangle, \tag{A.6}$$

respectively [81]. Eq. (A.5) is also referred to as the Bose-Einstein distribution [109]. From these expressions, we see that $P(n)$ can be expressed in terms of the mean photon number $\langle n \rangle$ as

$$P(n) = \langle n \rangle^n / (1 + \langle n \rangle)^{1+n}. \tag{A.7}$$

Thermal, or Bose-Einstein, photon-number statistics accurately describe the photon-number fluctuations associated with spontaneous scattering of laser light by atoms [108].

Next we consider the case of Poisson photon-number statistics, where the proba-

bility $P(n)$ of detecting n photons is given by

$$P(n) = e^{-|\alpha|^2} \frac{|\alpha|^{2n}}{n!}, \tag{A.8}$$

where α is a parameter related to the mean photon number. In this case, the mean and variance are given by the expressions

$$\langle n \rangle = \sum_n nP(n) = |\alpha|^2 \tag{A.9}$$

and

$$\mathrm{Var}(n) = \sum_n (n - \langle n \rangle)^2 P(n) = \langle n \rangle, \tag{A.10}$$

respectively [81]. $P(n)$ can be expressed in terms of the mean photon number $\langle n \rangle$ as

$$P(n) = e^{-\langle n \rangle} \frac{\langle n \rangle^n}{n!}. \tag{A.11}$$

Poisson statistics represent the fluctuations possessed by a coherent state, the quantum-mechanical state that most closely resembles a classical electromagnetic wave. The coherent state accurately describes the state of an ideal single-mode laser, and in the limit of strong excitation, the electric-field variation of a coherent state approaches that of a classical wave of stable amplitude and fixed phase [81]. Mathematically, the coherent state $|\alpha\rangle$ with $\langle n \rangle = |\alpha|^2$ is given by

$$|\alpha\rangle = e^{-|\alpha|^2/2} \sum_{n=0}^{\infty} \frac{\alpha^n}{\sqrt{n!}} \, |n\rangle \,, \tag{A.12}$$

and is the eigenstate of the annihilation operator $\hat{a}$, since $\hat{a} \, |\alpha\rangle = \alpha \, |\alpha\rangle$. Physically, the radiation emitted by a classical current distribution is, in fact, a coherent state [113].

Most relevant to the results discussed in this thesis, the photon-number fluctuations of a coherent state are the minimum achievable by a classical electromagnetic field, and therefore represent the benchmark for quantum-mechanical behavior

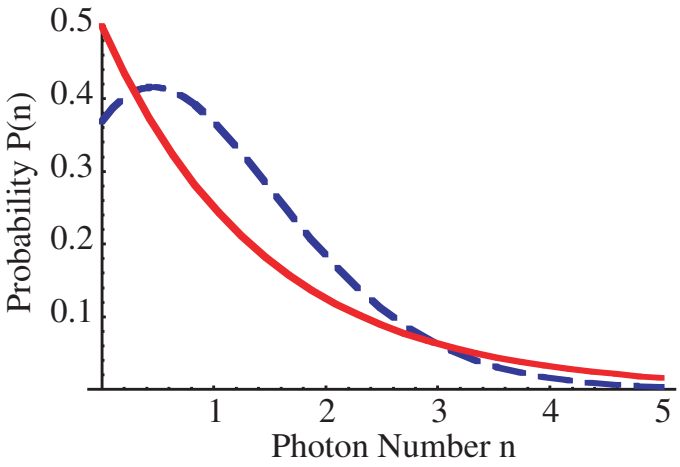

Figure A.7: Comparison of Poisson and thermal photon-number statistics. Probability $P(n)$ of measuring n photons in the field as a function of n for two fields, one with thermal statistics (red, solid line), the other with Poisson statistics (blue, dashed line). Both fields have $\langle n \rangle = 1$.

of the electromagnetic field. Any field whose photon-number fluctuations are sub-Poissonian, i.e. smaller than the fluctuations of Poissonian statistics, can only be explained using a quantized theory of the electromagnetic field [91]. An example of such a state is a Fock state $|n\rangle$ with n photons. For such a state, $\langle n \rangle = n$, and $\mathrm{Var}(n) = 0$.

Comparing Poisson statistics to thermal statistics, we see that for photon fields with equal mean numbers $\langle n \rangle$, the variance for a Poissonian light field ($\langle n \rangle$) is smaller than the variance for a thermal light field ($\langle n \rangle^2 + \langle n \rangle$). Therefore, fields with thermal statistics are said to be super-Poissonian. This is illustrated graphically in Fig. A.7, which shows the probability $P(n)$ of measuring n photons in the field as a function of n for two fields, one with thermal statistics, the other with Poisson statistics, and both with $\langle n \rangle = 1$. Finally, it is worth noting that a detector measuring multiple radiation modes, each with thermal statistics, will measure statistics approaching Poisson for

the combined incident field as the number of thermal modes increases [109].

In addition to the mean and variance, in Chapters 4 and 5 we utilize a quantity referred to as the second-order correlation function to characterize the photon-number statistics of electromagnetic fields. The second-order intensity correlation function [48, 49], can be defined for a field at position x at time t, and position y at time t' as

$$g^{(2)}(x\,t, y\,t') \equiv \langle : \hat{n}_x(t)\,\hat{n}_y(t') : \rangle / \langle \hat{n}_x(t) \rangle \langle \hat{n}_y(t') \rangle, \tag{A.13}$$

where $\hat{n}_i(t)$ denotes the photon-number operator for the field at position i and time t, and $: :$ denotes operator normal ordering.

In Chapters 4 and 5, it is stated that for classical fields $g^{(2)} \geq 1$, whereas an ideal Fock state with n photons yields $g^{(2)} = 1 - 1/n$. This can be easily demonstrated. Consider a field $\hat{\alpha}$ with number operator $\hat{n}_\alpha = \hat{\alpha}^\dagger \hat{\alpha}$, mean number $\langle \hat{n} \rangle \equiv \bar{n}$, and variance $\langle \hat{n}^2 \rangle - \langle \hat{n} \rangle^2 \equiv \mathrm{Var}(\hat{n})$. The second order correlation function is given by

$$\begin{aligned} g^{(2)} &= \frac{\langle \hat{\alpha}^\dagger \hat{\alpha}^\dagger \hat{\alpha} \hat{\alpha} \rangle}{\langle \hat{\alpha}^\dagger \hat{\alpha} \rangle^2} && \text{(A.14)} \\ &= \frac{-\langle \hat{n} \rangle + \mathrm{Var}(\hat{n}) + \langle n \rangle^2}{\langle \hat{n} \rangle^2} && \text{(A.15)} \\ &= 1 - \frac{1}{\langle \hat{n} \rangle} \left(1 - \frac{\mathrm{Var}(\hat{n})}{\langle \hat{n} \rangle} \right), && \text{(A.16)} \end{aligned}$$

where we have used the bosonic commutation relation $[\hat{\alpha}, \hat{\alpha}^\dagger] = 1$, and the relation $\langle \hat{n}^2 \rangle = \mathrm{Var}(\hat{n}) + \langle \hat{n} \rangle^2$.

We see that in the case of an n-photon Fock state, with $\langle \hat{n} \rangle = n$ and $\mathrm{Var}(\hat{n}) = 0$, we have $g^{(2)} = 1 - 1/n$. For a field with Poisson statistics, with $\langle \hat{n} \rangle = \mathrm{Var}(\hat{n})$, we obtain $g^{(2)} = 1$. Since Poisson statistics possess the minimum possible photon-number fluctuations of any classical field [91], any classical field will have $\mathrm{Var}(\hat{n}) \geq \langle \hat{n} \rangle$, and

therefore $g^{(2)} \geq 1$.

In order to experimentally measure the second-order correlation function of a field at the same point in space and time, the field must be split at a 50-50 beamsplitter and sent to two single-photon detectors, as shown in Figs. 3.2 and 4.2. In this case, the second-order correlation function is given by

$$g^{(2)}(D1, D2) = \langle \hat{n}_1 \, \hat{n}_2 \rangle / \langle \hat{n}_1 \rangle \langle \hat{n}_2 \rangle, \tag{A.17}$$

where $\hat{n}_1$ ($\hat{n}_2$) is the number operator for detector D1 (D2). Eq. (A.16) can also be derived for this experimental setup. Because the vacuum field enters the unused input port of the beamsplitter, each of the two output modes contain the incident mode and the vacuum mode. We denote the incident field $\hat{\alpha}$, the vacuum field $\hat{v}$, and the output modes in the two arms of the beamsplitter $\hat{\alpha}_1$ and $\hat{\alpha}_2$. In this case, the two output modes are given by

$$\hat{\alpha}_1 = \frac{1}{\sqrt{2}}(\hat{\alpha} + \hat{v}) \tag{A.18}$$

$$\hat{\alpha}_2 = \frac{1}{\sqrt{2}}(\hat{\alpha} - \hat{v}). \tag{A.19}$$

$$\tag{A.20}$$

Writing the number operators for $\hat{\alpha}_1$ and $\hat{\alpha}_2$ as $\hat{n}_1$ and $\hat{n}_2$ respectively, and substituting these number operators into Eq. (A.17), we have

$$g^{(2)} = \frac{\langle (\hat{\alpha}^\dagger + \hat{v}^\dagger)(\hat{\alpha} + \hat{v})(\hat{\alpha}^\dagger - \hat{v}^\dagger)(\hat{\alpha} - \hat{v}) \rangle}{\langle (\hat{\alpha}^\dagger + \hat{v}^\dagger)(\hat{\alpha} + \hat{v}) \rangle \langle (\hat{\alpha}^\dagger - \hat{v}^\dagger)(\hat{\alpha} - \hat{v}) \rangle}. \tag{A.21}$$

Using $\langle \hat{v}^\dagger \hat{v} \rangle = 0$, $\langle \hat{v} \hat{v}^\dagger \rangle = 1$, and $\hat{n} = \hat{\alpha}^\dagger \hat{\alpha}$, we again obtain Eq. (A.16).

A.4 Hardware Requirements for Detection of Twin-Mode Squeezing

In this appendix, we discuss the requirements on the detection hardware for implementing the experiments described in Chapter 2. In the case of Raman signals studied in Chapter 2, with typical powers on the order of a few microwatts, silicon-based photodiodes in a transimpedance amplifying configuration (see Appendix A.2 and Refs. [51] and [59]) must be used, rather than avalanche photodetectors. Here the main challenge is to meet requirements for low noise levels and high detection resolution. The technical white noise in the detected signals due to, for example, Johnson noise must be small compared to fluctuations of the signal field at the level of the standard quantum limit, which favors working with large photon numbers. However, the resolution for processing the signals needs to be better than the standard quantum limit as well. For signals at the standard quantum limit with average photon number $\overline{n}$, the fluctuation-to-signal ratio scales as (in terms of variances) $1/\overline{n}$. Thus meeting the resolution requirements favors working with small photon numbers.

We will analyze the noise-to-signal ratios for white noise, as well as the resolution requirements, and normalize them to the standard quantum limit (Fig. A.8). The signal is a photon flux $\Phi_n(t)$ measured at sample rate R. This sets the level for $\overline{n} = \overline{\Phi}_n/R$, and the noise-to-signal ratio (in terms of variances) for the standard quantum limit:

$$NSR_Q = R/\overline{\Phi}_n\,. \tag{A.22}$$

We will assume that the power (photon flux) of the signal fields is measured by

probing the voltage of a circuit as in Fig. A.8. With standard commercial components one can realize photo-detector-amplifier circuits with current amplification of $G_i = 5000$, a bandwidth larger than 1 MHz, and a white noise level below $\sigma_{V\,1\mathrm{Hz}} = 50\ \mathrm{nV}/\sqrt{\mathrm{Hz}}$ [59, 51]. With one electron (e) of photo-current per photon, the voltage signal level is then $\overline{\Phi}_n e G_i Z_{50}$, where Z_{50} is the 50 Ω impedance of the detection system. The voltage noise level is $\sigma_V = \sigma_{V\,1\mathrm{Hz}}\sqrt{R/2}$. This gives for the normalized noise-to-signal level (for white noise from the detection system):

$$NSR_W/NSR_Q = \frac{1}{\overline{\Phi}_n}\frac{\sigma_{V1\mathrm{Hz}}^2}{2(eG_iZ_{50})^2}\,, \tag{A.23}$$

see also Fig. A.8. Note that the expression is independent of the sample rate R. The white noise of the detection system clearly sets a minimum level of $\overline{\Phi}_n$ for which squeezing can be observed.

In the experiments, we recorded the signals with an analog-to-digital sampling process, which needs to be accurate enough to confirm noise-to-signal levels that are smaller than NSR_Q. Because the Raman signals show large excess noise, the detection system needs more dynamic range than for a signal with Poissonian photon statistics; hence, for this resolution analysis we will compare to a signal level $\overline{n} = M_{th}\overline{\Phi}_n/R$. The margin M_{th} needs to be about a factor of 5 for signals with thermal photon statistics. We assume a sampling process with a certain number of bits (bit) and sample time τ_s. Oversampling and averaging over results recorded during $1/R$ can be used to enhance the effective resolution with a factor $\sqrt{\tau_s R}$. The finite recording resolution leads then to noise on the recorded signal with a normalized noise-to-signal ratio:

$$NSR_R/NSR_Q = \overline{\Phi}_n\frac{M_{th}^2\tau_s}{(2^{bit})^2}\,. \tag{A.24}$$

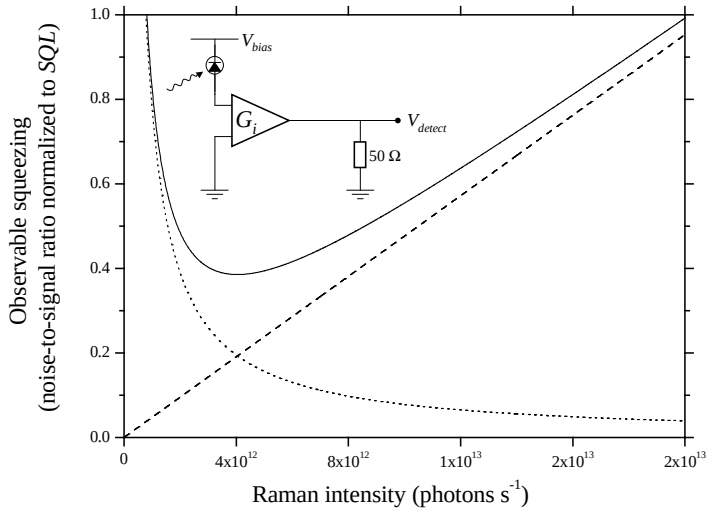

Figure A.8: Limitations on the observation of twin-mode intensity squeezing. **(Inset)** Generic photo-detector-amplifier circuit. The photo-current from a photo-diode (voltage biased in reverse at V_{bias}) is current-amplified with gain G_i, and voltage detected (V_{detect}) with 50 Ω technology. **(Main graph)** Observable squeezing parameters $\mathrm{Var}(n)/\overline{n}$ for measurements on a Fock state with photon number $\overline{n}$, as limited by technical noise-to-signal ratios normalized to the fluctuation-to-signal ratio for the standard quantum limit $SQL = 1/\overline{n}$. The dotted line is for a white noise floor in the detection process (here plotted for current amplification $G_i = 5000$ and a white noise level of 50 nV/$\sqrt{\mathrm{Hz}}$). The dashed line results from the finite resolution of analog-to-digital sampling (here from adjacent averaging of data sampled at 8 GHz with 8 bit resolution and using $M_{th} = 5$, see the text for details). The solid line gives the sum of the two noise contributions.

Note that this expression is also independent of the sample rate. The expression reflects that with increasing photon flux the resolution requirement scales as the standard quantum limit $1/\overline{n}$. Thus the finite recording resolution sets an upper limit on $\overline{\Phi}_n$ for which squeezing can be observed. (Note that at very low values of $\overline{\Phi}_n$ the relative sampling resolution cannot be realized, and for $\overline{\Phi}_n$ approaching zero the dashed line in Fig. A.8 should curve up; it can be described as a source of white noise.) As shown in Fig. A.8 for realistic experimental parameters, there is a $\overline{\Phi}_n$-window for

values as in Fig. 2.4 in which a squeezing parameter below 0.5 can be observed. This analysis was in terms of the detection of a single channel, but generalizing it to the statistics of two subtracted channels does not alter the values in Fig. A.8. The results of this analysis are independent of sample rate R, but one should note that twin-mode intensity squeezing is only expected for experiments with R commensurate with the Raman bandwidth or smaller.

The parameters assumed for the photodetectors and analog-to-digital sampling in Fig. A.8 correspond very closely to actual experimental parameters. As described in Appendix A.2, the 250 kΩ transimpedance resistor, over the output impedance of 50Ω corresponds to a current amplification of 5000. The measured white noise level for our photodetectors was 30nV/$\sqrt{\text{Hz}}$. The digital oscilloscope used to record the traces (Lecroy model LT374L) used adjacent averaging with 8-bit resolution at a rate of 4 GHz. An optical power of 1 μW $\approx 4 \cdot 10^{12}$ photons s^{-1} is a typical value for the Raman modes in our experiments.

The discussion so far has been concerned with a test for squeezing in the time domain. Problems arising from technical low-frequency $1/f$ noise [45] (so-called because its power density varies with frequency as $1/f$) can be dealt with by performing the test for squeezing in the frequency domain. The discrete Fourier transform (DFT) formalism [21] can be used for a straightforward transformation of the recorded time series m_1 and m_2 and the criteria for squeezing, as is done in Fig. 2.8.

Appendix B

Appendices to Chapter 4

B.1 Evaluating the Uncertainty in the Second-Order Correlation Function

In this appendix, we describe the method used to calculate the uncertainty in measurements of the second-order correlation function shown in Chapters 4 and 5. To begin, assume we have two random variables X and Y (standing for $AS1$ and $AS2$ - anti-Stokes channels 1 and 2). For present purposes, we must assume that neither the joint, nor the separate distributions of X and Y are known.

We define the following number (not a random variable) that we want to find:

$$g^{(2)} \equiv \frac{\langle X \times Y \rangle}{\langle X \rangle \langle Y \rangle}, \tag{B.1}$$

where the expectation value is taken using the full distribution. Given the joint distribution P_{12} of the anti-Stokes channels 1 and 2, we know this number exactly. In practice, however, we do not know the joint distribution P_{12}. Instead, we have a

sample S from N measurements

$$S = \{x_1, y_1, \ldots, x_N, y_N\}. \tag{B.2}$$

The goal of this appendix is to find an estimate for $g^{(2)}$, and calculate an uncertainty measure for how close our estimate is to $g^{(2)}$, given that all we possess is a sample S from N measurements.

In the following analysis, we follow the procedure outlined in Ref. [102]. $g^{(2)}$ is our *measurand*. The *measurement equation* is

$$g^{(2)} = f\left(\langle X \times Y\rangle, \langle X\rangle, \langle Y\rangle\right) = \frac{\langle X \times Y\rangle}{\langle X\rangle\langle Y\rangle}. \tag{B.3}$$

To compute the estimate for $g^{(2)}$ (call it z), we simply compute estimates for $\langle X \times Y\rangle$, $\langle X\rangle$, and $\langle Y\rangle$ and substitute them into f. The natural estimates for the three expectation values are just sample means, denoted by "bars":

$$\overline{xy} = \frac{1}{N}\sum_{i=1}^{N} x_i y_i \tag{B.4}$$

$$\overline{x} = \frac{1}{N}\sum_{i=1}^{N} x_i \tag{B.5}$$

$$\overline{y} = \frac{1}{N}\sum_{i=1}^{N} y_i \tag{B.6}$$

$$z = f(\overline{xy}, \overline{x}, \overline{y}). \tag{B.7}$$

For each experiment that yields a sample S and hence a single value of z, z is a single observation of a random variable, referred to as an estimator, defined by

$$Z = f\left(\frac{1}{N}\sum_{i=1}^{N} X_i Y_i, \frac{1}{N}\sum_{i=1}^{N} X_i, \frac{1}{N}\sum_{i=1}^{N} Y_i\right), \tag{B.8}$$

where the joint distribution of X_i and Y_i is the same for all i and equal to the joint distribution of X and Y. Random variables with different i are independent. The

standard measure of uncertainty [102, 44] is called the *standard uncertainty* and is an estimate for the standard deviation of Z, which in turn is the positive square root of the estimate for the variance of Z. To find this standard uncertainty (call it $u(z)$), we first need to find estimates for the standard uncertainties $u(\overline{xy})$, $u(\overline{x})$, and $u(\overline{y})$ of the three arguments of f in (B.7). From now on, we will drop the word "standard" when referring to the standard uncertainty. These uncertainties are estimates for standard deviations of estimators $\frac{1}{N}\sum_{i=1}^{N} X_i Y_i$, $\frac{1}{N}\sum_{i=1}^{N} X_i$, and $\frac{1}{N}\sum_{i=1}^{N} Y_i$, respectively, while $\overline{xy}$, $\overline{x}$, and $\overline{y}$ are single observations of these estimators. Since

$$\mathrm{Var}\left(\frac{1}{N}\sum_{i=1}^{N} X_i\right) = \frac{1}{N}\mathrm{Var}\left(X\right), \tag{B.9}$$

and since the natural estimate for $\mathrm{Var}\left(X\right)$ is the sample variance[1] $\frac{N}{N-1}\overline{(x-\overline{x})^2}$, we have

$$u^2(\overline{x}) = \frac{1}{N-1}\overline{(x-\overline{x})^2} \tag{B.10}$$

Similarly,

$$u^2(\overline{xy}) = \frac{1}{N-1}\overline{(xy-\overline{xy})^2} \tag{B.11}$$

$$u^2(\overline{y}) = \frac{1}{N-1}\overline{(y-\overline{y})^2}. \tag{B.12}$$

In order to compute $u(z)$, in addition to the uncertainties of the arguments we also need estimates $u(\overline{x},\overline{y})$, $u(\overline{x},\overline{xy})$, and $u(\overline{y},\overline{xy})$ for the covariances of the estimators for $\langle X\rangle$, $\langle Y\rangle$, and $\langle XY\rangle$: $\mathrm{Cov}\left(\frac{1}{N}\sum_{i=1}^{N} X_i, \frac{1}{N}\sum_{i=1}^{N} Y_i\right)$, $\mathrm{Cov}\left(\frac{1}{N}\sum_{i=1}^{N} X_i, \frac{1}{N}\sum_{i=1}^{N} X_i Y_i\right)$,

[1] We have the $\frac{N}{N-1}$ prefactor because the estimator $\frac{1}{N-1}\sum_{i=1}^{N}\left(X_i - \frac{1}{N}\left(\sum_{j=1}^{N} X_j\right)\right)^2$ is unbiased while the estimator $\frac{1}{N}\sum_{i=1}^{N}\left(X_i - \frac{1}{N}\left(\sum_{j=1}^{N} X_j\right)\right)^2$ is biased.

and $\mathrm{Cov}\left(\frac{1}{N}\sum_{i=1}^{N} Y_i, \frac{1}{N}\sum_{i=1}^{N} X_i Y_i\right)$, respectively. Since

$$\mathrm{Cov}\left(\frac{1}{N}\sum_{i=1}^{N} X_i, \frac{1}{N}\sum_{i=1}^{N} Y_i\right) = \frac{1}{N}\mathrm{Cov}\left(X, Y\right), \tag{B.13}$$

and since the natural estimate for $\mathrm{Cov}\left(X, Y\right)$ is the sample covariance [2] $\frac{N}{N-1}\overline{(x-\overline{x})(y-\overline{y})}$, we have

$$u(\overline{x}, \overline{y}) = \frac{1}{N-1}\overline{(x-\overline{x})(y-\overline{y})}. \tag{B.14}$$

Similarly,

$$u(\overline{x}, \overline{xy}) = \frac{1}{N-1}\overline{(x-\overline{x})(xy-\overline{xy})} \tag{B.15}$$

$$u(\overline{y}, \overline{xy}) = \frac{1}{N-1}\overline{(y-\overline{y})(xy-\overline{xy})}. \tag{B.16}$$

From the estimates for the three arguments of f, the three uncertainties in the arguments, and the three estimates for the covariances, we can compute $u(z)$ using the law of propagation of uncertainty, which is

$$\begin{aligned} u^2(z) = & \left(\frac{\partial f}{\partial \overline{x}}\right)^2 u^2(\overline{x}) + \left(\frac{\partial f}{\partial \overline{y}}\right)^2 u^2(\overline{y}) + \left(\frac{\partial f}{\partial \overline{xy}}\right)^2 u^2(\overline{xy}) \\ & +2\left[\frac{\partial f}{\partial \overline{x}}\frac{\partial f}{\partial \overline{y}}u(\overline{x}, \overline{y}) + \frac{\partial f}{\partial \overline{x}}\frac{\partial f}{\partial \overline{xy}}u(\overline{x}, \overline{xy}) + \frac{\partial f}{\partial \overline{y}}\frac{\partial f}{\partial \overline{xy}}u(\overline{y}, \overline{xy})\right], \end{aligned} \tag{B.17}$$

where the partial derivatives are evaluated at the estimates $\overline{xy}$, $\overline{x}$, and $\overline{y}$. Using Eq. (B.3), taking the partial derivatives, and also using Eqs. (B.10) - (B.12) and Eqs. (B.14) - (B.16), we obtain

$$\begin{aligned} u^2(z) = & \frac{f^2(\overline{xy}, \overline{x}, \overline{y})}{N-1}\Big[\frac{\overline{(x-\overline{x})^2}}{\overline{x}^2} + \frac{\overline{(y-\overline{y})^2}}{\overline{y}^2} + \frac{\overline{(xy-\overline{xy})^2}}{\overline{xy}^2} \\ & +2\frac{\overline{(x-\overline{x})(y-\overline{y})}}{\overline{x}\,\overline{y}} - 2\frac{\overline{(x-\overline{x})(xy-\overline{xy})}}{\overline{x}\,\overline{xy}} - 2\frac{\overline{(y-\overline{y})(xy-\overline{xy})}}{\overline{y}\,\overline{xy}}\Big] \end{aligned} \tag{B.18}$$

[2] Again, as in the case of standard deviation, we use a $\frac{N}{N-1}$ prefactor to have the corresponding estimator $\frac{1}{N-1}\sum_{i=1}^{N}\left(X_i - \frac{1}{N}\left(\sum_{j=1}^{N} X_j\right)\right)\left(Y_i - \frac{1}{N}\left(\sum_{k=1}^{N} Y_k\right)\right)$ unbiased.

This method was used to calculate the uncertainty in the normalized variance V from Chapter 3 (although using a different function f than the function used in this appendix) as well as the uncertainty in the second-order correlation function $g^{(2)}$ from Chapters 4 and 5.

Bibliography

[1] A. André and M. Bajcsy and A. S. Zibrov and M. D. Lukin. *Phys. Rev. Lett.*, 94:063902, 2005.

[2] D. Akamatsu, K. Akiba, and M. Kozuma. *Phys. Rev. Lett.*, 92:203602, 2004.

[3] A. André. *Nonclassical states of light and atomic ensembles: Generation and New Applications*. Ph.D. Thesis, Harvard University, Cambridge, MA, 2005.

[4] A. André, M. D. Eisaman, R. L. Walsworth, A. S. Zibrov, and M. D. Lukin. *J. Phys. B: At. Mol. Opt. Phys.*, 38:S589, 2005.

[5] M. Aspelmeyer, H. R. Böhm, T. Gyatso, T. Jennewein, R. Kaltenbaek, M. Lindenthal, G. Molina-Terriza, A. Poppe, K. Resch, M. Taraba, R. Ursin, P. Walther, and A. Zeilinger. *Science*, 301:621, 2003.

[6] O. Aytur and P. Kumar. *Phys. Rev. Lett.*, 65:1551, 1990.

[7] H.-A. Bachor. *A Guide to Experiments in Quantum Optics*. Wiley-VCH, New York, 1998.

[8] M. Bajcsy, A. S. Zibrov, and M. D. Lukin. *Nature*, 426:638, 2003.

[9] V. Balić, D. A. Braje, P. Kolchin, G. Y. Yin, and S. E. Harris. *Phys. Rev. Lett.*, 94:183601, 2005.

[10] A. Beveratos, R. Brouri, T. Gacoin, J-P. Poizat, and P. Grangier. *Phys. Rev. A*, 64:061802, 2001.

[11] A. Beveratos, R. Brouri, T. Gacoin, A. Villing, J.-P. Poizat, and P. Grangier. *Phys. Rev. Lett.*, 89:187901, 2002.

[12] A. T. Black, J. K. Thompson, and V. Vuletić. *Phys. Rev. Lett.*, 95:133601, 2005.

[13] B. B. Blinov, D. L. Moehring, L.-M. Duan, and C. Monroe. *Nature*, 428:153, 2004.

[14] K. J. Boller, A. Imamoglu, and S. E. Harris. *Phys. Rev. Lett.*, 66:2593, 1991.

[15] R. W. Boyd. *Nonlinear Optics*. Academic Press, San Diego, 2nd edition, 2003.

[16] D. A. Braje, V. Balić, G. Y. Yin, and S. E. Harris. *Phys. Rev. A*, 68:041801(R), 2003.

[17] S. Brattke, G. R. Guthohrlein, M. Keller, W. Lange, B. Varcoe, and H. Walther. *J. Mod. Opt.*, 50:1103, 2003.

[18] S. L. Braunstein and A. K. Pati, editors. *Quantum Information with Continuous Variables*. Kluwert, Dordrecht, 2003.

[19] H.-J. Briegel, W. Dur, J. I. Cirac, and P. Zoller. *Phys. Rev. Lett.*, 78:3221, 1998.

[20] H. J. Briegel, W. Dur, S. J. van Enk, J. I. Cirac, and P. Zoller. Quantum repeaters. In D. Bouwmeester, A. Ekert, and A. Zeilinger, editors, *The Physics of Quantum Information*. Springer, Berlin, 2000.

[21] W. L. Briggs and V. E. Henson. *The DFT: An Owner's Manual for the Discrete Fourier Transform*. Society for Industrial and Applied Mathematics, Philadelphia, 1995.

[22] C. Brunel, B. Lounis, P. Tamarat, and M. Orrit. *Phys. Rev. Lett.*, 83:2722, 1999.

[23] D. Budker, D. F. Kimball, S. M. Rochester, and V. V. Yashchuk. *Phys. Rev. Lett.*, 83:1767, 1999.

[24] G. Casella and R. L. Berger. *Statistical Inference*. Duxbury, Pacific Grove, CA, 2002.

[25] S. Castelletto, I. P. Degiovanni, V. Schettini, and A. Migdall. *Opt. Express*, 13:6709, 2005.

[26] T. Chanelière, D. N. Matsukevich, S. D. Jenkins, S.-Y. Lan, T. A. B. Kennedy, and A. Kuzmich. *Nature*, 438:833, 2005.

[27] L. Childress, J. M. Taylor, A. S. Sørensen, and M. D. Lukin. *Phys. Rev. A*, 72:052330, 2005.

[28] L. Childress, J. M. Taylor, A. S. Sørensen, and M. D. Lukin. *Phys. Rev. Lett.*, 96:070504, 2006.

[29] C. W. Chou, H. de Riedmatten, D. Felinto, S. V. Polyakov, S. J. van Enk, and H. J. Kimble. *Nature*, 438:828, 2005.

[30] C. W. Chou, S. V. Polyakov, A. Kuzmich, and H. J. Kimble. *Phys. Rev. Lett.*, 92:213601, 2004.

[31] J. I. Cirac, P. Zoller, H. J. Kimble, and H. Mabuchi. *Phys. Rev. Lett.*, 78:3221, 1997.

[32] R. J. Cook. *Phys. Rev. A*, 25:2164, 1982.

[33] A. Dantan and M. Pinard. *Phys. Rev. A*, 69:043810, 2004.

[34] L. M. Duan, M. D. Lukin, J. I. Cirac, and P. Zoller. *Nature*, 414:413, 2001.

[35] M. D. Eisaman, A. André, F. Massou, M. Fleischhauer, A.S. Zibrov, and M. D. Lukin. *Nature*, 438:837, 2005.

[36] M. D. Eisaman, A. André, F. Massou, G.-W. Li, L. Childress, A. S. Zibrov, and M. D. Lukin. In P. R. Hemmer, P. Heszler J. R. Gea-Banacloche, and M. S. Zubairy, editors, *Fluctuations and Noise in Photonics and Quantum Optics III*, volume 5842, page 105. SPIE, Bellingham, WA, 2005.

[37] M. D. Eisaman, L. Childress, A. André, F. Massou, A.S. Zibrov, and M. D. Lukin. *Phys. Rev. Lett.*, 93:233602, 2004.

[38] J. Fan and A. Migdall. *Opt. Express*, 13:5777, 2005.

[39] J. Fan, A. Migdall, and L. J. Wang. *Opt. Lett.*, 30:3368, 2005.

[40] J. Fiurášek, N. J. Cerf, and E. S. Polzik. *Phys. Rev. Lett.*, 93:180501, 2004.

[41] M. Fleischhauer, A. Imamoglu, and J. P. Marangos. *Rev. Mod. Phys.*, 77:633–673, 2005.

[42] M. Fleischhauer and M. D. Lukin. *Phys. Rev. Lett.*, 84:5094, 2000.

[43] M. Fleischhauer and M. D. Lukin. *Phys. Rev. A*, 65:022314, 2002.

[44] International Committee for Weights and Measures. Guide to the expression of uncertainty in measurement. 1993.

[45] S. Franco. *Design with Operational Amplifiers and Analog Integrated Circuits*. McGraw-Hill, New York, 2nd edition, 1998.

[46] E. Fraval, M. J. Sellars, and J. J. Longdell. *Phys. Rev. Lett.*, 92:077601, 2004.

[47] E. Fraval, M. J. Sellars, and J. J. Longdell. *Phys. Rev. Lett.*, 95:030506, 2005.

[48] R. J. Glauber. *Physical Review*, 130:2529, 1963.

[49] R. J. Glauber. *Physical Review*, 131:2766, 1963.

[50] A. V. Gorshkov, A. André, M. Fleischhauer, A. S. Sørensen, and M. D. Lukin. *quant-ph/0604037*, 2006.

[51] M. B. Gray, D. A. Shaddock, C. C. Harb, and H. A. Bachor. *Rev. Sci. Instr.*, 69:3755, 1998.

[52] K. Hammerer, K. Mølmer, E. S. Polzik, and J. I. Cirac. *Phys. Rev. A*, 70:044304, 2004.

[53] W. Happer. *Rev. Mod. Phys.*, 44:169, 1972.

[54] S. E. Harris. *Physics Today*, 50(7):36, 1997.

[55] S. E. Harris, M. K. Oshman, and R. L. Byer. *Phys. Rev. Lett.*, 18:732, 1967.

[56] L. V. Hau, S. E. Harris, Z. Dutton, and C. H. Behroozi. *Nature*, 397:594, 1999.

[57] A. Heidmann, R. J. Horowicz, S. Reynaud, E. Giacobino, and C. Fabre. *Phys. Rev. Lett.*, 59:2555, 1987.

[58] P. R. Hemmer, D. P. Katz, J. Donoghue, M. Cronin-Golomb, M. S. Shahriar, and P. Kumar. *Opt. Lett.*, 20:982, 1995.

[59] P. C. D. Hobbs. *Building electro-optical systems: making it all work*. John Wiley and Sons, Inc, New York, 2000.

[60] M. Hohensee, A. André, and M. D. Lukin. *to be published*, 2006.

[61] C. K. Hong and L. Mandel. *Phys. Rev. Lett.*, 56:58, 1986.

[62] C. K. Hong, Z. Y. Ou, and L. Mandel. *Phys. Rev. Lett.*, 59:2044, 1987.

[63] P. Horowitz and W. Hill. *The Art of Electronics*. Cambridge University Press, Cambridge, 1989.

[64] W. Jiang, C. Han, P. Xue, L.-M. Duan, and G.-C. Guo. *Phys. Rev. A*, 69:043819, 2004.

[65] B. Julsgaard, J. Sherson, J. I. Cirac, J. Fiurasek, and E. S. Polzik. *Nature*, 432:482–486, 2004.

[66] M. M. Kash, V. A. Sautenkov, A. S. Zibrov, L. Hollberg, G. R. Welch, M. D. Lukin, Y. Rostovtsev, E. S. Fry, and M. O. Scully. *Phys. Rev. Lett.*, 82:5229, 1999.

[67] M. Keller, B. Lange, K. Hayasaka, W. Lange, and H. Walther. *Nature*, 431:1075, 2004.

[68] J. F. Kielkopf. *J. Phys. B: At. Mol. Opt. Phys.*, 9:L547, 1976.

[69] J. Kim, O. Benson, H. Kan, and Y. Yamamoto. *Science*, 397:500, 1999.

[70] H. J. Kimble. *Physica Scripta*, 76:127, 1998.

[71] M. Klein, I. Novikova, D. F. Phillips, and R. L. Walsworth. *quant-ph/0602131*, 2006.

[72] E. Knill, R. Laflamme, and G. J. Milburn. *Nature*, 409:46, 2001.

[73] A. E. Kozhekin, K. Mølmer, and E. S. Polzik. *Phys. Rev. A*, 62:033809, 2000.

[74] A. Kuhn, M. Hennrich, and G. Rempe. *Phys. Rev. Lett.*, 89:067901, 2002.

[75] C. Kurtsiefer, S. Mayer, P. Zarda, and H. Weinfurter. *Phys. Rev. Lett.*, 85:290, 2000.

[76] A. Kuzmich, W. P. Bowen, A. D. Boozer, A. Boca, C. W. Chou, L.-M. Duan, and H. J. Kimble. *Nature*, 423:731, 2003.

[77] A. Kuzmich, K. Mølmer, and E. S. Polzik. *Phys. Rev. Lett.*, 79:4782, 1997.

[78] W. E. Lamb. *Appl. Phys. B*, 60:77, 1995.

[79] C. Liu, Z. Dutton, C. H. Behroozi, and L. V. Hau. *Nature*, 409:490, 2001.

[80] J. J. Longdell, E. Fraval, M. J. Sellars, and N. B. Manson. *Phys. Rev. Lett.*, 95:063601, 2005.

[81] R. Loudon. *The Quantum Theory of Light*. Oxford University Press, New York, 2000.

[82] B. Lounis and W. E. Moerner. *Nature*, 407:491, 2000.

[83] M. D. Lukin. *Rev. Mod. Phys.*, 75:457, 2003.

[84] M. D. Lukin, P. R. Hemmer, and M. O. Scully. *Advances in Atomic, Molecular and Optical Physics*, 42:347, 2000.

[85] M. D. Lukin and A. Imamoğlu. *Phys. Rev. Lett.*, 84:1419, 2000.

[86] M. D. Lukin and A. Imamoğlu. *Nature*, 413:273, 2001.

[87] M. D. Lukin, A. B. Matsko, M. Fleischhauer, and M. O. Scully. *Phys. Rev. Lett.*, 82:1847, 1999.

[88] M. D. Lukin, S. F. Yelin, and M. Fleischhauer. *Phys. Rev. Lett.*, 84:4232, 2000.

[89] A. Mair, J. Hager, D. F. Phillips, R. L. Walsworth, , and M. D. Lukin. *Phys. Rev. A*, 65:031802(R), 2002.

[90] L. Mandel. *Phys. Rev.*, 144:1071, 1961.

[91] L. Mandel and E. Wolf. *Optical Coherence and Quantum Optics*. Cambridge University Press, Cambridge, 1995.

[92] F. De Martini, G. Di Giuseppe, and M. Marrocco. *Phys. Rev. Lett.*, 76:900, 1996.

[93] D. N. Matsukevich, T. Chanelière, S. D. Jenkins, S.-Y. Lan, T. A. B. Kennedy, and A. Kuzmich. *Phys. Rev. Lett.*, 96:030405, 2006.

[94] D. N. Matsukevich and A. Kuzmich. *Science*, 306:663, 2004.

[95] D. N. Matsukevich *et al. Phys. Rev. Lett.*, 95:040405, 2005.

[96] J. McKeever, A. Boca, A. D. Boozer, J. R. Buck, and H. J. Kimble. *Nature*, 425:268, 2003.

[97] J. McKeever, A. Boca, A. D. Boozer, R. Miller, J. R. Buck, A. Kuzmich, and H. J. Kimble. *Science*, 303:1992, 2004.

[98] P. Meystre and M. Sargent III. *Elements of Quantum Optics*. Springer, New York, 3rd edition, 1999.

[99] P. Michler, A. Kiraz, C. Becher, W. V. Schoenfeld, P. M. Petroff, L. Zhang, E. Hu, and A. Imamoglu. *Science*, 290:2282, 2000.

[100] A. Muthukrishnan, M. O. Scully, and M. Suhail Zubairy. *Opt. Phot. News Trends*, 3:S–18, 2003.

[101] J. Nunn, I. A. Walmsley, M. G. Raymer, K. Surmacz an F. C. Waldermann, Z. Wang, and D. Jaksch. *quant-ph/0603268*, 2006.

[102] National Institute of Standards and Technology. Guidelines for evaluating and expressing the uncertainty of nist measurement results. *NIST Technical Note*, 1297, 1994.

[103] D. F. Phillips, M. Fleischhauer, A. Mair, R. L. Walsworth, and M. D. Lukin. *Phys. Rev. Lett.*, 86:783, 2001.

[104] S. V. Polyakov, C. W. Chou, D. Felinto, and H. J. Kimble. *Phys. Rev. Lett.*, 93:263601, 2004.

[105] M. G. Raymer, J. Noh, K. Banaszek, and I. A. Walmsley. *Phys. Rev. A*, 72:023825, 2005.

[106] M. G. Raymer and I. A. Walmsley. In E. Wolf, editor, *Progress in Optics*, volume 28, pages 181 – 270. North-Holland, Amsterdam, 1990.

[107] K.J. Resch, M. Lindenthal, B. Blauensteiner, H.R. Böhm, A. Fedrizzi, C. Kurtsiefer, A. Poppe, T. Schmitt-Manderbach, M. Taraba, R. Ursin, P. Walther, H. Weier, H. Weinfurter, and A. Zeilinger. *Opt. Express*, 13:202, 2005.

[108] V. I. Rupasov. *Phys. Lett. A*, 175:93, 1993.

[109] B. E. A. Saleh and M. C. Teich. *Fundamentals of photonics*. John Wiley and Sons, Inc, New York, 1991.

[110] C. Santori, D. Fattal, J. Vučković, G. S. Solomon, and Y. Yamamoto. *Nature*, 419:594, 2002.

[111] C. Santori, M. Pelton, G. Solomon, Y. Dale, and Y. Yamamoto. *Phys. Rev. Lett.*, 86:1502, 2001.

[112] M. O. Scully and C. H. R. Ooi. *J. Opt. B: Quantum Semiclass. Opt.*, 6:S816–S820, 2004.

[113] M. O. Scully and M. S. Zubairy. *Quantum Optics*. Cambridge University Press, Cambridge, 1997.

[114] D. T. Smithey, M. Beck, M. Belsley, and M. G. Raymer. *Phys. Rev. Lett.*, 69:2650, 1992.

[115] D. A. Steck. *Rubidium 87 D Line Data*, volume 1.6. http;//steck.us/alkalidata/, 2003.

[116] A. B. URen, C. Silberhorn, J. L. Ball, K. Banaszek, and I. A. Walmsley. *Phys. Rev. A*, 72:021802(R), 2005.

[117] A. B. URen, C. Silberhorn, K. Banaszek, and I. A. Walmsley. *Phys. Rev. Lett.*, 93:093601, 2004.

[118] C. H. van der Wal, M. D. Eisaman, A. André, R. L. Walsworth, D. F. Phillips, A. S. Zibrov, and M. D. Lukin. *Science*, 301:196, 2003.

[119] J. Vanier and C. Audoin. *The Quantum Physics of Atomic Frequency Standards*, volume 1. IOP Publishing Ltd, Philadelphia, 1989.

[120] J. Vanier and C. Audoin. *The Quantum Physics of Atomic Frequency Standards*, volume 2. IOP Publishing Ltd, Philadelphia, 1989.

[121] J. Vanier, J.-F. Simard, and J.-S. Boulanger. *Phys. Rev. A*, 9:1031, 1974.

[122] B. T. H. Varcoe, S. Brattke, M. Weidinger, and H. Walther. *Nature*, 403:743, 2000.

[123] E. Waks, E. Diamanti, B. C. Sanders, S. D. Bartlett, and Y. Yamamoto. *Phys. Rev. Lett.*, 92:113602, 2004.

[124] D. F. Walls and G. J. Milburn. *Quantum Optics*. Springer, Berlin, 1st edition, 1994.

[125] A. Yariv. *Optical Electronics in Modern Communications*. Oxford University Press, New York, 5th edition, 1997.

[126] Z. Yuan, B. E. Kardynal, R. M. Stevenson, A. J. Shields, C. J. Lobo, K. Cooper, N. S. Beattie, D. A. Ritchie, and M. Pepper. *Science*, 295:102, 2002.

[127] V. Zwiller, T. Aichele, W. Seifert, J. Persson, and O. Benson. *Appl. Phys. Lett.*, 82:1509, 2003.

[128] V. Zwiller, H. Blom, P. Jonsson, N. Panev, S. Jeppesen, T. Tsegaye, E. Goobar, M.-E. Pistol, L. Samuelson, and G. Bjork. *Appl. Phys. Lett.*, 78:2476, 2001.